

Additive Manufacturing of Ceramics

Printing Beyond the Binder

by

Giorgia Franchin

Bachelor of Science in Materials and Chemical Engineering, 2011

University of Padova

Master of Science in Materials Engineering, 2013

University of Padova

Submitted to the Department of Industrial Engineering

In partial fulfillment of the requirements for the degree of

Doctor of Philosophy of Industrial Engineering

Curriculum: Mechanical, Materials and Chemical Engineering

At the

University of Padova

Supervisor: _____ **Prof. Paolo Colombo**

Professor of Materials Science and Technology

University of Padova

Co-supervisor: _____ **Prof. Neri Oxman**

Associate Professor of Media Arts and Sciences

Massachusetts Institute of Technology

Acknowledgements

When I talk about my work, the focus is on goals, data collection and discussion; I report the findings and try to provide interpretations. Very little of the daily lab life gets into these reports: if I am here, submitting my PhD thesis in a few hours, it is thanks to all the people that have walked alongside with me in and outside the lab, providing incredible inspiration and continuous support.

I would like to start from Prof. Paolo Colombo, my supervisor and mentor for more than four years: our adventure in the Additive Manufacturing world has begun together, approaching with genuine enthusiasm a sketchy Do-It-Yourself FDM Printer; what a fascinating journey it has been! You are an endless furnace of knowledge, ideas and precious advices, and I could not be more grateful for your professional and personal support.

Prof. Neri Oxman, my co-supervisor: you opened the doors of MIT for me, fulfilling one of my childhood dreams. Working with you has pushed me out of my comfort zone and taught me how science and engineering can cooperate with design, architecture and art, and how the latter can look back at nature and become a formidable vehicle for its messages. Every time we talk, you enrich my perspectives with powerful, outside-the-box thoughts.

Thanks to Prof. Enrico Bernardo: your hints and help have guided me to new and fruitful approaches in problem solving.

I would like to thank all my colleagues of the Advanced Ceramics and Glasses group in Padova, and in particular Andrea Zocca, Hamada Elsayed, Alberto Conte, Paolo Scanferla, Johanna Schmidt and Chengying Bai. I have learned so much from your knowledge and experience working side by side with you! Sharing pain and joy has sweetened the first and enhanced the second. You are a big part of this work, and the only ones with which I can genuinely celebrate crack-free samples, spanning structures and pure crystal phases.

To the whole DII lab crew: the way we all rely just on coffee and pastries is unique, and so are our nerdy discussions over lunch. Thanks for highlighting the funny side of science!

A special thanks goes to the students that worked with me over these years: Marco Cattaldo, Luca Zeffiro, Larissa Wahl and Filippo Gobbin: your help in conducting experiments and measurements was precious, and I hope I was a good guidance for you.

A gigantic thanks goes to the Mediated Matter group: from the very first day at MIT I felt part of your amazing family: thank you for your warm welcome and for all we shared – I love the way you develop projects and the curiosity that drives everyone towards each other! Sunanda Sharma, thank you for being my fellow scientist in such a diverse team, an outreach passionate and a great

friend! Kelly Donovan, you have been the best guidance through the jungle of bureaucracy, always able to find the best solution to my cases: without you, my stay in US would have been impossible.

Special thanks to the Glass Team: John Klein, my “boss” and companion for the countless nights spent on (re)building and testing our moody Roxanne; Chikara Inamura, my favorite, sleepless ninja and the greatest team builder; Michael Stern, the most pragmatic engineer and passionate glass-blower I ever met; Daniel Lizardo, my enthusiast fellow materials scientist; Markus Kayser, a real maker, who proved me that functionality can always rhyme with elegance.

Peter Houk, thank you for having taught me how to – quite literally – put hands on glass: glass blowing with you was mind blowing! Your experience and competence have fed my understanding, and your explorative perspective of science and art has pushed my limits further and further.

I would like to thank all other people who contributed to the work here presented: Erika Zanchetta, Martin Schwentenwein, Johannes Homa and Prof. Giovanna Brusatin, for working out the chemistry and the printing aspects of the stereolithography of a preceramic polymer; Emilia Gioffredi and Annalisa Chiappone, for their help with the rheological measurements of the hardystonite inks; Andrea Baliello, Giovanni Giacomello and Prof. Marco Pasetto, for their guidance in the use of the rheometer for the geopolymeric inks; James Weaver, Pierre-Thomas Brun, Shreya Dave and Prof. Maria Yang, for their various, precious insights and contributions to the glass printing project.

For keeping my life balanced and for dragging me out of the lab, thanks to all my friends in Padova and all over the world! You keep me sane with our chatting, cooking, travel planning and music, and make me feel at home anytime I am with you.

Alessandro: thank you for your love and your support over these years; being with you enriches my life in all possible ways. I love your ambition and curiosity, and how they stimulate mine; I love how we truly believe in each other: together with you I feel invincible; and, of course, I love you!

I would like to conclude from where it all started: my family. Silvia, I could not be prouder of the woman you are becoming: ambitious, determined, and brilliant. We still make the greatest laughs on something only us can get, and I am sure this will not change. To my parents: I owe you everything, every success and every opportunity; thank you for transmitting me your curiosity, your love for travelling, knowledge and art. Dad, it is following your path that I proudly became an engineer; Mum, I owe you the passion for foreign languages, cultures, and outreach. Thank you for all your support and encouragement.

Grandpa, this is dedicated to you, my #1 supporter.

Abstract

This research project focuses on the production of ceramics via Additive Manufacturing (AM) techniques, with particular focus on extrusion-based technologies. The main advantage of AM is the ability to produce cellular structures with high complexity and controlled porosity, allowing to manufacture light but efficient stretch-dominated structures. The inspiration comes from nature: bone architectures are a great example, consisting of thin, solid skins attached to highly porous, cellular cores.

Very few commercially available AM systems are suited for ceramic materials, and most of them use ceramic powders as feedstock. Residual pores and cracks are very hard to avoid and result in low strength, poor reliability and loss of unique material properties such as glass optical transparency. AM technologies employing polymers are at a much more advanced stage of development. The goal has been to exploit such advances and to provide alternatives to the ceramic powder-binder approaches. Three different material families were explored: preceramic polymers, geopolymers, and glass.

The same preceramic polymer, a commercial polysilsesquioxane, was employed as a non sacrificial, reactive binder to develop inks for stereolithography (SL) and direct ink writing (DIW).

The first technology allowed for production of dense, crack-free SiOC micro-components with strut size down to $\sim 200 \mu\text{m}$ and optimal surface quality. No shape limitations were experienced, but porous structures or small dense parts are the best options in order to avoid residual pores and cracks. The second approach was employed for the fabrication of complex biosilicate scaffolds for tissue engineering with a rod diameter of $350 \mu\text{m}$ and unsupported struts. The preceramic polymer had the double role of source of silica and rheology modifier. Ceramic matrix composites (CMCs) were also fabricated; the preceramic polymer developed the ceramic matrix (SiOC) upon pyrolysis in inert atmosphere, whereas reinforcement was given by chopped carbon fibers.

Geopolymer components with controlled porosity were designed and produced first by negative replica of PLA sacrificial templates and then by DIW. Highly porous ceramic components with features of $\sim 800 \mu\text{m}$ and unsupported parts with very limited sagging were produced with the latter approach.

A novel extrusion-based AM approach was finally developed for the production of objects starting from molten glass. The system processed glass from the molten state to annealed components of complex, digitally designed forms. Objects possessing draft angles and tight radii were fabricated. Within the design space it was possible to print with high precision and accuracy; parts showed a strong adhesion between layers, and high transparency through the layers.

Table of contents

Research Motivation	1
Thesis Organization.....	3
Background.....	5
Additive Manufacturing and ceramics.....	5
Fused Deposition Modeling.....	8
Direct Ink Writing	9
Stereolithography.....	12
Negative replica.....	14
References.....	16
1. Preceramic polymers	21
SL of SiOC from a preceramic polymer	25
Materials and methods.....	25
Material Synthesis	25
2D soft-lithography optimization experiments	26
Production of 3D SiOC microcomponents.....	26
Characterization	28
Results and discussion	29
Conclusions.....	34
DIW of hardystonite from a preceramic polymer and fillers.....	35
Materials and methods.....	36
Ink preparation.....	36
Rheological characterization	37
DIW and ceramization of hardystonite 3D scaffolds	39
Characterization	40
Results and discussion	40
Rheological characterization	40
Production and characterization of porous scaffolds.....	45
Crystalline phase assemblage.....	49
Physical and mechanical properties of the scaffolds	51
Conclusions.....	52

DIW of Ceramic Matrix Composites (CMCs) from a preceramic polymer and fibers	53
Materials and methods.....	55
Ink preparation	55
Direct ink writing and ceramization of C/SiOC structures	57
Characterization	58
Results and discussion	59
Conclusions	65
References.....	67
2. Geopolymers	75
Negative replica of PLA printed structures with geopolymers.....	81
Materials and Methods.....	81
Slurry preparation	81
Negative replica of PLA sacrificial templates.....	82
Characterization	83
Results and Discussion	83
Conclusions	89
DIW with geopolymeric inks	90
Materials and methods.....	90
Ink preparation	90
Rheological characterization	91
Direct Ink Writing	92
Physical and mechanical characterization.....	93
Results and discussion	93
Rheological properties of the inks.....	93
Production and characterization of porous lattices	103
Case study	106
Conclusions	108
References.....	109

3. Glass.....	113
Materials and methods.....	115
Glass 3D Printer (G3DP).....	115
Materials and process characterization	117
Parts fabrication and characterization	118
Results and discussion	119
Materials and process characterization	119
Characterization of the printed objects	125
Case studies.....	128
Conclusions and Future Work.....	130
References.....	131
Summary and conclusions	133

Research Motivation

Up to recent times, materials scientists and engineers have focused on the understanding of the physical and chemical properties of polymers, ceramics and metals, in order to determine their mechanical, thermal, and functional behavior. Manufacturing technologies have been developed with the aim of exploiting the intrinsic properties of materials, such as the low melting point of polymers and the ductility of metals; microstructure modification and material functionalization have been so far the result of post processing treatments such as quenching, etching, and coating.

Materials development has produced synthetic materials, which in some cases possess properties, which are superior to biological based materials; however, natural materials are still unbeatable in terms of their architecture.

Over the past millennia, nature evolved extremely efficient cellular materials, which combine low density with high stiffness and strength; bone architectures are a great example, consisting of thin, solid skins attached to highly porous, cellular cores. Skin thickness, core cell shape, size and distribution vary among species and with respect to the specific bone function: a typical bird's wing bone is much lighter and porous than a human femur. Within the same bone, gradient in density and morphology can be observed.

Human-developed cellular architectures are much less intricate: to date, market-ready manufacturing technologies limit the choice to foams and honeycombs. Structure control is crucial as it determines the behavior of the cellular material. The randomness typical of foams results in bend-dominated deformation and a rapid decrease in strength and stiffness with porosity. A linear decrease could potentially be achieved by stretch-dominated ordered lattices.

Unique opportunities associated with the design and production of complex cellular architecture are now being provided by the special combination of materials engineering with computational design and additive manufacturing (AM). AM technologies are enabling the actual fabrication of cellular components with much less limitations compared to the conventional routes; computational power and methods, on the other hand, have been improved and are now able to design intricate architectures for specific functions.

The cooperation between these worlds enables the application of topological optimization and architectural principles that already increased the efficiency of buildings and structures to the material scale. It results in an additional degree of freedom for material design, which could be manufacture to tailor location-specific requirements.

The same material can double its function within the same component, being a structural element, with high strength/density ratio, but also a thermal insulation or a permeable membrane.

The intrinsic property of the bulk material is the upper bound that defines the mechanical properties of the cellular component. Therefore, efforts are rapidly moving from AM of polymers to metals and ceramics. By fabricating lattice structures of extreme materials, such as technical ceramics, ceramic matrix composites (CMCs) and ultimately diamond, unprecedented strength/density ratios can be accessed.

Among the many commercially available AM systems, very few are suited for ceramic materials, and most of them use ceramic powders as feedstock. Due to the high melting point of ceramics, consolidation of powder to a dense part is a big challenge, and residual porosity is yet very hard to avoid. Residual pores and cracks are responsible for the low strength and poor reliability of additively manufactured ceramic parts; moreover, they inhibit unique material properties such as glass optical transparency due to the light scattering.

Inner porosity, on the other hand, could also provide for the desirable functional features in the design and fabrication of multifunctional materials with graded, hierarchical structures.

As polymeric materials possess unique formability and a much lower melting point compared to ceramics, AM technologies employing polymers are at a much more advanced stage of development. The motivation driving this research has been to exploit such advances and to provide alternatives to the ceramic powder-binder approaches, which could potentially overcome the aforementioned limitations. The potential of these technologies to meet the high demand of complex architected components with superior mechanical properties and additional functionalities would open the way to high-end applications in lightweight structures, energy absorption, thermal management, biomedical engineering and responsive metamaterials.

Thesis Organization

The state-of-the-art of AM for ceramic materials will be presented in the Background, with focus on the technologies employed over the course of this PhD work.

Chapter 1 reports on the use of a preceramic polymer to develop inks for stereolithography (SL) and direct ink writing (DIW). Contrary to conventional organic binders, preceramic polymers have a low decomposition mass loss, so they can be considered as non-sacrificial binders. Pure preceramic polymer inks were developed, as well as composition in which they behave as reactive binders to form complex silicate phases or as matrix in a CMC.

Chapter 2 focuses on geopolymers, a class of ceramic materials synthesized from aluminosilicate powders in alkaline or acidic environments by a polycondensation reaction, which resembles the polymeric ones. Lattices were fabricated first following a negative replica route, and then developing slurries with optimized rheology for DIW. Their applications range from low-CO₂ emissions concrete to filters for air and water depuration.

Chapter 3 presents the development of a novel extrusion system for soda-lime glass able to process it from a molten state to an annealed product. Soda-lime glass is a much more traditional material compared to preceramic polymers and geopolymers; its amorphous structure and glass transition correspond to a gradual variation of its properties upon heating/cooling. Most polymers possess the same behavior, which is exploited in AM processes such as fused deposition modeling (FDM); the biggest challenge involved in the a FDM approach applied to soda-lime glass resided in the development of a platform able to operate at much higher temperatures.

Background

Additive Manufacturing and ceramics

Solid Freeform Fabrication (SFF) technologies enable the manufacture of three-dimensional (3D) structures based on a layer-by-layer approach starting from Computer-Aided Design (CAD) models. After the development of stereolithography (SL) in the 1980s [1], numerous competing SFF technologies have been introduced and improved with the focus moving from rapid prototyping to production of finished and functional devices. Additive Manufacturing (AM) systems based on SFF technology eliminate tooling costs, making small-scale production feasible and cheap and increasing flexibility; less material is wasted and generally less energy is consumed, resulting in a “greener” production compared to conventional manufacturing routes. AM has the peerless ability to produce designs impossible to build otherwise; additional complexity does not affect production rate, cost, or quality. Rapid and economic design iterations exploit the efficacy of non-linear design and optimization.

According to the American Society for Testing and Materials (ASTM), AM is defined by the “process of joining materials to make objects from 3D model data, usually layer upon layer, opposed to subtractive manufacturing methodologies, such as traditional machining” [2].

In contrast, subtractive fabrication techniques construct the manufactured object by successively removing material from a solid block; most machining processes such as milling, grinding and turning are part of this family. Finally, mechanically shaping a set amount of material i.e. by bending, forging or forming, is known as formative fabrication.

The feedstock material for AM processes can be employed in form of powder, liquid, slurry, filament or sheet. It can be directly deposited only in the position giving the desired shape of the final object, or it can be deposited forming a complete layer and consolidated only where needed [3].

Based on these criteria, ASTM divided AM technologies into seven categories [2]:

- **Material extrusion:** material is selectively dispersed through a nozzle or orifice (e.g. direct ink writing (DIW) or robocasting, fused deposition modeling (FDM)).
- **Material jetting:** droplets of build material are selectively deposited (e.g. direct inkjet printing, DIP).
- **Binder jetting:** a liquid bonding agent is selectively deposited to join powder materials (e.g. powder based 3D printing).
- **Sheet lamination:** sheets of material are bonded to form an object (e.g. laminated object manufacturing, LOM).

- **Vat photopolymerization:** liquid photopolymer in a vat is selectively cured by light-activated polymerization (e.g. Stereolithography (SL)).
- **Powder-bed fusion:** thermal energy selectively fuses regions of a powder bed (e.g. selective laser sintering/melting (SLS/SLM); selective electron beam melting).
- **Direct energy deposition:** focused thermal energy fuses a material by melting it as it is deposited.

Material extrusion, material jetting and direct energy deposition are known as **direct** AM manufacturing technologies, as the material is deposited only where the objects is; binder jetting, sheet lamination, vat photopolymerization, powder-bed fusion are classified as **indirect** processes, meaning that they require the deposition of a layer on which the object cross-section is inscribed. In the latter case, the excess material has to be removed at the end of the print; at the same time, it provides a support for the successive layers. Direct technologies, on the other hand, often require the addition of sacrificial structures to support large overhangs, which are time consuming and can be difficult to remove.

It is also true that indirect processes do not allow for the production of objects with closed porosity, as there is no way to remove the excess material trapped inside it; even in the case of small open pores and cells, the unreacted material can be difficult to remove completely. In the case of powder-bed fusion or binding, partially sintered/bonded particles affect the surface finish of the manufactured object significantly.

Indirect technologies can potentially be faster, as the cross-section can be inscribed over the entire layer surface; simultaneous production of multiple objects is also enabled. Direct AM, instead, can only deposit material in sequence.

AM technologies that are based on the processing of polymeric and metallic materials, have been so far the most successful. Even multi-material textures and functionally as well as compositionally graded structures can be fabricated during the manufacturing process [4,5]. Direct AM appears more promising in the combination with multi-material systems, also including ceramics (functional gradients, ceramic/plastic and ceramic/metal interfaces). Indirect technologies show much more limitations, e.g. the addition of metallic materials acting as conductor in multilayer ceramic systems is possible just for small concentrations [6].

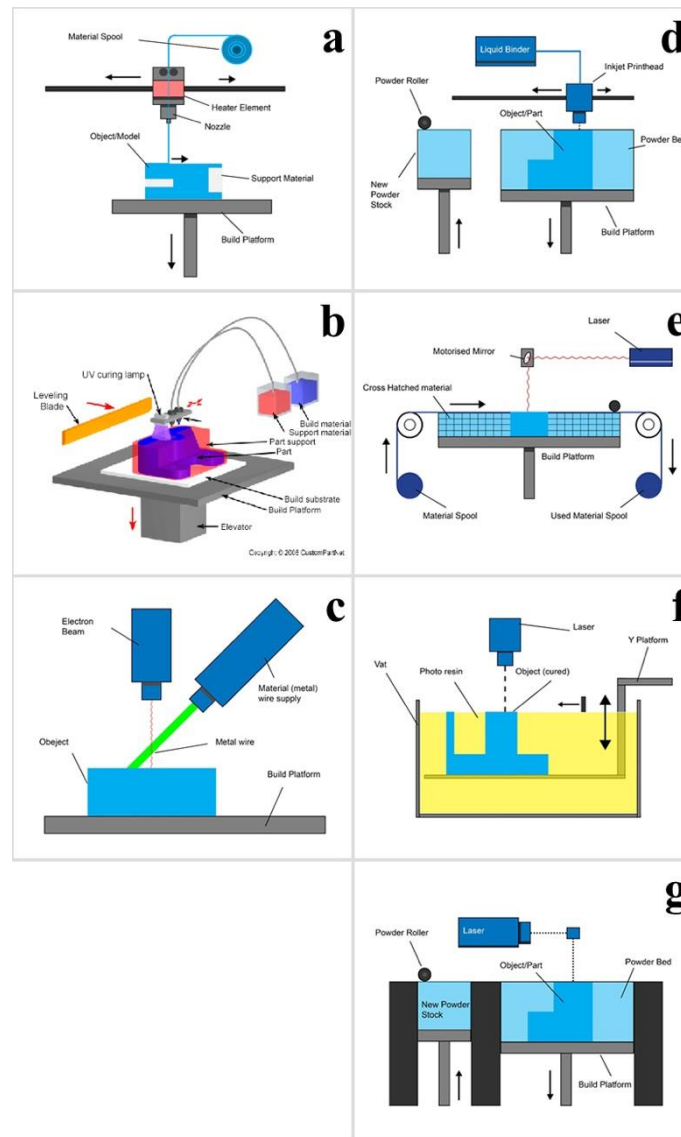


Fig. 1.1 - The seven categories of AM [7]. (a) Material extrusion, (b) Material jetting and (c) Direct energy deposition form the group of direct technologies; (d) binder jetting, (e) sheet lamination, (f) VAT photopolimerizaton and (g) powder-bed fusion are grouped under indirect processes.

As the focus is moving from design and prototyping task to the production of functional objects with adequate physical properties, there are technical challenges in AM of ceramics still being faced by most technologies. Most work in the field has been so far on fabrication of porous structures such as lightweight lattices, scaffolds for tissue engineering, filters and catalyst carriers. Many of the current direct AM technologies are intrinsically suited for the production of structures with a fine mesh, and enable the production of lattices with a control on the amount, direction and shape of the pores impossible to get otherwise; in this sense, AM is not competing with traditional manufacturing, but rather, opens new fields of research.

Mentioned applications are more forgiving, as a certain amount of random porosity is tolerated or even desired in order to provide more functionality.

Fully dense, monolithic ceramics, on the other hand, show superior mechanical properties, thermal resistance and durability; so far, very few AM technologies have the potential to fabricate components with these features, limiting the industrial impact of this production route. The biggest issue relies in the only partial processing of the objects during the fabrication: in most cases, the product is a green body which needs to be sintered or converted to ceramic with the same limitations involved in conventional manufacturing. The need of specific expertise and equipment, such as high temperature furnaces, restricts the user field to people already dealing in ceramic production or research.

The following paragraphs will focus on the state-of-the-art of the AM technologies applied to ceramic materials and relevant for this work of research; their suitability for fabrication of both porous and monolithic components will be discussed in detail, and several examples will be presented.

Fused Deposition Modeling

Fused Deposition Modeling (FDM) is today considered one of the most popular technologies, as it is employed in most desktop machines for the production of polymeric parts. The easiest approach to adapt this relatively cheap technology to ceramic manufacturing to prepare a mixture of ceramic powder and a relatively high amount of polymer. As the printing head is heated, the polymer melts and is extruded in a filamentary form; it then solidifies upon cooling and thus retain the shape of the extruded part. The main drawback resided in the feedstock preparation: ideally, a continuous filament should be produced, which would be flexible enough to be collected in spools and continuously fed to the printing head. However, it is very hard to produce such a filament with a high ceramic loading, as it immediately becomes too brittle. The high amount of polymer needed can cause issues during subsequent burning and sintering of the parts.

First attempts used commercially available FDM printers for polymers (i.e. by Stratasys Inc., Eden Prairie, MN) for production of silicon nitride component [8]. Functional ceramics such as PZT were also successfully produced by FDM: Bandyopadhyay et al. produced a polymeric filament spool loaded with 50-55% PZT powder and used it with a commercial machine to fabricate a 3-3 piezocomposite ladder structure after sintering and impregnation with epoxy resin [9]. Jafari et al. developed a proprietary apparatus with four deposition units and used it to fabricate more complex piezoelectric components, i.e. a multilayer transducer composed on soft and hard PZT [10].

With the same machine, Allahverdi et al. also demonstrated fabrication of BiT structures and of alumina structures with photonic bandgap properties [11].

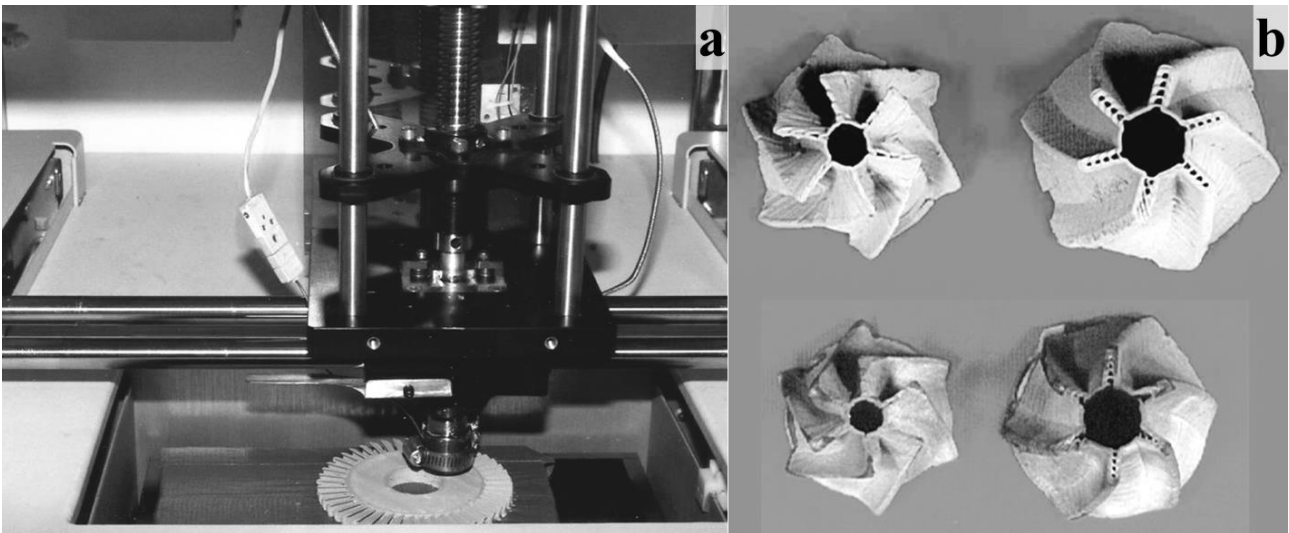


Fig. 1.II- (a) FDM extrusion head creating a ceramic prototype; (b) green and sintered silicon-nitride parts [8].

Grida et al produced zirconia components from a mixture of 55% zirconia in wax and tested different nozzles with diameter ranging from 76 to 510 μm [12]; they observed that when the filaments are too fine, they solidify too quickly in air.

For what concerns bio-related applications, Park et al. printed scaffolds with a mixture of 40% hydroxyapatite (HA) and polycaprolactone (PCL) and measured the influence of the patterned shape on the compressive modulus [13]; they also conducted in vitro tests with osteoblast-like cells, as the scaffolds are meant for application in bone tissue engineering.

Polypropylene-tricalcium phosphate (TCP) composites with a pore size of 160 μm were fabricated by Kalita et al. [14]; resulting in a total porosity of 36%, they possessed a compressive strength of 12.7 MPa.

Direct Ink Writing

Direct Ink Writing (DIW), originally known as Robocasting after Cesarano's patent [15], is a layer by layer fabrication technique that involves the robotic deposition of a viscous ceramic paste extruded through a fine nozzle. Central to the approach is the creation of an ink that can be extruded in form of a filament; it then needs to solidify rapidly to maintain the shape of the printed structures, which is particularly challenging if the filaments span gaps in the underlying layer(s). Appropriate rheological properties for the ink are therefore an essential requirement.

Robocasting originally exploited the evaporation of the solvent as mean of rapid solidification for ceramic suspensions with high solid loading; the minimal drying of the slurry after extrusion in air converts it from a pseudoplastic to a dilatant behavior. This approach, however, limits the nozzle size to a minimum of 0.5 mm, otherwise clogging occurs.

A partial solution is the deposition in a non-wetting bath, often constituted by oil, which prevents excessive drying. Different ways of achieving the desired rheology can also overcome this issue.

The ideal rheology for a DIW ink is that of a Bingham pseudoplastic fluid, i.e. a fluid who shows an initial yield stress and whose viscosity decreases with the increasing shear rate. In this way, the ink can be easily extruded at low pressure but is able to retain its shape once deposited, even in case of suspended struts. Such behavior is typical of a reversible gel and can be achieved in several ways, including flocculation of a ceramic suspension to form a gel (e.g. by a change in pH, ionic strength of the solvent, addition of polyelectrolytes), or the formulation of a ceramic ink containing a polymeric binder and plasticizer [16]. The use of polyelectrolytes and salts for tailoring of the pH is complex and requires a specific characterization of each suspension, i.e. measurement and adjustment of its zeta-potential. Moreover, ions in the solution can interfere with the ceramic particles: it is the case with bioglass, which was bound to dissolve and leach ions in water due to pH modification [17]. The blend with a polymer binder and a plasticizer is less dependent from the ceramic in use, but requires a de-binding step to remove the organic part; for lattices with a fine mesh, no defects generated by such additional step were detected [18]. Another possibility is the use of gelling additives, which is favorable because it makes use of a very little amount of organic additives, therefore making a dedicated de-binding step unnecessary [19]. The same bioglass suspension mentioned above was successfully dispersed using carboxymethyl cellulose, which also behaves as a reversible gel former [17].

As clogging of the nozzle does not affect the latter cases, the size of the nozzle and of the corresponding extruded filament can shrink down to 100 μm [20,21]; the choice of the nozzle is usually a compromise between processing time and surface quality. It is also possible to produce specific cross-sections by using squared, hexagonal or more complex nozzles [22]; even hollow filaments can be extruded [23].

The green bodies usually have a density up to 60%, which enables an almost complete densification of the sintered parts.

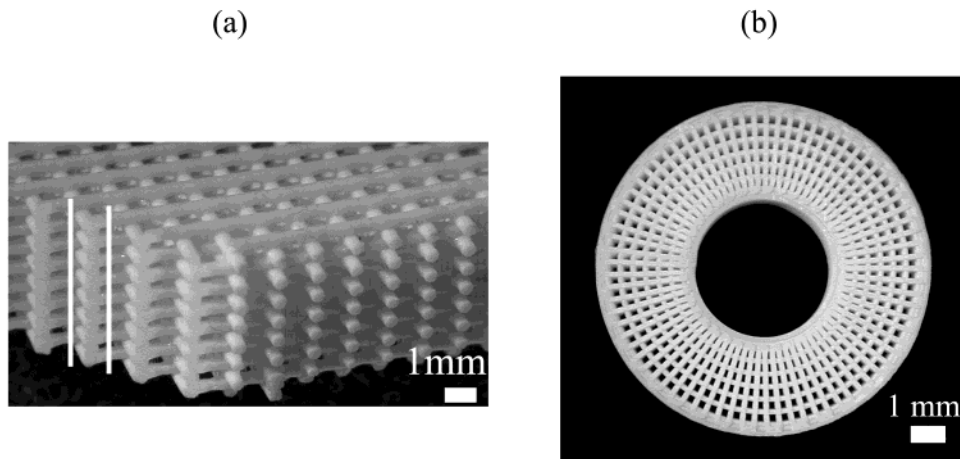


Fig. 1.III - (a) a 3D periodic structure with a simple tetragonal symmetry of lattice and (b) a 3D radial structure comprised of alternating layers deposited using radial and concentric fill patterns [24].

Even so, the deposition in a filament fashion has so far shown its limitations in the fabrication of monolithic parts, as it generates surfaces with a rough surfaces and voids at the interface between layers; this is also the case for FDM approaches. Moreover, the presence of a binder or organic additives can also translate into residual porosity or gas formation during de-binding. The mechanical properties of such components are affected by these irregularities and the properties along the vertical direction are usually much lower than the bulk ones.

Experimentation with porous components, on the other hand, has been particularly successful. Most of the research has been oriented on the fabrication of porous bioceramic scaffold, which are particularly suited for bone tissue engineering applications. For this reason, mechanical properties have been carefully analyzed and correlated to the porosity of the scaffolds, as they should be able to withstand some load. Miranda et al. printed hydroxyapatite (HA) scaffolds with a total porosity of 39% and 15% of microporosity of the struts [25]; their compressive strength under uniaxial load was ~ 50 MPa, and it doubled after immersion for two weeks in simulated body fluid (SBF) [26]. Porosity within the struts was found to be significant by Franco et al.: they printed several types of bioceramic scaffolds by developing a thermo-reversible gel ink which has a low viscosity when extruded at low temperature, but undergoes gelation when deposited into a warm ($60\text{ }^{\circ}\text{C}$) oil bath [27]. An increasing amount of gelling agent resulted in a porosity of the struts increasing from 5% to 40%, which translated in a compressive strength decreasing from ~ 25 MPa to ~ 2 MPa.

Fu et al. were able to achieve fully dense bioglass struts on scaffolds with 60% total porosity [28]. The mesh of the scaffold was very anisotropic with unidirectional pores, and so was the compressive strength: they reached 136 MPa in the channels direction and only 55 MPa in the perpendicular one. These values can be fitted well with the Gibson-Ashby model for cellular ceramics with closed pores [29].

A model of the compressive strength of HA scaffolds was developed by Genet et al. based on a Weibull approach and compared it with own experimental data [30]. They first kept the diameter of the strut constant and gradually increased the spacing between the struts and so the porosity and experienced a decrease in the compressive strength; they then kept the porosity constant (45%) and increased both the spacing and the diameter of the struts, and they found a decrease of almost 75% of the compressive strength. The model proposed showed a good accordance with the experimental data.

Good results have been shared also in other, non bio-related fields of applications: mullite lattices with 100 to 1000 μm pore sizes were printed by Stuecker et al. with a sintered strut density of 96% [31]. Radial struts arrays with increasing spanning distances were printed by Smay et al. with a strut diameter of 200 to 400 μm and a spacing of 300 to 1200 μm [24]. The same ink was used to produce PZT components for ultrasonic sensing applications [32]. Infiltration with an epoxy resin resulted in PZT-polymer composites with 2-2 connectivity. Complex phases were also produced by Smay et al., which used a nozzle mixer to print ternary mixtures of BaTiO_3 , BaZrO_3 , SrTiO_3 [33]. They also presented one of the first examples of multi-material printing as they fabricated Ni- BaTiO_3 metal-ceramic structures through an array of single nozzles.

As already mentioned, for certain applications, some amount of porosity within the struts is desirable as it decreases the weight of the component and increases its aspect ratio. Such porosity can be designed by adding a porogen to the ink [34,35]. Dellinger et al. produces scaffolds with a porosity gradient: macropores (100 – 600 μm) obtained through the printing process, micropores (1-30 μm) produced by PMMA microsphere addition to the ink, and submicron pores (< 1 μm) due to incomplete sintering [35].

Stereolithography

Stereolithography is historically the first developed AM technology and consists of the selective photopolymerization of a liquid resin with a UV light. The resin can be filled with ceramic particles forming a slurry typically including a monomer solution, a photo-initiator, an absorber and dispersing agents; concentrations of 40-60 vol% can be achieved [36–39].

Even if SL is an indirect AM process, the material surrounded the cross-linked part is liquid and therefore cannot provide sufficient support; support structures need to be built and removed after printing [39]. Thanks to the use of fine ceramic particles and the high green densities achievable, almost dense ceramic parts can be produced [37]. Moreover, layer inscribing through a light source allows for a much higher resolution compared to DIW and FDM; theoretically, it is limited by the biggest between the pixel area and the particle size.

On the other hand, there are material limitations associated with the light absorption: SiC components, for example, cannot be fabricated via SL. Kiriwara et al. experimented with several materials producing samples possessing an ordered porosity of 75 vol% [40]. They produced yttria-stabilized zirconia (YSZ) lattices with 100 μm thick struts and 250 μm lattice constant as anodes for solid oxide fuel cells; alumina diamond-like structures served for simulation and measurement of photonic properties. Chartier et al. also fabricated alumina 2D porous meshes [41].

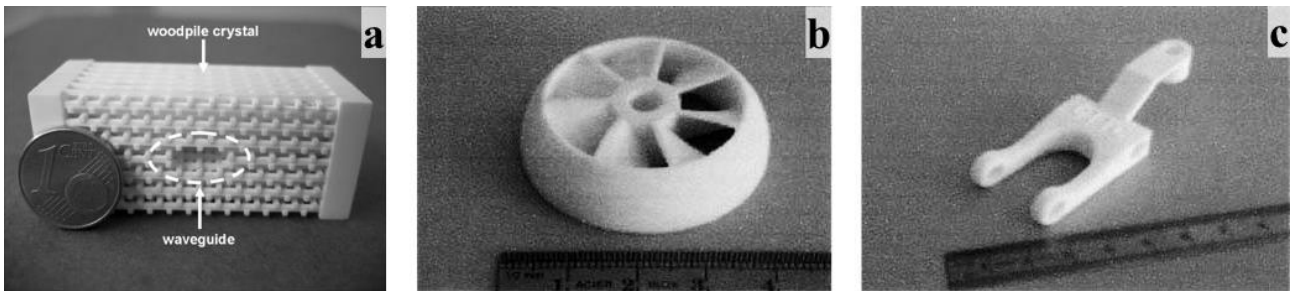


Fig. 1.IV- (a) Elaborated 3D zirconia woodpile crystal having a waveguide within it [36]; (b) and (c) Examples of alumina sintered pieces [41].

HA implants were also produced by means of SL; Kiriwara et al. fabricated a dendrite structure with graded porosity and a strut density between 95 and 98% [40]. Chu et al. produced scaffolds with orthogonal pores, with a designed porosity of 40% and a compressive strength of 30 MPa [42]. SL was also combined with freeze casting for producing β -TCP-type 1 collagen composite scaffolds inspired by the osteochondral cartilage [43].

A much more recent development of SL, namely nano-stereolithography, makes use of a two-photon equipment to achieve resolutions down to 200 nm. In this case, the structure is built in a voxel-by-voxel fashion. Stable ceramic suspensions with particles smaller than 200 nm are difficult to obtain, and so far the best results have been reached by using preceramic polymers to obtain SiCN complex micron-sized structures upon pyrolysis in nitrogen [44]. $9 \times 9 \times 9 \mu\text{m}^3$ structures with an average cell size of 1 μm were reported.

Of the technologies presented, SL is the most promising for the production of monolithic components. The critical step in achieving full density is de-binding: when it is thermally activated, it transforms the binder and additives into gaseous species which can leave pores and defects behind as they leave the bulk by diffusion.

Heating must be very slow as the pressure inside the part cannot increase to much, otherwise cracks and voids will form.

Such issues are well known also in conventional manufacturing such as injection molding [45]; it was shown that the limiting factor is the maximum wall thickness or volume of the green body, as for wall thicknesses of ~1 cm, thermal treatment would require several days [46].

Negative replica

A possible solution for some of the limitations of the AM of ceramics is a negative replica approach, where molds or porous structures are printed, impregnated with a ceramic slurry and then the molds are removed. Molds can be produced from AM of polymeric materials, whose development is at a greater stage compared to ceramics and offers easier processes, better resolution and surface quality. Moreover, the final ceramic part can be more homogeneous and possess a uniform microstructure when the template is filled with suitable slurry. Finally, the requirements in terms of rheological behavior for the infiltrating slurries are much less stringent in comparison to the strict control required for the fabrication of high quality structures by DIW. However, infiltration can also be a delicate process, especially for complex lattices with fine, intricate channels.

Bose et al. fabricated 3D honeycomb TCP and alumina structures for bone implants by infiltrating a polymeric mold created by stereolithography with a ceramic slurry [47]. Porous components produced by negative replica were developed almost exclusively for tissue engineering applications. Preliminary attempts involved manual building of predesigned macroporous architectures where sugar porogen elements were stacked layer-by-layer to form uniaxial, orthogonal and helicoidal networks in polymeric structures [48]. A few years later, PLA and PLA-HA scaffolds were fabricated by casting in 3D printed wax/PSA molds. The same route was followed by Ma providing highly accurate inverse replicas with promising features for tissue engineering applications [49]. Different technologies can be employed to produce the molds: Detsch et al. produced a wax mold with dropwise deposition and infiltrated it with a HA slurry [50]; they also replicated the geometry by DIW. Negative replica produced scaffolds with 44% porosity, whereas components fabricated via DIW had a porosity of 37%.

The pore size (300 μm) and strut diameter (500 μm) were the same and in both cases the strut relative density reached 96% after sintering. This result indicates that the two techniques are fully interchangeable. Also Bandyopadhyay et al. compared piezocomposites produced with FDM and negative replica approach [9].

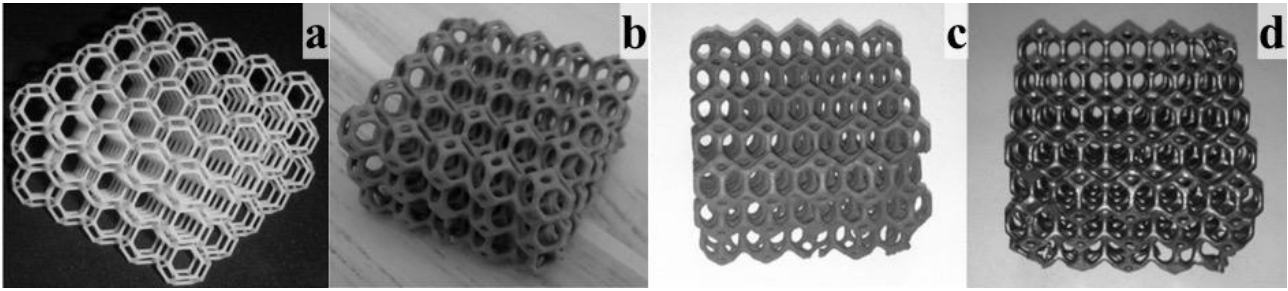


Fig. 1.V - The manufacturing procedure: (a) template, (b) slurry replication, (c) pyrolysis, (d) silicon infiltration [51].

SL resin molds were fabricated and impregnated with HA following a gel-casting approach in order to increase the strength of the green body [52]; similar molds led to the fabrication of diamond-shaped $\text{TiO}_2/\text{SiO}_2$ photonic crystals [53]. Guo et al. produced PZT components by gel-casting into selective laser sintered (SLS) polystyrene molds; they found out that a proper polymer and corresponding decomposition treatment need to be selected accurately in order to avoid deformation of the parts [54]. Ortona et al. produced complex, regular three dimensional cellular structures through a Polyjet approach, and they coated it with a SiC slurry; after pyrolysis, the resulting hollow lattice was infiltrated with molten Si to generate RBSiC structures [51].

The combination of porosities and architectures at various scales, gradually decreasing from macro- to micro- and nanostructures is possible and was demonstrated for instance, by Chen et al. with PLLA nano-fibrous scaffolds [55]. Local pores can be manufactured simultaneously with the infiltration process using conventional methods (e.g. using emulsions or adding sacrificial particles to the infiltrating slurry), producing both local and global pores within one sample (often with different length scales, enabling the fabrication of components with hierarchical porosity).

References

- [1] C.W. Hull, Apparatus for production of threedimensional objects by stereolithography, (1986).
- [2] ASTM, Standard Terminology for Additive Manufacturing Technologies -, (2012).
- [3] A. Zocca, P. Colombo, C.M. Gomes, J. Guenster, Additive Manufacturing of Ceramics: issues, potentialities and opportunities, *J. Am. Ceram. Soc.* 98 (2015) 1983–2001.
- [4] D.C. Hofmann, J. Kolodziejaska, S. Roberts, R. Otis, R.P. Dillon, J.-O. Suh, Z.-K. Liu, J.-P. Borgonia, Compositionally graded metals: A new frontier of additive manufacturing, *J. Mater. Res.* 29 (2014) 1899–1910. doi:10.1557/jmr.2014.208.
- [5] M. Vaezi, S. Chianrabutra, B. Mellor, S. Yang, Multiple material additive manufacturing – Part 1: a review, *Virtual Phys. Prototyp.* 8 (2013) 19–50. doi:10.1080/17452759.2013.778175.
- [6] W. Kollenberg, Ceramic and Multi-Material 3D-Printing, *Keramische Zeitschrift.* 66 (2014) 233–236.
- [7] Loughborough University, The 7 categories of Additive Manufacturing, (n.d.). <http://www.lboro.ac.uk/research/amrg/about/the7categoriesofadditivemanufacturing/> (accessed October 29, 2016).
- [8] R. Vaidyanathan, J. Walish, J.L. Lombardi, S. Kasichainula, P. Calvert, K.C. Cooper, The extrusion freeforming of functional ceramic prototypes, *Jom.* 52 (2000) 34–37. doi:10.1007/s11837-000-0066-4.
- [9] A. Bandyopadhyay, R.K. Panda, V.F. Janas, M.K. Agarwala, S.C. Danforth, A. Safari, Processing of Piezocomposites by Fused Deposition Technique, *J. Am. Ceram. Soc.* 80 (2005) 1366–1372. doi:10.1111/j.1151-2916.1997.tb02993.x.
- [10] M.A. Jafari, W. Han, F. Mohammadi, A. Safari, S.C. Danforth, N. Langrana, A novel system for fused deposition of advanced multiple ceramics, *Rapid Prototyp. J.* 6 (2000) 161–175. doi:10.1108/13552540010337047.
- [11] M. Allahverdi, S.C. Danforth, M. Jafari, A. Safari, Processing of advanced electroceramic components by fused deposition technique, *J. Eur. Ceram. Soc.* 21 (2001) 1485–1490. doi:10.1016/S0955-2219(01)00047-4.
- [12] I. Grida, J.R.G. Evans, Extrusion freeforming of ceramics through fine nozzles, *J. Eur. Ceram. Soc.* 23 (2003) 629–635. doi:10.1016/S0955-2219(02)00163-2.
- [13] S.A. Park, S.H. Lee, W.D. Kim, Fabrication of porous polycaprolactone/hydroxyapatite (PCL/HA) blend scaffolds using a 3D plotting system for bone tissue engineering, *Bioprocess Biosyst. Eng.* 34 (2011) 505–513. doi:10.1007/s00449-010-0499-2.

- [14] S.J. Kalita, S. Bose, H.L. Hosick, A. Bandyopadhyay, Development of controlled porosity polymer-ceramic composite scaffolds via fused deposition modeling, *Mater. Sci. Eng. C*. 23 (2003) 611–620. doi:10.1016/S0928-4931(03)00052-3.
- [15] J. Cesarano, P.D. Calvert, Freeforming objects with low-binder slurry, US 6027326, 2000.
- [16] J. a. Lewis, J.E. Smay, J. Stuecker, J. Cesarano, Direct ink writing of three-dimensional ceramic structures, *J. Am. Ceram. Soc.* 89 (2006) 3599–3609. doi:10.1111/j.1551-2916.2006.01382.x.
- [17] S. Eqtesadi, A. Motealleh, P. Miranda, A. Pajares, A. Lemos, J.M.F. Ferreira, Robocasting of 45S5 bioactive glass scaffolds for bone tissue engineering, *J. Eur. Ceram. Soc.* 34 (2014) 107–118. doi:10.1016/j.jeurceramsoc.2013.08.003.
- [18] F.C.G. de Sousa, J.R.G. Evans, Sintered Hydroxyapatite Latticework for Bone Substitute, *J. Am. Ceram. Soc.* 86 (2003) 517–519. doi:10.1111/j.1151-2916.2003.tb03332.x.
- [19] Q. Fu, E. Saiz, A.P. Tomsia, Direct Ink Writing of Highly Porous and Strong Glass Scaffolds for Load-bearing Bone Defects Repair and Regeneration, 7 (2011) 3547–3554. doi:10.1016/j.actbio.2011.06.030.
- [20] X. Lu, Y. Lee, S. Yang, Y. Hao, R. Uvic, J.R.G. Evans, C.G. Parini, Fabrication of Millimeter-Wave Electromagnetic Bandgap Crystals Using Microwave Dielectric Powders, *J. Am. Ceram. Soc.* 92 (2009) 371–378. doi:10.1111/j.1551-2916.2008.02907.x.
- [21] S. Yang, K.-F. Leong, Z. Du, C.-K. Chua, The Design of Scaffolds for Use in Tissue Engineering. Part II. Rapid Prototyping Techniques, *Tissue Eng.* 8 (2002) 1–11. doi:10.1089/107632702753503009.
- [22] J.A. Lewis, Direct ink writing of 3D functional materials, *Adv. Funct. Mater.* 16 (2006) 2193–2204.
- [23] T. Schlordt, F. Keppner, N. Travitzky, P. Greil, Robocasting of Alumina Lattice Truss Structures, *J. Ceram. Sci. Technol.* 3 (2012) 1–7. doi:10.4416/JCST2012-00003.
- [24] J.E. Smay, J. Cesarano, J.A. Lewis, Colloidal Inks for Directed Assembly of 3-D Periodic Structures, *Langmuir*. 18 (2002) 5429–5437. doi:10.102/la0257135.
- [25] P. Miranda, A. Pajares, E. Saiz, A.P. Tomsia, F. Guiberteau, Fracture modes under uniaxial compression in hydroxyapatite scaffolds fabricated by robocasting, *J. Biomed. Mater. Res. Part A*. 83A (2007) 646–655. doi:10.1002/jbm.a.31272.
- [26] P. Miranda, A. Pajares, E. Saiz, A.P. Tomsia, F. Guiberteau, Mechanical properties of calcium phosphate scaffolds fabricated by robocasting, *J. Biomed. Mater. Res. Part A*. 85A (2008) 218–227. doi:10.1002/jbm.a.31587.
- [27] J. Franco, P. Hunger, M.E. Launey, A.P. Tomsia, E. Saiz, Direct write assembly of calcium

- phosphate scaffolds using a water-based hydrogel, *Acta Biomater.* 6 (2010) 218–228. doi:10.1016/j.actbio.2009.06.031.
- [28] Q. Fu, E. Saiz, A.P. Tomsia, Bioinspired Strong and Highly Porous Glass Scaffolds, *Adv. Funct. Mater.* 21 (2011) 1058–1063. doi:10.1002/adfm.201002030.
- [29] L.J. Gibson, M.F. Ashby, *Cellular solids. Structure and properties*, (1997) 502. doi:10.1017/CBO9781139878326.
- [30] M. Genet, M. Houmard, S. Eslava, E. Saiz, A.P. Tomsia, A two-scale Weibull approach to the failure of porous ceramic structures made by robocasting: Possibilities and limits, *J. Eur. Ceram. Soc.* 33 (2013) 679–688. doi:10.1016/j.jeurceramsoc.2012.11.001.
- [31] J. Stuecker, J. Cesarano, D.A. Hirschfield, Control of the viscous behavior of highly concentrated mullite suspensions for robocasting, *J. Mater. Process. Technol.* 142 (2003) 318–325. doi:10.1016/S0924-0136(03)00586-7.
- [32] J.E. Smay, J. Cesarano, B.A. Tuttle, J.A. Lewis, Directed Colloidal Assembly of Linear and Annular Lead Zirconate Titanate Arrays, *J. Am. Ceram. Soc.* 87 (2004) 293–295. doi:10.1111/j.1551-2916.2004.00293.x.
- [33] J.E. Smay, S.S. Nadkarni, J. Xu, Direct Writing of Dielectric Ceramics and Base Metal Electrodes, *Int. J. Appl. Ceram. Technol.* 4 (2007) 47–52. doi:10.1111/j.1744-7402.2007.02118.x.
- [34] J. Cesarano, J.G. Dellinger, M.P. Saavedra, D.D. Gill, R.D. Jamison, B.A. Grosser, J.M. Sinn-Hanlon, M.S. Goldwasser, Customization of Load-Bearing Hydroxyapatite Lattice Scaffolds, *Int. J. Appl. Ceram. Technol.* 2 (2005) 212–220. doi:10.1111/j.1744-7402.2005.02026.x.
- [35] J.G. Dellinger, J. Cesarano, R.D. Jamison, Robotic deposition of model hydroxyapatite scaffolds with multiple architectures and multiscale porosity for bone tissue engineering, *J. Biomed. Mater. Res. Part A.* 82A (2007) 383–394. doi:10.1002/jbm.a.31072.
- [36] T. Chartier, C. Duterte, N. Delhote, D. Baillargeat, S. Verdeyme, C. Delage, C. Chaput, Fabrication of Millimeter Wave Components Via Ceramic Stereo- and Microstereolithography Processes, *J. Am. Ceram. Soc.* 91 (2008) 2469–2474. doi:10.1111/j.1551-2916.2008.02482.x.
- [37] M.L. Griffith, J.W. Halloran, Freeform Fabrication of Ceramics via Stereolithography, *J. Am. Ceram. Soc.* 79 (2005) 2601–2608. doi:10.1111/j.1151-2916.1996.tb09022.x.
- [38] J. Homa, M. Schwentenwein, A Novel Additive Manufacturing Technology for High-Performance Ceramics, in: *Adv. Process. Manuf. Technol. Nanostructured Multifunct. Mater.*, 2015: pp. 33–40. doi:10.1002/9781119040354.ch4.

- [39] W. Zhou, D. Li, H. Wang, A novel aqueous ceramic suspension for ceramic stereolithography, *Rapid Prototyp. J.* 16 (2010) 29–35. doi:10.1108/13552541011011686.
- [40] S. Kirihara, Creation of Functional Ceramics Structures by Using Stereolithographic 3D printing, *Trans. JWRI.* 43 (2014) 5–10.
- [41] T. Chartier, C. Chaput, F. Doreau, M. Loiseau, Stereolithography of structural complex ceramic parts, *J. Mater. Sci.* 37 (2002) 3141–3147. doi:10.1023/A:1016102210277.
- [42] T.-M.G. Chu, S.J. Hollister, J.W. Halloran, S.E. Feinberg, D.G. Orton, Manufacturing and characterization of 3-d hydroxyapatite bone tissue engineering scaffolds., *Ann. N. Y. Acad. Sci.* 961 (2002) 114–7. <http://www.ncbi.nlm.nih.gov/pubmed/12081877>.
- [43] W. Bian, D. Li, Q. Lian, X. Li, W. Zhang, K. Wang, Z. Jin, Fabrication of a bio-inspired beta-Tricalcium phosphate/collagen scaffold based on ceramic stereolithography and gel casting for osteochondral tissue engineering, *Rapid Prototyp. J.* 18 (2012) 68–80. doi:10.1108/13552541211193511.
- [44] T.A. Pham, D.-P. Kim, T.-W. Lim, S.-H. Park, D.-Y. Yang, K.-S. Lee, Three-Dimensional SiCN Ceramic Microstructures via Nano-Stereolithography of Inorganic Polymer Photoresists, *Adv. Funct. Mater.* 16 (2006) 1235–1241. doi:10.1002/adfm.200600009.
- [45] T. Chartier, E. Delhomme, J.F. Baumard, G. Veltl, F. Ducloux, Injection moulding of hollow silicon nitride parts using fusible alloy cores, *Ceram. Int.* 27 (2001) 821–827. doi:[http://dx.doi.org/10.1016/S0272-8842\(01\)00036-0](http://dx.doi.org/10.1016/S0272-8842(01)00036-0).
- [46] G.H. Wroblewska, Structural Ceramics with Complex Shape - Forming Methods, in: 25th Annu. Conf. Compos. Adv. Ceram. Mater. Struct. A Ceram. Eng. Sci. Proceedings, Vol. 22, Issue 3, John Wiley & Sons, Inc., Hoboken, NJ, USA, 2001: pp. 43–50. doi:10.1002/9780470294680.ch5.
- [47] S. Bose, Processing of Bioceramic implants via fused deposition modelling, Present. '98 SFF (Austin, TX). (1998) 629–636.
- [48] R. Zhang, P.X. Ma, Synthetic nano-fibrillar extracellular matrices with predesigned macroporous architectures., *J. Biomed. Mater. Res.* 52 (2000) 430–8. doi:10.1002/1097-4636(200011)52:2<430::AID-JBM25>3.0.CO;2-L.
- [49] P.X. Ma, Scaffolds for tissue fabrication, *Mater. Today.* 7 (2004) 30–40. doi:10.1016/S1369-7021(04)00233-0.
- [50] R. Detsch, F. Uhl, U. Deisinger, G. Ziegler, 3D-Cultivation of bone marrow stromal cells on hydroxyapatite scaffolds fabricated by dispense-plotting and negative mould technique, *J. Mater. Sci. Mater. Med.* 19 (2008) 1491–1496. doi:10.1007/s10856-007-3297-x.
- [51] A. Ortona, C. D'Angelo, S. Gianella, D. Gaia, Cellular ceramics produced by rapid

- prototyping and replication, *Mater. Lett.* 80 (2012) 95–98. doi:10.1016/j.matlet.2012.04.050.
- [52] A. Woesz, M. Rumpler, J. Stampfl, F. Varga, N. Fratzl-Zelman, P. Roschger, K. Klaushofer, P. Fratzl, Towards bone replacement materials from calcium phosphates via rapid prototyping and ceramic gelcasting, *Mater. Sci. Eng. C.* 25 (2005) 181–186. doi:10.1016/j.msec.2005.01.014.
- [53] H. Yin, S. Kirihaara, Y. Miyamoto, Fabrication of Ceramic Photonic Crystals with Diamond Structure for Microwave Applications, *J. Am. Ceram. Soc.* 87 (2004) 598–601. doi:10.1111/j.1551-2916.2004.00598.x.
- [54] D. Guo, L. Li, K. Cai, Z. Gui, C. Nan, Rapid Prototyping of Piezoelectric Ceramics via Selective Laser Sintering and Gelcasting, *J. Am. Ceram. Soc.* 87 (2004) 17–22. doi:10.1111/j.1151-2916.2004.tb19938.x.
- [55] V.J. Chen, L.A. Smith, P.X. Ma, Bone regeneration on computer-designed nano-fibrous scaffolds, *Biomaterials.* 27 (2006) 3973–3979. doi:10.1016/j.biomaterials.2006.02.043.

1. Preceramic polymers

Preceramic polymers are a class of inorganic/organometallic polymers which can be converted to a ceramic with high yield. Ceramics resulting from this process are named polymer-derived ceramics (PDC). This novel class of ceramic materials was introduced more than 40 years ago, and it has gained interest within scientists and industry thanks to its processing versatility and outstanding material properties.

Most of preceramic polymers consist of silicon-based molecules; depending on the specific precursor, binary systems such as SiC and Si₃N₄, and more complex systems such as SiOCN or SiBCN can be produced. They can be synthesized at lower temperatures (1000 - 1300 °C) compared to classical powder technology (above 1700 °C) with a lower energy consumption. Some varieties, like SiOC or SiCN, cannot be produced following any other approach but the molecular route.

PDCs exhibit superior oxidation resistance and excellent thermo-mechanical properties (i.e. stability to creep, crystallization, or phase separation) up to and above 1500 °C [1]. Moreover, they can also possess functional properties such as piezo-resistivity, electrical conductivity, luminescence, high chemical durability and favorable non coagulating behavior in contact with blood as well as compatibility with cells [2–7].

The greatest advantage of this class of materials is that they can be processed or shaped using conventional polymer-forming technologies such as infiltration, coating, spinning, extrusion, injection molding and so on. This way, the general drawbacks and shaping limitations of the traditional ceramic processing can be overcome.

PDCs have found application in several key fields such as information technology, transport, defense, energy as well as environmental systems, biomedical components, sensors, and micro or nano-electromechanical systems.

The general formula of an organosilicon polymer comprises a Si atom bonded to another atom or group, forming the polymer backbone, and two substituent groups at the Si atom. The variation of the backbone group determines the polymer class, whereas by changing the functional groups at the Si atom properties such as chemical and thermal stability, solubility and rheology can be tailored. Substituents can also modify the final chemistry of the ceramic, as they provide carbon in the structure.

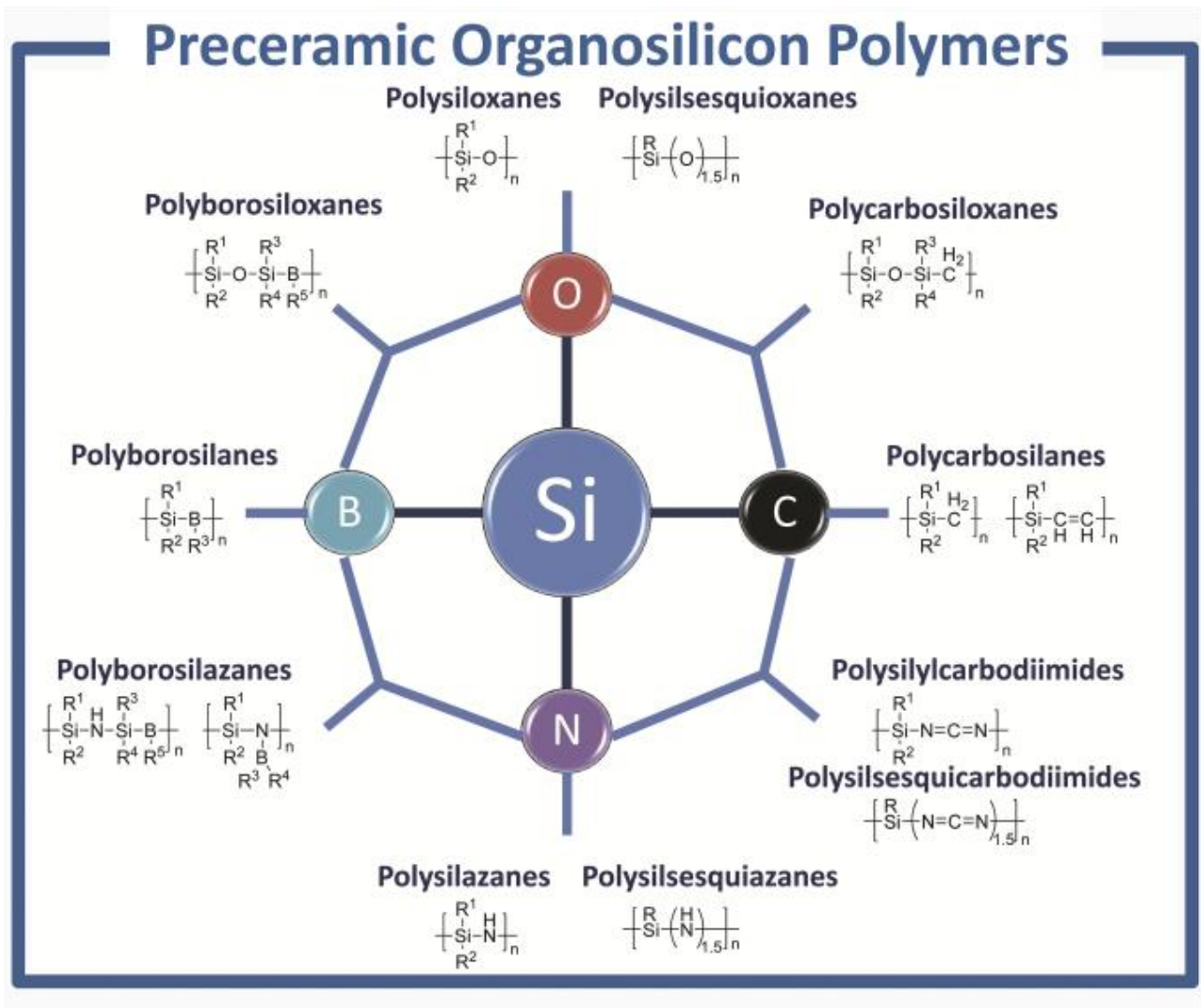


Fig. 1.1 - Main classes of Si-polymer precursors for ceramics [1].

Processing of preceramic polymers can usually be done in three steps:

- 1) **Shaping:** as mentioned, one of the key features of PDCs is that they possess a polymeric nature at forming temperatures; therefore, conventional plastic-forming technologies can be applied. Typically, the precursor is either a cross-linkable liquid, a meltable and curable solid, or an unmeltable but soluble solid.
- 2) **Cross-linking:** after shaping, the component needs to be cured forming a thermoset able to retain its shape upon ceramization. The functional groups (Si-H, Si-OH etc.) spontaneously react via condensation or addition, usually below 200 °C; this thermal cross-linking can be triggered by using catalyst, to the point that cross-linking reactions occur already during shaping. Alternative means besides heating are oxidative treatment, e-beam curing, UV-curing or treatment in alkaline solution [7]. Cross-linking stabilizes the material structure and thus prevents the evaporation of oligomers during heat treatment. This results in a lower release of gases that can form bubbles and defects.

- 3) **Ceramization:** polymer-to-ceramic conversion leads to the decomposition and release of organic groups. The most widely used process is pyrolysis, i.e. thermal treatment to high temperatures. The process and the final composition depend on the precursor, the presence of passive or active fillers, the atmosphere, the heating conditions etc.; however, in most cases a 100% ceramic component can be obtained at about 1000 °C. The results are remarkably stable amorphous phases; when heated at elevated temperatures, phase separation and subsequent crystallization occur.

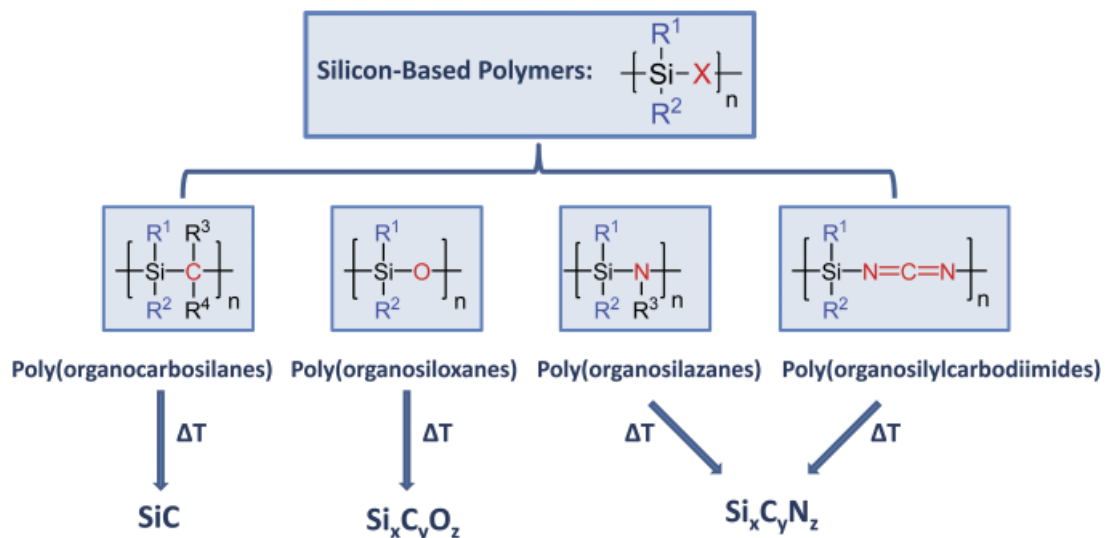


Fig. 1.2 - Thermal decomposition of Si-based polymers [1].

Ceramization occurs with gas release and high shrinkage, leading to large defects such as pores and massive cracks on bulk parts. The main strategy to overcome these limitations has been so far the introduction of fillers.

They can be classified in two main categories:

- 1) **Inert fillers:** they do not react at any stage with the polymer, its decomposition products and ceramic residue and the atmosphere. Their purpose is to reduce the shrinkage and gas release upon ceramization and to provide means of escape for decomposition gases, thus reducing cracking significantly and allowing for production of bulk parts.
- 2) **Active fillers:** these materials can react with the polymer and its decomposition products, the atmosphere or the ceramic residue. A sacrificial polymeric filler can be added to the preceramic polymer as porogen: in fact, it decomposes completely forming pores with size and shape depending on the filler itself. Metallic and intermetallic fillers can react with the decomposition products of the polymer forming carbides, or with an inert atmosphere forming nitrides.

By exploiting the volume expansion associated with the formation of such compounds, near net-shape components with almost zero shrinkage can be fabricated [8,9]. Metallic but also oxide fillers can react with the ceramic residue: the pyrolysis of a preceramic polymer in oxidizing atmosphere gives a reactive SiO₂ ceramic residue which can generate complex silicate phases. The latter approach has been extensively applied by the research group in Padova and led to the development of numerous compositions: technical ceramics such as mullite [10] and SiAlON [11] but also bioceramics such as wollastonite [12] and hardystonite [13,14]. The choice of submicro-sized active fillers with high reactivity resulted in phases with high purity, produced at a lower temperature compared to standard ceramic processing technology.

The polymeric nature of the preceramic precursor opens the door to AM development. Polycarbosilane was used both alone and filled with SiC for ink-jet printing of simple shapes[15]; Selective Laser Curing was used to produce downscaled turbine wheels with a polysiloxane powder filled with SiC [16]. More recently, Zocca et al. developed different approaches for the use of powder-bed 3D printing in combination with preceramic polymers: in the first, a solid methylsilsesquioxane powder was used for the powder bed and printed with commercial binders[17]; in the second, the preceramic polymer acted as non sacrificial binder and was jetted on a powder bed containing active (CaCO₃) and passive fillers to form wollastonite-based bioceramic scaffolds [18]. SiOC lattices with ~120 μm thick struts were produced by DIW at the Imperial College London [19]; a small amount of graphene oxide was added to decrease the shrinkage upon pyrolysis. Eckel et al. produced SiOC microlattices and honeycombs with high precision by curing preceramic monomers UV light in a SL printer or with a technology known as self-propagating photopolymer wave-guide technology (SPPW) [20].

Most experiments in this chapter were performed with a specific preceramic polymer, a commercial product labelled Silres MK (Wacker Chemie AG, Nünchritz, DE). It is a poly(methylsilsesquioxane), with the characteristic -Si-(O)_{1.5}- backbone and methyl lateral groups. The glass transition temperature T_g is between 40 and 60 °C, but the polymer also possesses approximately 2 mol% hydroxy and ethoxy groups that allow cross-linking with release of water and ethanol [21]. Cross-linking occurs spontaneously at 150- 200°C, but the reaction can be accelerated by the addition of an appropriate catalyst. However, there is no need of a catalyst when a high amount of fillers is mixed with the polymer, as the fillers will prevent the collapsing of the structure above T_g. The ceramic yield in one of the highest commercially available: 84 wt% upon firing at 1000 °C in air or inert atmosphere.

SL of SiOC from a preceramic polymer

Partially published in:

Zanchetta, E., Cattaldo, M., Franchin, G., Schwentenwein, M., Homa, J., Brusatin, G., Colombo, P.: Stereolithography of SiOC Ceramic Microcomponents. Adv. Mater.

2016, 28, 370-376 [22]

SL of preceramic polymers has the potential to combine resolution and surface smoothness typical of polymer forming with the superior thermo-mechanical and chemical properties of ceramics in the microfabrication field. Different methods have already been used to micropattern PDCs components [23]. In particular, polysilazanes 2D shaping was performed with liquid casting, softlithography [24–27] and photolithography [28]; first attempts with 3D fabrication were conducted with nano-stereolithography [29]. These molecules are not easily available and require processing in a non moisture, oxygen-free environment as they are very sensitive to air. Polysiloxanes, on the other hand, are not sensitive to air and moisture; they are much cheaper and commercially available. Their use has been so far limited to 2D patterns through molding or photolithography (for siloxanes containing vinyl groups) [30–33].

The goal of this section was to fabricate SiOC ceramic microcomponents via SL, starting from a preceramic polymer with high ceramic yield.

Materials and methods

Material Synthesis

Silres MK does not cure under UV light; therefore it needs to be functionalized. The photocurable preceramic polymer was prepared by dissolving MK in a mixture of THF (Aldrich) and Dowanol TPM (Tripropylene Glycol Monomethyl Ether, Dow Chemical Company) solvents in 1:1 volume ratio under stirring and sonication. Typically, 40 g of MK were dissolved in 40 mL of solution. Then, an organically modified silicon alkoxyde (3-(trimethoxysilyl)propyl methacrylate or TMSPM) was added to the solution with a MK to TMSPM weight ratio of 80:20 and let stir for 1 hour. The mixture was finally hydrolyzed in acidic conditions (1% molar of HCl and 2.4% molar of water with respect to TMSPM) at room temperature for 12 h.

2D soft-lithography optimization experiments

The photopolymerization of the acrylic groups in the photocurable resin was promoted by the addition of two commercial photoinitiators: 2-Benzyl-2-dimethylamino-1-(4-morpholinophenyl)butanone-1 (Ciba IRGACURE 369, BASF, Ludwigshafen, DE) and 2,2-dimethoxy-1,2-diphenylethan-1-one (Ciba IRGACURE 651, BASF, Ludwigshafen, DE) with a molar concentration of 1% with respect to TMSPM. Thin films (5 μm thick) were deposited by spin coating on a Si wafer and a micro-patterned PDMS mold was gently pressed on them. The material was exposed to increasing UV doses with a 250 nm-enhanced type Xe–Hg Hamamatsu Lightningcure LC5 UV lamp (6 J/cm^2) to validate and optimized the process.

Production of 3D SiOC microcomponents

Printing of the microcomponents was conducted at Lithoz (Lithoz GmbH, Wien, A) using the stereolithography printer CeraFab 7500 (Lithoz GmbH, Wien, A; see Fig. 1.3).

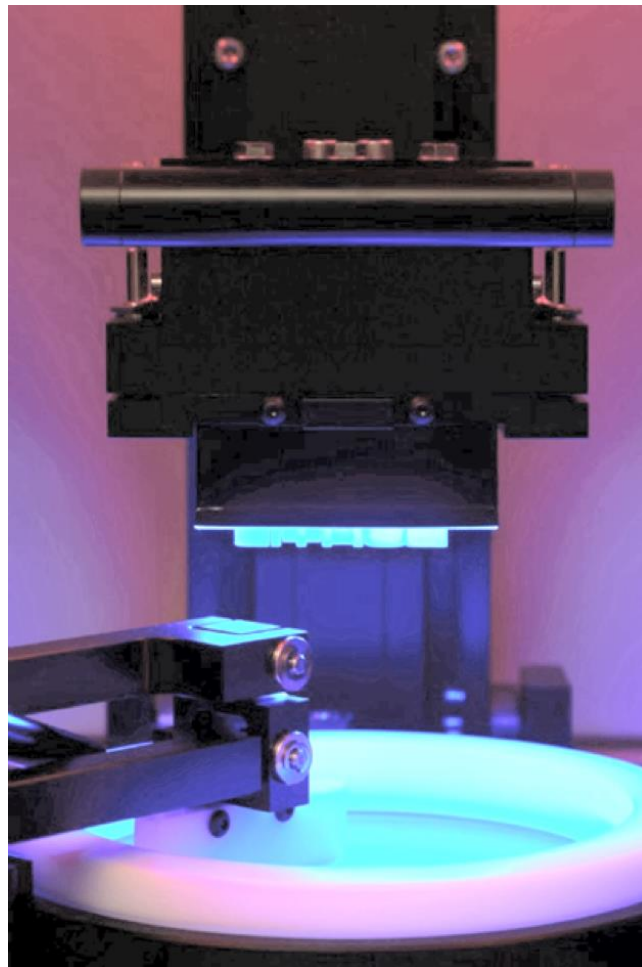


Fig. 1.3 - CeraFab 7500 SL printer (copyright: Lithoz GmbH, Wien, A).

Before printing, the THF solvent was evaporated through rotavapor at 45 °C for 60 min. A different radical-based photoinitiator was chosen, which was a camphorquinone-amine system comprising camphorquinone (Sigma-Aldrich, St. Louis, MI, USA) and ethyl 4-(dimethylamino)benzoate (Sigma-Aldrich, St. Louis, MI, USA) in equimolar ratio. It is already widely used in dental filling materials but also for other biomedical applications [34]. Upon exposure to light in the near UV-range the photoinitiator undergoes homolytic cleavage and forms radicals which then initiate the radical polymerization to form the polymer network. An azo dye was added as light absorber to control the penetration depth of the light into the ink. This way, it is possible to cure thin layers and realize high resolution in z-direction.

The SL process in use is named Lithography-based Ceramic Manufacturing (LCM) and was developed at Lithoz (Lithoz GmbH, Wien, A). It is based on the layer-by-layer selective cross-linking of the resin by means of a LED source according to a virtually sliced CAD model. The local curing allows to shape each layer as desired and prevents thermoplastic flow of the resin during subsequent pyrolysis. After printing of one layer, the moving stage which supports the object moves up and extracts it from the liquid; the vat rotates to recoat the part with the solution. The moving stage moves then down to a gap height corresponding to the layer height. A schematic of the process is shown in Fig. 1.4.

The process can be applied to a wide range of different viscosities, from <1 to 100 Pa·s, with only some adjustments in the printing parameters. The lateral resolution of the system is 40 µm; the layer height was set to 25 µm.

After 3D printing, the base and support struts were removed from the green bodies, which were then pyrolyzed at 1000 °C with a heating rate of 1 °C/min for 1 hour in inert atmosphere (99.99% N₂).

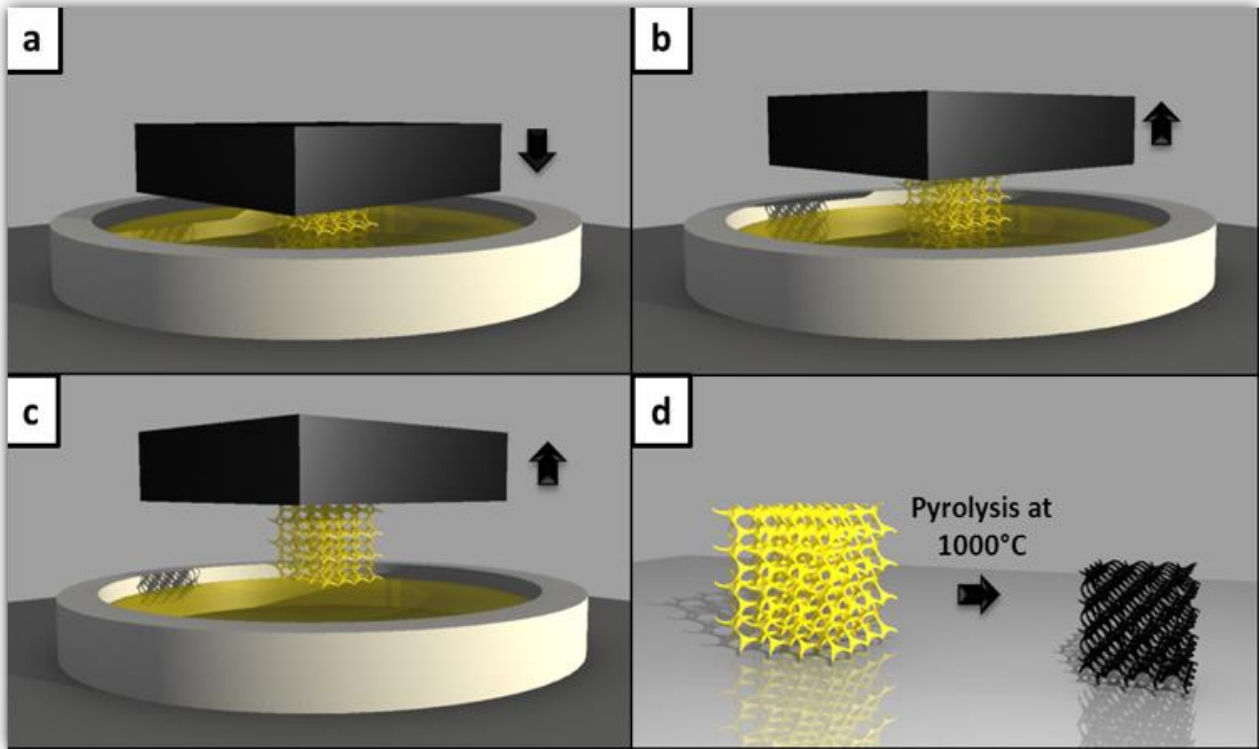


Fig. 1.4 - SL of the preceramic photopolymer. (a) the moving stage goes down to a gap corresponding to the layer height, and a layer is cured; (b) the moving stage goes up to release the component; (c) at the end of the process, the component is removed; (d) pyrolysis at 1000 °C gives the SiOC component (black) [22].

Characterization

The progress of the photopolymerization reaction in the preceramic polymer was investigated by means of Fourier transform infrared spectroscopy (Jasco FT-IR-620 spectrometer) in the range of 400–4500 cm^{-1} with a resolution of $\pm 4 \text{ cm}^{-1}$; it provides bonding information for the ceramic material after pyrolysis.

The ceramization process was investigated by differential thermal analysis/thermal gravimetry (DTA/TG; STA409/429, Netzsch Gerätebau GmbH, Selb, DE), operating in nitrogen flow using a heating rate of 2 °C/min up to the maximum temperature of 1000 °C. The analysis was conducted on the MK+TMSPM mixture previously dried in air at 60 °C overnight to eliminate the THF.

X-ray diffraction (XRD) pattern of the ceramized material was collected using a X-ray diffractometer (D8 Advance, Bruker Italia Srl, Milano, IT) with Cu $K\alpha$ radiation, step scan 0.02°, 2 s per step.

The quality and the microstructure of the green bodies and of the corresponding ceramic structures was evaluated through stereomicroscopy (STEMI 2000-C, Carl Zeiss AG, Oberkochen, DE) and scanning electron microscopy (ESEM, Quanta 200, FEI, Hillsboro, OR).

The designed total porosity was extracted from of the CAD file as the ratio between the volume occupied by the structure and the volume of the rectangular prism encapsulating the object. The true density of SiOC powder after ceramization was measured by means of a helium pycnometer (Micromeritics AccuPyc 1330, Norcross, GA). The total porosity of the lattices was calculated by weighing the samples on a digital scale and measuring their size of the samples using a digital caliper, taking into account the measured SiOC density.

The compression strength of the SiOC structures was assessed on samples of approximately $10 \times 10 \times 10 \text{ Mm}^3$ in size, using an Instron 1121 UTM (Instron Danvers, MA) operating with a cross-head speed of 0.2 mm min^{-1} .

Results and discussion

As printed components could not be produced in house, when those experiments were conducted, first experiments were carried out on polymer films to allow for a quick feedback concerning the different parameters chosen for the ink. First, the MK-TMSPM ratio was adjusted until a sufficient polymerization degree was reached. The assumption was that a composition suitable for obtaining a 2D solid structure after removal of the mold would also allow to obtain solid layers through stereolithography.

Fig. 1.5 reports the proposed mechanism for cross-linking of the photocurable MK-TMSPM system, supported by FTIR spectroscopy of a MK-TMSPM film exposed at increasing UV doses.

As the curing progressed, C-C bond absorbance decreased and C-O peak broadened and shifted to higher wavelengths, signaling the polymerization of TMSPM's acrylate groups and gradual terminal double bond polymerization [35]. Moreover, Si-OH absorption decreased, together with the ratio between the longitudinal and the transverse optical components of the Si-O-Si bond; these variations indicated a densification of the film through the condensation of Si-O-Si bonds[36].

The curing process resulted in a condensed SiOC glassy network linked to a polymerized organic phase.

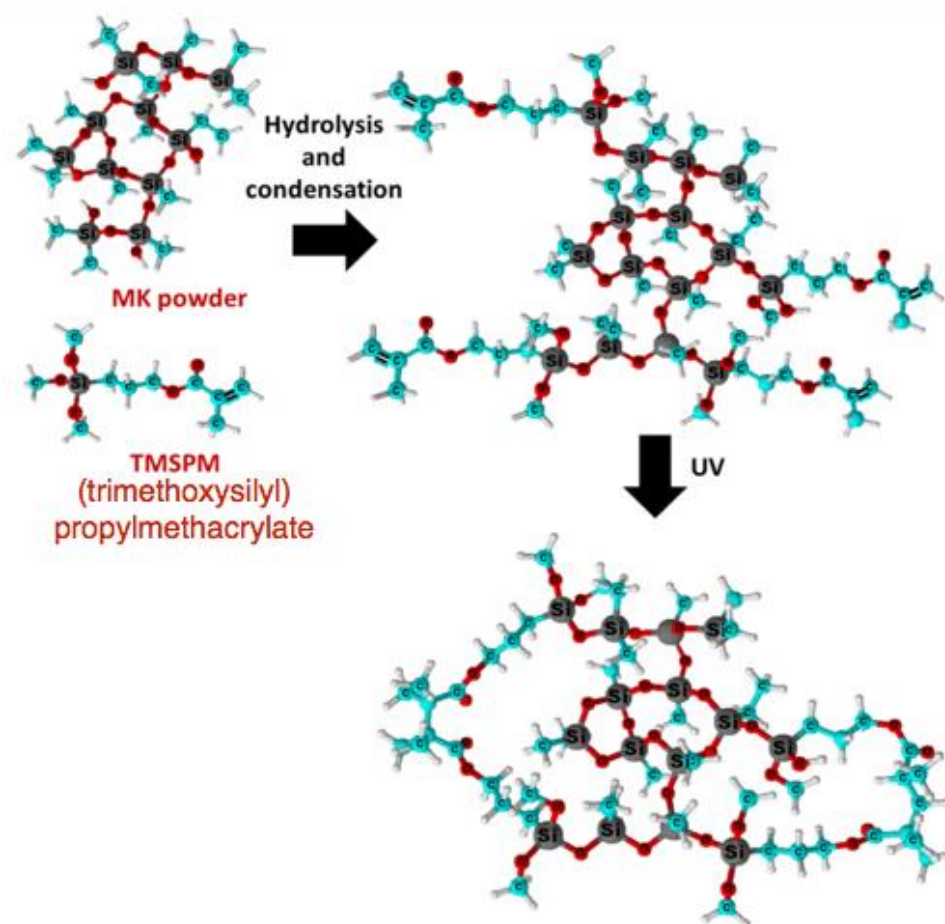


Fig. 1.5 – Photocurable MK-TMSPM synthesis and curing.

Optimization of the pyrolysis conditions was also performed on the 2D structures until shape retention of the produced components during heating was reached (i.e. that the degree of cross-linking and the heating rate were appropriate to avoid melting of the structures). The low heating rate chosen, associated with the previous UV cross-linking of the structures, allowed shape retention and the diffusion and release of decomposition gaseous species without generation of pores and defects. FTIR spectroscopy and XRD diffraction analysis on the ceramized material confirmed that amorphous SiOC phase was obtained.

The ceramization process was investigated by thermal gravimetry. Fig. 1.6 reports the TGA curves in nitrogen atmosphere for the single components of the system, i.e. MK resin, TMSPM, pure THF, pure dowanol their mixture; finally, it includes the TGA curve of the photopolymerized system.

The system was dried overnight at 60 °C in air; data from the solvents and the solvent mixture demonstrated that THF was almost entirely eliminated, whereas some residual dowanol is retained.

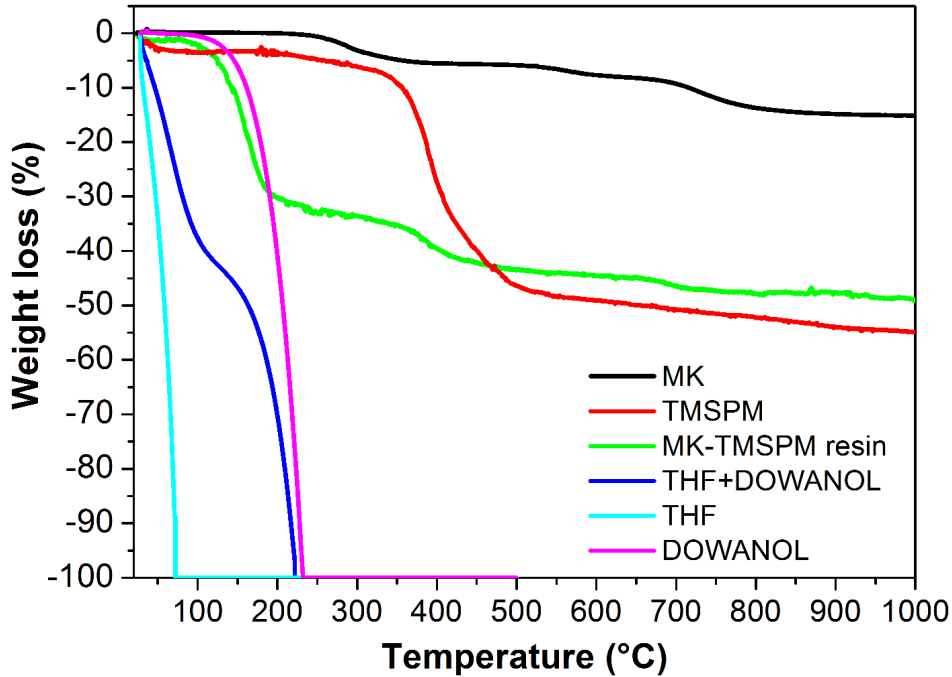


Fig. 1.6 - TGA curves in nitrogen atmosphere for the pure silicone resin (MK), TMSPM powder, MK-TMSPM resin powder, THF+Dowanol solvent mixture, and pure THF and pure Dowanol [22].

The overall mass loss for MK-TMSPM was of 48.6 wt% at 1000°C, and it was the result of four main contributions:

- 1) ~2 wt% loss from room temperature to 100 °C was caused by the evaporation of water produced by the polycondensation reactions and of residual THF;
- 2) ~31 wt% loss from 100 to ~230 °C was due to the evaporation of residual dowanol;
- 3) ~11 wt% loss from 230 to ~500 °C was caused by the polycondensation of MK and subsequent release of byproducts (water and ethanol) as well as to the degradation of the organic component of TMSPM;
- 4) ~4 wt% loss from 500 to ~800 °C corresponded to the loss of hydrogen and methane from MK (transformation of the organic-inorganic polymeric network into a ceramic one).

Though it is hard to separate the contributions from the different components occurring in the same temperature range, data indicated clearly that ~29 wt% of the mass loss could be attributed to the residual solvent, and explained why the overall ceramic yield was significantly lower than the pure MK one (~15 wt% loss at 1000 °C). On the other hand, a solvent with low volatility is required for achieving longer printing times before the viscosity of the material increases too much.

SEM images of the 2D microstructures after pyrolysis are shown in Fig. 1.7. Pillars with a diameter of 4 μm with no shape distortion and defects are visible, indicating that the cross-linking process and subsequent pyrolysis were successful.

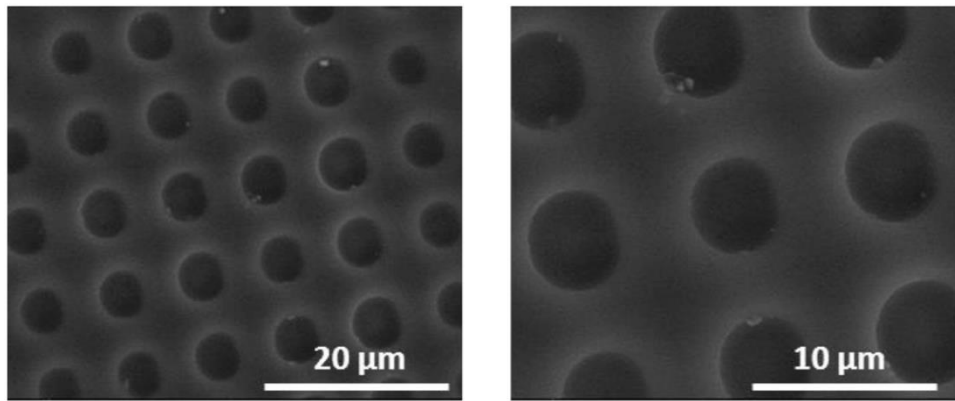


Fig. 1.7 - SEM images of PDC 2D microstructures obtained through soft-lithography after pyrolysis at 1000°C in nitrogen atmosphere[37].

First 3D samples produced with CeraFab 7500 (Lithoz GmbH, Wien, A) were simple cylinders. Fig. 1.8(a) is a picture of the green bodies; Fig. 1.8(b-d) show SEM images of a pyrolyzed cylinder at increasing magnification. The quality of this structures is rather low as the experiments were performed on mixtures with variable amount of solvent and varying printing parameters in order to optimize the process. However, the experiments confirmed that the degree of crosslinking achieved during 3D printing, even with a different photoinitiator, was sufficient to avoid deformation of the component during pyrolysis, and that the pyrolysis led to the formation of dense 3D microstructures.

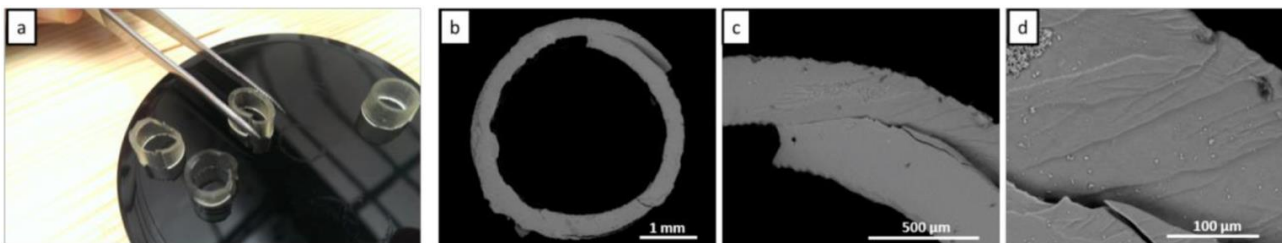


Fig. 1.8 - 3D cylinders by SL: (a) picture of the green bodies and (b-d) SEM images of a pyrolyzed cylinder at increasing magnification [37].

After optimization of the printing parameters, a complex lattice with a resolution of $\sim 200 \mu\text{m}$ was finally fabricated. It possessed cavities, undercuts and large overhangs in order to demonstrate the versatility and accuracy of SL technique. Successful printing of such a delicate and complex structure demonstrated the high photoreactivity of the resin, the sufficient stiffness of the cured photopolymer and the high achievable resolution. Many different shapes and micro-components—either dense or highly porous—could be produced using this approach.

Fig. 1.9 reports a comparison between the green body and the SiOC structure after pyrolysis at 1000 °C in nitrogen atmosphere. The conversion from polymer to ceramic resulted in a ~25% isotropic linear shrinkage, which did not deform the pyrolyzed structure.

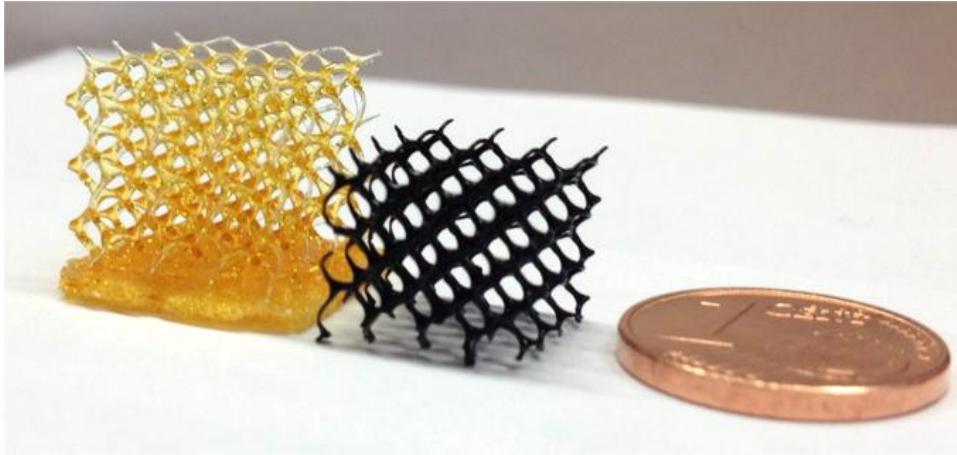


Fig. 1.9 - Picture of a printed green body and of the corresponding pyrolyzed 3D ceramic component.

Fig. 1.10 reports SEM images of the printed and pyrolyzed structure at increasing magnification. The evidence of the layer-by-layer fabrication can be noted in Fig. 1.10(b, e): different bands protruding from the surface can be detected. They are separated by ~25 μm (equal to the set layer height) in the green body and by ~20 μm after pyrolysis, confirming the structure shrinkage.

The surface of both the green and the pyrolyzed lattices was smooth and completely defect-free. The struts of the cellular structure, whose sections are shown in Fig. 1.10(c, f) are dense and show no porosity.

The SiOC struts have a density of 2.12 g/cm^3 . The designed total porosity of the components was 96.03 vol%, while the measured one was 93.1 ± 0.3 vol%. This difference can be caused by some degree of over-polymerization during printing, which slightly decreased the porosity of the actual parts. The compression strength of the ceramized SiOC structures was 0.686 ± 0.105 MPa.

Considering the relative density of the tested components (0.069 ± 0.002), the structures possessed a compression strength in accordance with values reported in the literature for SiOC macroporous ceramics produced using different processes [38].

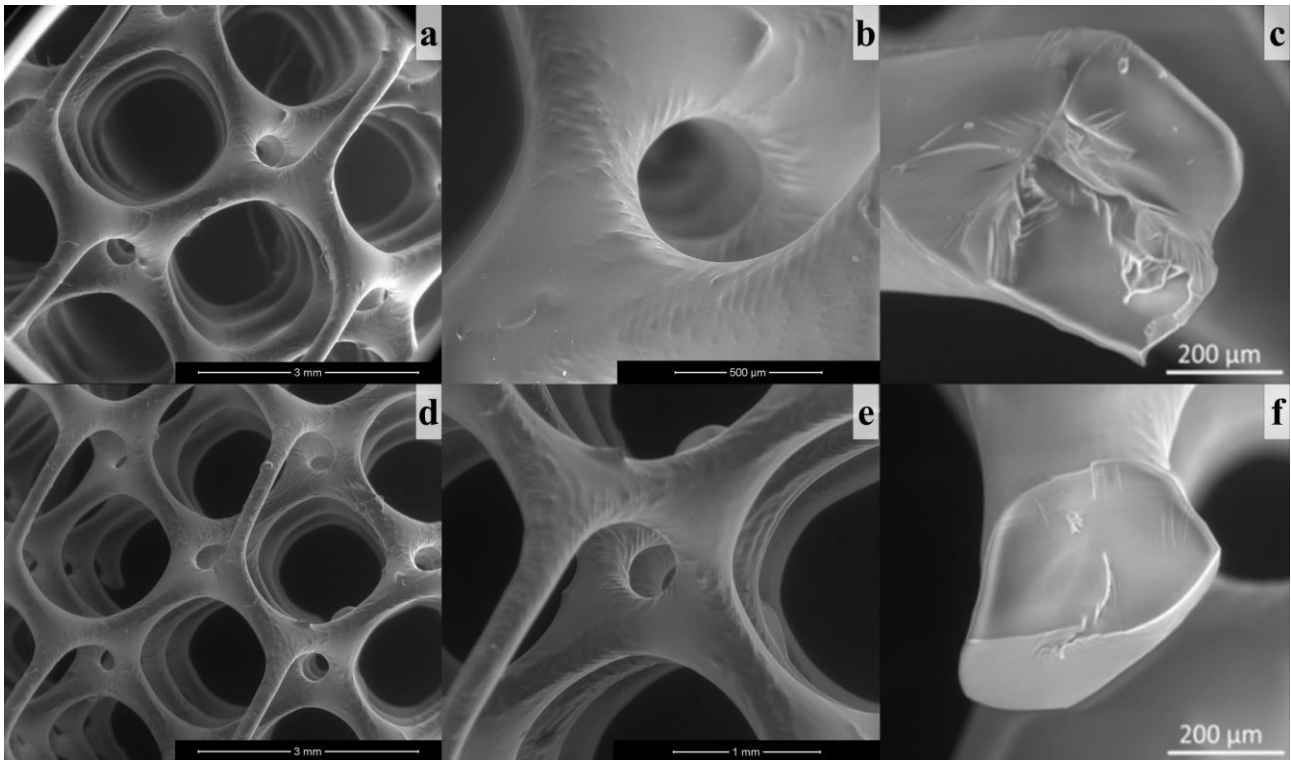


Fig. 1.10 – (a) and (b) SEM images at increasing magnification of the green body and (c) a close up of a section of its struts; (d) and (e) SEM images at increasing magnification of the same component after pyrolysis and (f) close-up of a section of its struts after pyrolysis.

Conclusions

Stereolithography of dense and crack-free SiOC ceramic micro-components with high resolution was demonstrated using a commercially available preceramic polymer which was chemically modified for the purpose. Cellular geometries with strut size down to $\sim 200 \mu\text{m}$ were fabricated and converted to dense, crack-free SiOC micro-components with optimal surface quality through pyrolysis at $1000 \text{ }^\circ\text{C}$. Ceramic objects fabricated with SL possessed a compressive strength similar to that of conventionally produced components.

Single parts with variable 3D model design can be quickly realized without shape limitations (i.e. overhangs, undercuts, cavities), opening the way to complex micrometric 3D structures based on advanced ceramic materials such as SiOC. In fact, the same strategy can be transferred to other PDCs systems (SiC, SiCN, and BN) producing precision micro-components able to resist to harsh environments and high temperatures. As the decomposition products need to be effectively eliminated during pyrolysis, porous structures or small dense parts are the best options in order to avoid residual pores and cracks.

DIW of hardystonite from a preceramic polymer and fillers

Partially published in:

Zocca, A., Franchin, G., Elsayed, H., Gioffredi, E., Bernardo, E., Colombo, P.: Direct Ink Writing of a Preceramic Polymer and Fillers to Produce Hardystonite (Ca₂ZnSi₂O₇) Bioceramic Scaffolds. J. Am. Ceram. Soc. 2016, 99 (6), 1-8 [39]

Hardystonite (Ca₂ZnSi₂O₇) is a zinc calcium silicate; it is gaining interest in the bioceramics field as it possesses better mechanical properties and also improved biological ones compared to calcium silicate wollastonite (CaSiO₃). In fact, hardystonite ceramics can conduct both osteoblast-like cells and osteoclasts, which are the main living constituents of human bones; therefore, they find potential application in skeletal tissue regeneration and as coatings [40]. Bone marrow mesenchymal stromal cells were reported to attach and spread well on the hardystonite ceramics; moreover, a bending strength of 136 ± 4 MPa and a fracture toughness of 1.24 ± 0.03 MPa m^{1/2} were reported for samples with a relative density of $83 \pm 3\%$ and a grain size in the range of 1-5 μm [41].

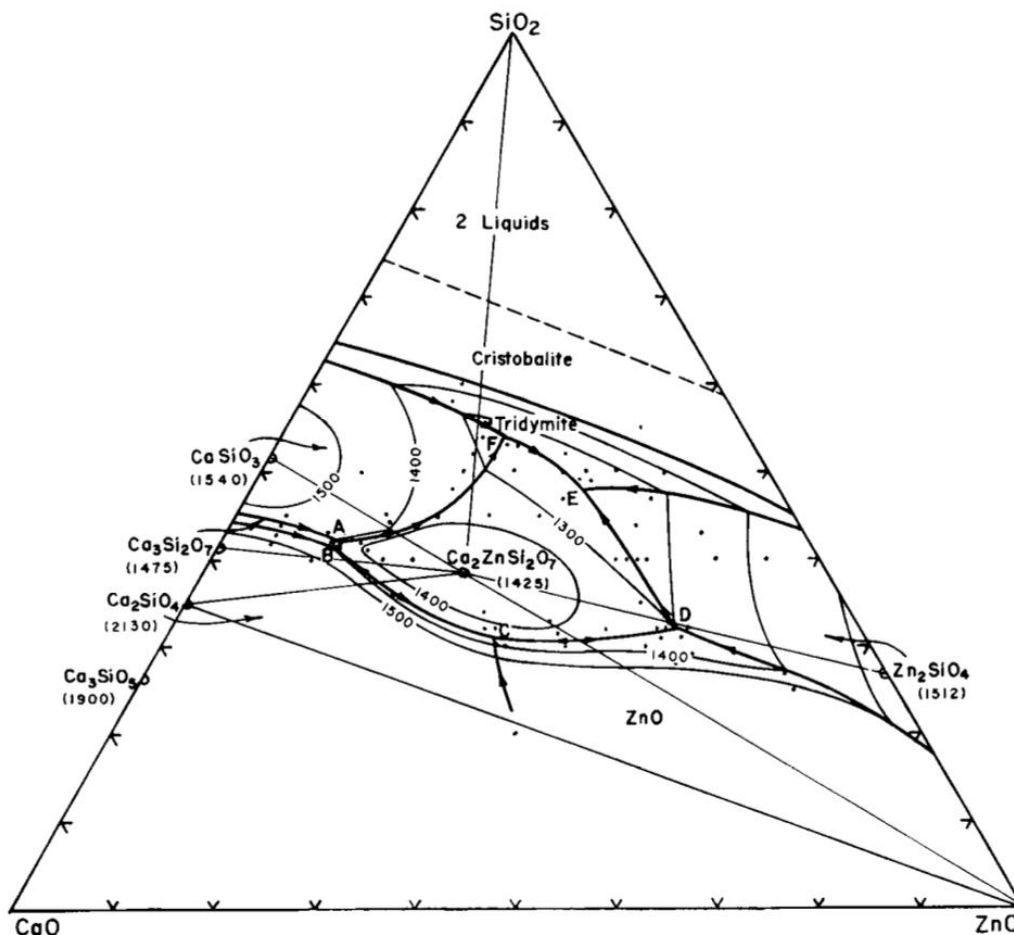


Fig. 1.11 - Phase diagram of the system CaO-SiO₂-ZnO [42].

The synthesis of hardystonite through the reaction of a preceramic polymer and fillers has been recently demonstrated within the research group [14]; the reaction is the following:



Hardystonite phase is also identified in the SiO₂-CaO-ZnO phase diagrams in Fig. 1.11.

The aim of the work in this section was to produce hardystonite scaffolds by DIW of an ink containing a preceramic polymer and active fillers.

Materials and methods

Ink preparation

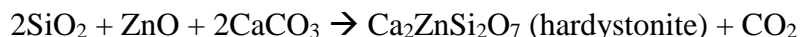
ZnO (Sigma-Aldrich, St. Louis, MO) and CaCO₃ (Bitossi, Vinci, IT) were mixed as a dry powder. Silres MK polymer was used as preceramic polymer, in this case as a SiO₂ source. Fumed silica (FS, Aerosil R106, Evonik, Essen, DE) was mainly used as a rheology modifier, as it is known to be a thickening and thixotropic agent in low molecular weight solvents [43,44]. It also acted as additional source of SiO₂. This FS was treated with octamethylcyclotetrasiloxane to become hydrophobic and dissolvable in isopropanol, which was chosen as a solvent.

The mixing stage of the ink was crucial, as a homogeneous mixture was essential for avoiding the formation of agglomerates capable of clogging the nozzle of the syringe during DIW; moreover, it would help to achieve a complete reaction with no phase separation or inclusions.

The preparation of the ink involved three steps:

- 1) FS was dispersed in isopropanol and mixed with mechanical stirring until a thick gel was achieved;
- 2) Preceramic polymer was gradually added to the dispersion and ball milled in a planetary mill for 1h at 200 rpm in an alumina jar with alumina balls (diameter ~1 cm);
- 3) Finally, the ceramic fillers (ZnO and CaCO₃; hardystonite powder when required) were added, and the ink was again ball milled for 5 hours at 400 rpm.

The first compositions developed, labeled H0, did not contain any hardystonite powder. It was designed to give pure hardystonite upon pyrolysis, according to the reaction:



Upon heat treatment, CaCO₃ decomposes into CaO and gaseous CO₂, and the oxide reacts with the SiO₂ from MK and FS and with ZnO to give the desired silicate.

The second ink developed, named HF, was similar to H0 but contained some hardystonite powder as filler already in the ink.

Biological-grade hardystonite powder was not commercially available, thus the powder was prepared according to the preceramic polymer route followed by ball milling; this was a cheaper and simpler way in comparison to the sol-gel route demonstrated in literature [45].

After some preliminary tests, the appropriate amount of FS to achieve the desired rheology was set at 10 wt%, expressed as amount of fumed silica/total silica, (where total silica = silica derived from the siloxane + fumed silica) after pyrolysis. This value was the same for both H0 and HF. Their final compositions are reported in Table 1.1. The density of the inks was calculated using the rule of mixture from the theoretical density of the individual raw materials.

Table 1.1 - Composition and density of H0 and HF inks (wt%)

Ink	Isopropyl alcohol (g)	Fumed silica (g)	MK (g)	ZnO (g)	CaCO₃ (g)	Hardystonite filler (g)	Density (g/cm³)
H0	13.5	2.5	26.4	16.7	41	0	1.73
HF	12.1	1.9	20.3	12.8	31.6	21.2	1.89

The particle size of the filler powders (reported within brackets) was analyzed by a laser diffraction particle size analyzer (Mastersizer S, Malvern, England) and is reported in Table 1.2.

Table 1.2 - Particle size distribution of the fillers in use.

Filler	d(v, 10%) (µm)	d(v, 50%) (µm)	d(v, 90%) (µm)
ZnO	0.34	0.70	1.48
CaCO₃	0.79	2.32	9.18
Hardystonite	0.61	2.03	2.06

Rheological characterization

The rheology of the ink is the key factor for the DIW process, and is crucial for the fabrication of geometries with unsupported parts; in fact, the material has to bear its own weight with minimal deformation after being printed.

The problem of determining the theoretical conditions for the stability of a spanning strut interested Smay et al.[46] and Schlordt et al.[47]. Based on a static beam bending model, Smay et al. demonstrated that in order to have a minimal deflection (< 5% of the filament diameter) the following relation must be satisfied:[46]

$$G' \geq 0.35 \gamma \left(\frac{L}{D} \right)^4 D \quad (1.1)$$

where G' is the shear storage modulus of the ink, γ is the specific weight of the ink in oil ($\gamma_{ink} - \gamma_{oil} = [\rho_{ink} - \rho_{oil}] \cdot g$; with $g \sim 9.81 \text{ m/s}^2$), L the spanning distance (distance between two points supporting the filament) and D the diameter of the filament.

Schlördt et al. focused on the dynamical deformation of the filament and proposed a model for the midspan deflection [47]:

$$z(t) \sim \frac{1}{2} \sqrt{L(t)^2 - L_0^2} \quad (1.2)$$

where $z(t)$ is the time dependent midspan deflection, L_0 is initial length of the beam and $L(t)$ is the time dependent length of the beam, which can be expressed as:

$$L(t) = L_0 \left(1 + \int_0^t \frac{\rho \cdot g \cdot L_0}{6\eta(t)} dt \right) \quad (1.3)$$

where $\rho = \rho_{ink} - \rho_{oil}$ is the density of the ink in the oil bath, g is the gravitation constant and $\eta(t)$ is the time dependent viscosity. Both models were slightly modified to account for the buoyancy force given by the fact that the filaments were immersed in oil.

$\eta(t)$ plays the most important role, as it is the only time dependent variable; in an optimized Bingham pseudoplastic system, the material is extruded at high shear rate and at low viscosity; once it is deposited, its viscosity should rapidly increase (recover) to minimize the deflection $z(t)$.

In order to assess whether the inks were suitable for a DIW process and to apply the proposed models, three different rheological tests were performed:

- 1) **Steady rate sweep:** the shear rate was ramping from 0.1 s^{-1} to 100 s^{-1} and the corresponding shear stress was measured;
- 2) **Dynamic oscillation test,** the strain ramping logarithmically from 0.01% to 100% at 1 Hz frequency;
- 3) **Viscosity recovery,** in two steps. First, a shear rate of 50 s^{-1} for 30 s was applied, followed by the application of a controlled shear stress of 25 Pa for 90 s in order to measure the recovery of viscosity. The shear rate needed to be high enough to overcome the initial yield stress of the ink; in the second stage, the shear stress needed to be lower than the yield stress to allow recovery. Values were chosen according to the results of the other two tests.

The tests were performed at the Istituto Italiano di Tecnologia (IIT, Torino, IT) with a stress-controlled rheometer (MCR302, Anton Paar GmbH, Austria), equipped with a Peltier system for temperature control and with 50 mm parallel plates geometry. The tests were performed in isothermal conditions at 25°C ; a solvent trap filled with isopropanol was used to prevent quick evaporation of the highly volatile solvent.

DIW and ceramization of hardystonite 3D scaffolds

The device used in this work was commercial fused deposition modelling printer for polymeric materials (Powerwasp Evo, Wasproject, Massa Lombarda, IT) equipped with a syringe for paste extrusion. The syringe containing the preceramic ink was mounted in place of the heated head, and the ink was extruded by a mechanical piston actioned by a stepper motor on the side. The lateral (XY) resolution of the printer is 120 μm ; the Z resolution is 4 μm . The syringe base system can mount conical nozzles of various sizes (Nordson Italia S.p.a., Segrate, IT) ranging from 100 to 1500 μm . The printer and its equipment are shown in Fig. 1.12.

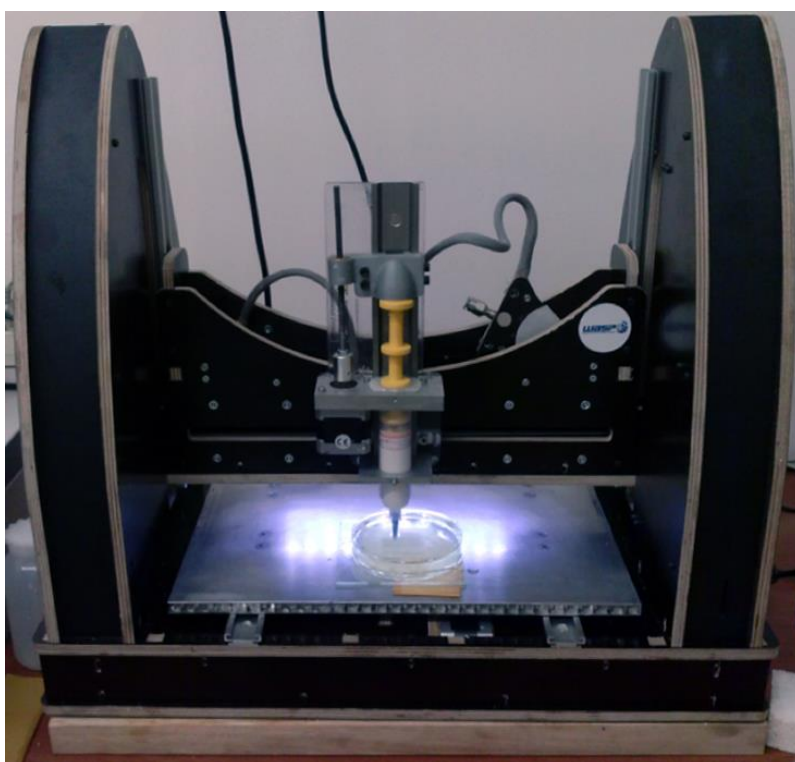


Fig. 1.12 - Powerwasp Evo FDM printer with paste extrusion equipment.

For this work, nozzles with a diameter of 410 μm were used. Because of the fine nozzles, printing in air resulted in frequent clogging of the nozzle; therefore, the ink was printed in a nonwetting oil bath (sunflower oil, $\rho_{\text{oil}} = 0.92 \text{ g/cm}^3$) visible in Fig. 1.12.

The green bodies were heat treated following this schedule: pre-heating at 200°C on a Teflon foil in order to start the cross-linking of the polymer, heating to 450°C at a rate of 1°C/min, from 450 to 500°C at 0.5°C/min (1h dwelling at 500°C), from 500 to 600°C at 0.5°C/min (3h dwelling at 600°C), from 600 to 900°C at 1°C/min, from 900 to 1200°C at 5°C/min (1h dwelling time at 1200°C). The heat treatment was conducted either in static air or under flowing nitrogen (99.99%).

Characterization

The ceramization process was investigated by DTA/TG (STA409/429, Netzsch Gerätebau GmbH, Selb, DE), operating in static air and nitrogen flow using a heating rate of 2 °C min⁻¹ up to the maximum temperature of 1200 °C. The analysis was conducted on the inks and on the raw materials and led the optimization of the heat treatment.

The phase composition of ceramized powders (obtained through grinding of the filaments after heat treatment at 1200°C) was investigated by XRD (D8 Advance, Bruker Italia Srl, Milano, IT).

The composition of the ceramized materials was determined by X-ray fluorescence (Spectro X-LAB; Spectro Analytical Instruments GmbH, Kleve, DE).

The dimensions of the scaffolds were measured by means of a digital caliper, before and after the heat treatment, in order to calculate the shrinkage occurring during ceramization.

The designed total porosity was calculated as the ratio between the volume occupied by the model scaffold and the volume of the rectangular prism encapsulating the object. The true density of ground filaments after ceramization was measured by means of a helium pycnometer (Micromeritics AccuPyc 1330, Norcross, GA). The total porosity of the scaffolds was calculated and given by weighing the samples on a digital scale and measuring their size using a digital caliper, taking into account the measured true density.

The compressive strength of the ceramized scaffolds was measured at room temperature using an Instron 1121 UTM (Instron Danvers, MA) at cross-head speed of 0.5 mm/min. It was calculated from the maximum stress recorded during the test. As it was not possible to lap the samples to achieve parallel faces, a compliant layer (Parafilm M, Pechiney Plastic Packaging, Neenah, WI) was used between the plates and the sample surfaces to ensure that the load distribution was homogeneous. The results were reported as mean ± standard deviation over at least 10 samples for each composition.

The morphology of the scaffolds was investigated by scanning electron microscopy (ESEM, Quanta 200, FEI, Hillsboro, OR). The porosity in the struts of the scaffold was evaluated by image analysis of SEM pictures using Fiji software [48].

Results and discussion

Rheological characterization

To validate the suitability of the inks for DIW, their rheological properties were measured and used to apply the proposed models.

The steady rate sweep test allowed to assess if the inks possessed a Bingham pseudo-plastic behavior, as desired for DIW applications [49].

Modeling the extrusion process as the flow of a viscous fluid through a tube, the shear rate applied to the ink can be estimated by:

$$\gamma' = \frac{4Q}{\pi r^3} \quad (1.4)$$

where Q is the volumetric flow rate, r is the nozzle radius; in the experiments presented here, the estimated shear rate was $\sim 100 \text{ s}^{-1}$.

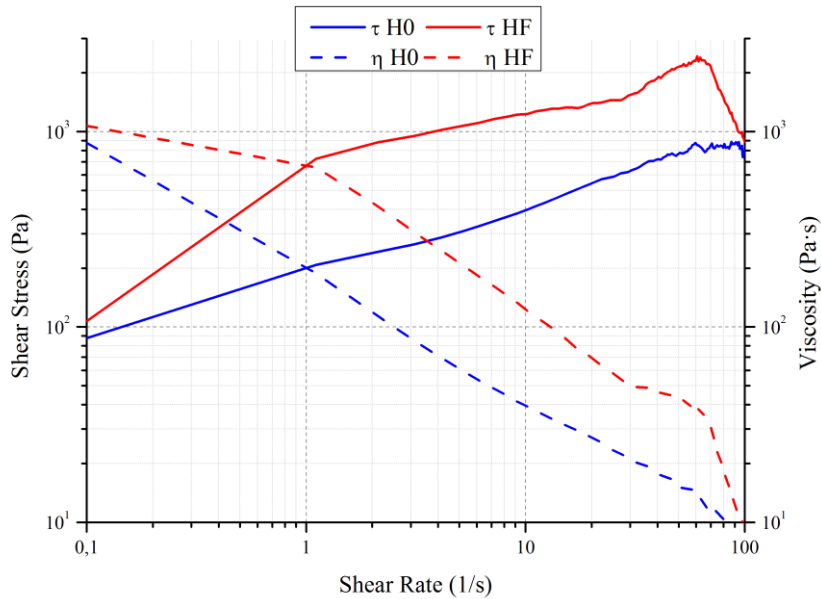


Fig. 1.13 - Flow curves for H0 and HF inks, plotting the shear stress and the calculated apparent viscosity with dependence to the shear rate [39].

Fig. 1.13 shows the experimental flow curves for H0 and HF inks. H0 had a high apparent viscosity at low shear rates: for $\gamma' = 0.1 \text{ s}^{-1}$, the viscosity is $\eta \sim 10^3 \text{ Pa}\cdot\text{s}$; when the shear rate increased to 100 s^{-1} , the viscosity decreased by two orders of magnitude. This behavior is typical of shear thinning fluids, and the linear trend of the curves in double logarithmic scale is in accordance to a power-law model with yield stress reported by Herschel [50]. The curves for HF were similar, also with a viscosity $\eta \sim 10^3 \text{ Pa}\cdot\text{s}$ at low shear rates which goes down to $\eta \sim 10 \text{ Pa}\cdot\text{s}$ in correspondence to the extrusion shear rate. The lines here seem to be fragmented in two linear segments with different slope, but this effect might be caused by experimental errors; in fact, the ink tended to be expelled from the side of the plates of the rheometer as the shear rate increased. This might also be the cause of the humps and irregularities observed at high shear rates.

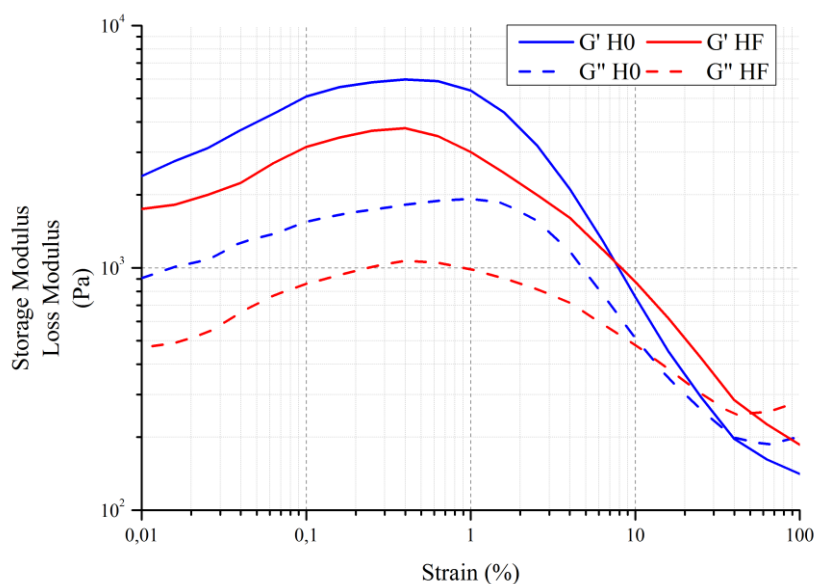


Fig. 1.14 - Log-log plot of the storage and loss moduli of H0 and HF inks as a function of the shear stress. The strain was ramping logarithmically from 0.01 to 100% at 1Hz [39].

Dynamic oscillation tests allowed to assess whether the inks had a transition to low rigidity systems at high shear stress values. Fig. 1.14 shows a log-log plot of the storage (G') and loss (G'') moduli of the inks as a function of the shear stress. The curves show a similar behavior and both can be divided in three different sections:

- 1) at low shear stress, a distinct plateau for G' and G'' was detected;
- 2) at intermediate shear stress both moduli showed an overshoot;
- 3) the two curves for G' and G'' decreased and intersected; then, their values stabilized again.

This trend is typical of a gel and can be interpreted as a gradual destruction of the microstructural arrangement of the ink. It can be classified as type IV Large Amplitude Oscillatory Test (LAOS) behavior, or strong strain overshoots. Such conduct is related to intermolecular interaction and formation of network microstructure [51]. In this case, it was the suspended fumed silica which formed a network of interconnected colloidal aggregates; as they were bonded by weak Van der Waals forces, they could be reversibly disrupted and reformed when a shear stress was respectively applied or removed [43].

In the plateau region, $G'_{(eq)} \sim 6.0$ kPa for H0. As per HF, G' was slightly lower ($G'_{(eq)} \sim 3.8$ kPa), indicating that a weaker gel was formed. Since these curves did not have a clear transition point, the values of the yield stress τ_y were determined at the intersection between the G' and G'' curves and were found to be $\tau_y \sim 96$ Pa for H0 and $\tau_y \sim 255$ Pa for HF.

This method resulted in lower values for τ_y compared to different criteria applied in literature (i.e. that τ_y corresponded to the τ value for which $G' = 0.9 G'_{(eq)}$), thus being more conservative [46].

To assess whether these values satisfied the condition in Eq. 1.1, the threshold values in the equation were calculated for the chosen geometry and ink. The model scaffold possessed unsupported features with a designed spanning distance L (road gap) of 1 mm (corresponding to the actual measured value); the filament diameter D (road width) was 0.35 mm. The two inks had a density $\rho_{ink} = 1.73 \text{ g/cm}^3$ for H0 and $\rho_{ink} = 1.89 \text{ g/cm}^3$ for HF, corresponding to a specific weight of $7.75 \cdot 10^3 \text{ N/m}^3$ and $9.32 \cdot 10^3 \text{ N/m}^3$, respectively. Inputting these values, Eq. 1.1 gives $G' \geq 63 \text{ Pa}$ for H0 and 76 Pa for HF. The values resulting from the dynamic oscillation test were significantly above the limits, indicating that the developed inks had sufficiently high rigidity at low shear stress values.

It is true that in literature typically stronger gels were used for DIW. Smay et al. developed inks with $G'_{(eq)}$ in the range of 10 to 100 kPa [46], while inks used by Schlordt et al. showed a $G'_{(eq)}$ up to 390 kPa [47]. For the generation of larger structures or higher L/D ratio, the development of inks with higher $G'_{(eq)}$ might be necessary; a possible solution could be to increase the content of fumed silica or to reduce the content of solvent.

The time dependent viscosity recovery test was performed in order to assess whether the midspan deflection in the printed structures would have been acceptable. The measurement enabled to follow the degradation of the structure of the material at the micro-scale (gel-like interconnected structure) occurring in the first step, when a stress above τ_y was applied; the recovery of the gel-like structure with time was recorded during the second step.

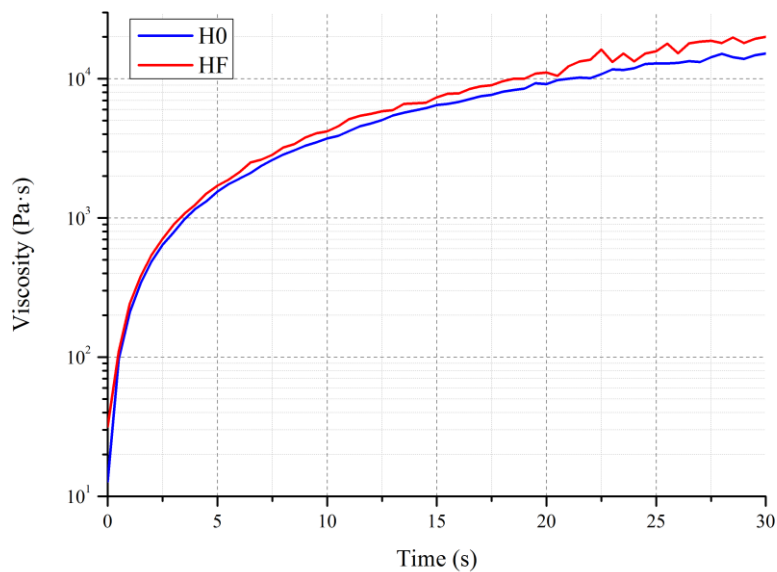


Fig. 1.15 - Viscosity recovery test. The plot shows the second stage of the test [39].

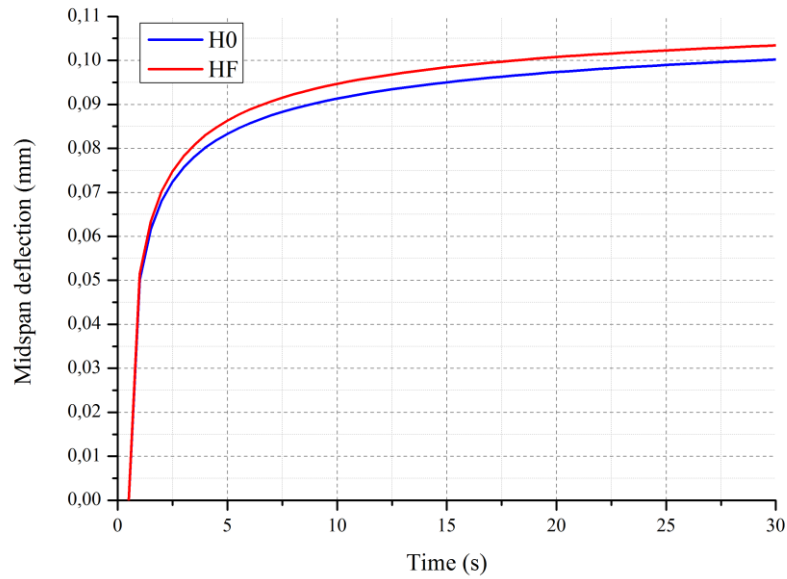


Fig. 1.16 - Midspan deflection calculated with Eq. 1.2 and Eq. 1.3 using data from Fig. 1.15 as input [39].

Fig. 1.15 shows the recovery of viscosity with time during the second stage. H0 and HF behavior was very similar: the viscosity started from a low value (below 100 Pa·s) but increased by two orders of magnitude in less than 20 seconds, arriving at a plateau value. This result confirmed the deformation of the unsupported structures in the printed scaffold was limited to a short period of time, before the viscosity increased and the system became too rigid. These results were in accordance with what achieved experimentally by Lewis et al [52].

Using these data as input in Eq. 1.2 and 1.3, the deflection profile in the middle of the filament could be calculated and is reported in Fig. 1.16. The shape of the curve traced that of Fig. 1.15. For the given spanning distance L and a filament diameter D , the final calculated deflection was ~ 0.1 mm for both H0 and HF, which was considered acceptable. These results confirmed that the inks developed were suitable for DIW of desired geometry with good accuracy. Having developed a stronger alumina ink, Schlördt et al. also reported a smaller deflection of only ~ 0.04 mm with a similar proposed model ($L = 1$ mm, $D = 0.5$ mm) [47]. However, the modeled deflection slightly overestimated the experimental observations: a midspan deflection of ~ 0.07 mm was measured in the scaffolds; similarly, for a span of 2.5 mm, the model estimated a midspan deflection of 0.4 mm, while a deflection of ~ 0.3 mm was observed.

Production and characterization of porous scaffolds

After the rheological optimization, the inks were used for scaffold fabrication via DIW. The chosen geometry was of a $15 \times 5 \times 5 \text{ mm}^3$ scaffold with orthogonal pores, with $350 \mu\text{m}$ thick struts and a spanning length of 1 mm. A model scaffold with these characteristics has a computed porosity of 79.6 vol%; during printing, however, a small overlap ($50 \mu\text{m}$) was introduced between the layers in order to improve the adhesion between the filaments. This resulted in a porosity slightly lower than the value calculated for the model.

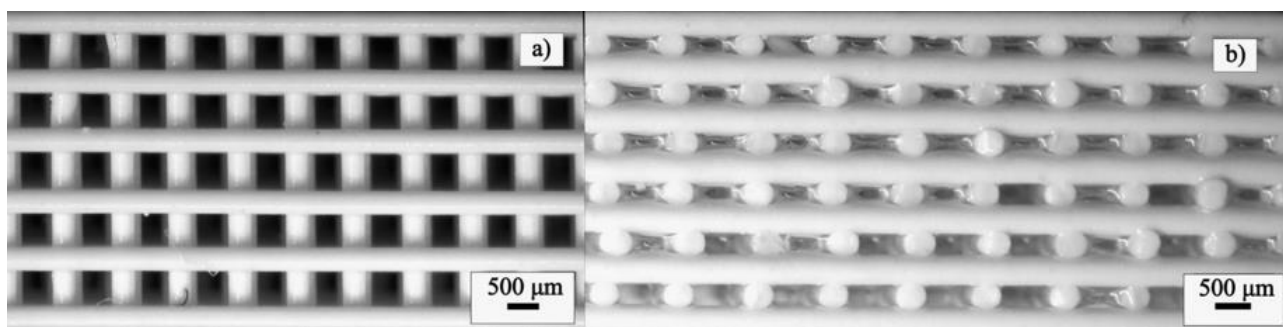


Fig. 1.17 - (a) Top view and (b) side view of a scaffold in the green state, printed with HF ink, from optical microscope images [39].

Fig. 1.17 shows an example of the printed scaffolds in the green state, before the heat treatment. The image is relative to HF, but scaffolds produced with ink H0 were similar. Very limited sagging can be detected, confirming the results from the rheological characterization. The as printed structures showed no visible cracks or defects and possessed an optimal adhesion between the layers.

First pyrolysis treatments were performed in air to 1200°C with a heating rate of $1^{\circ}\text{C}/\text{min}$ on scaffolds printed with ink H0. The heat treatment resulted in extensive cracking of the filaments (visible in Fig. 1.18).

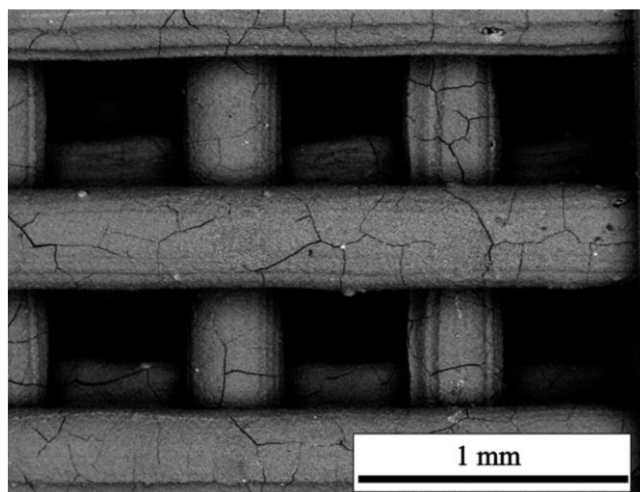


Fig. 1.18 - SEM of a scaffold printed with ink H0 after pyrolysis at 1200 °C in air [39].

DTA/TG analysis was performed on the inks and the raw materials in order to understand the possible causes of the cracking; resulting curves are reported in Fig. 1.19(a).

Considering the pure MK polymer, a first mass loss starting from $\sim 230^{\circ}\text{C}$ could be detected; it corresponded to the release of byproducts (water and ethanol) from the cross-linking reactions. From $\sim 350^{\circ}\text{C}$ to $\sim 830^{\circ}\text{C}$ an almost continuous mass loss took place as the polymer transformed to ceramic releasing decomposition products.

The CaCO_3 powder, on the other hand, started to decompose at $\sim 700^{\circ}\text{C}$ forming CaO and CO_2 ; most of the mass loss associated with the reaction (~ 45 wt%) is concentrated between 800°C and 950°C . As the CaCO_3 contribution to the mass loss was the highest, this was supposed to be the major cause for the extensive cracking of the scaffolds. CaO powder could be used instead of CaCO_3 as a filler, but its processing is problematic due to its high hygroscopicity.

A different approach to solve the issue brought to the development of ink HF. In fact, the already ceramized hardystonite powder acted as inert filler and decreased the total amount of gaseous species released. The amount of hardystonite filler was selected after some preliminary trials, considering both the rheology of the ink and the quality of the scaffolds after printing and heat treatment; the final composition is reported in Table 1.1. TGA analysis confirmed this hypothesis, as the total mass loss of HF was slightly lower than that of ink H0.

Besides the MK polymer and CaCO_3 mass losses, both inks showed an initial mass loss which can be attributed to the evaporation of residual solvent.

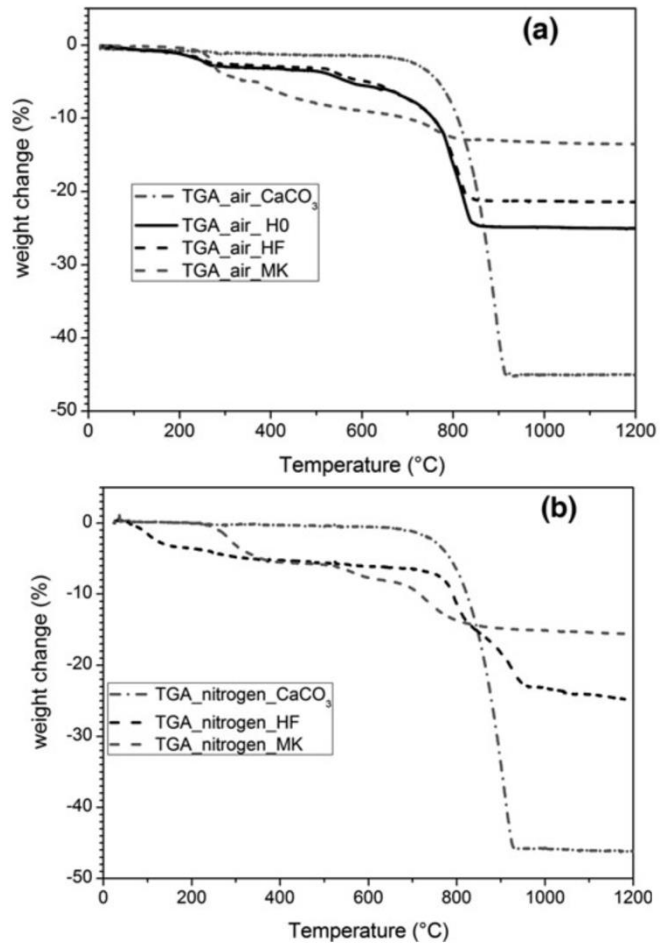


Fig. 1.19 - TGA curves up to 1200 °C of H0, HF, MK and CaCO₃ (a) in air and (b) in nitrogen [39].

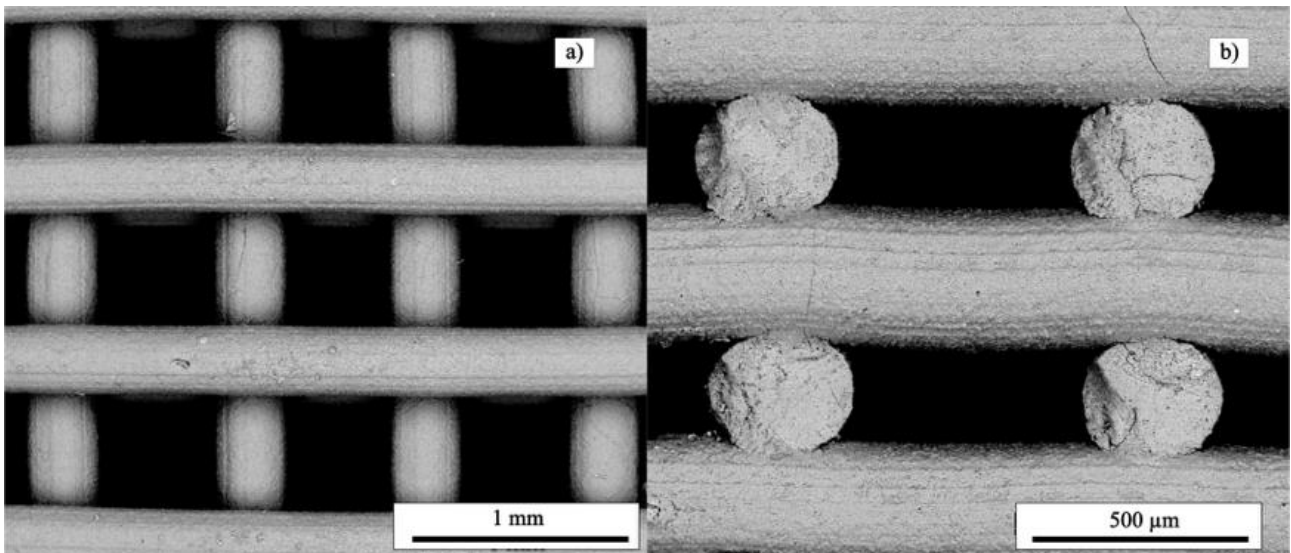


Fig. 1.20 - (a) Top view and (b) side view from SEM microscope images of a scaffold printed with HF ink, after pyrolysis in air at 1200 °C [39].

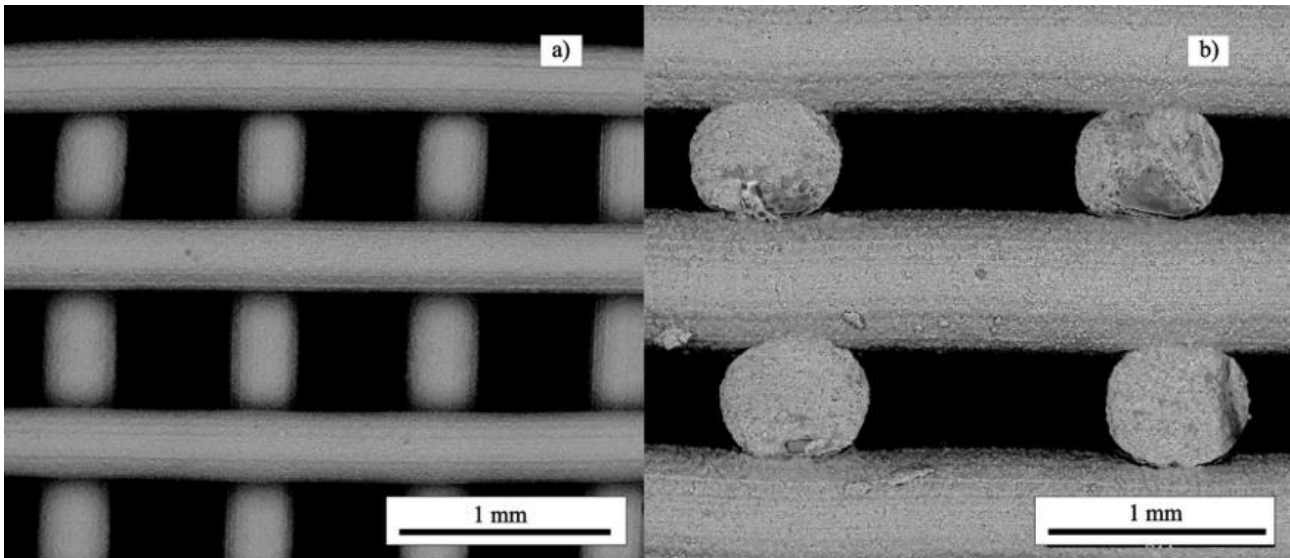


Fig. 1.21 - (a) Top view and (b) side view from SEM microscope images of a scaffold printed with HF ink, after pyrolysis in nitrogen at 1200 °C.

The addition of the inert filler was successful as it greatly decreased the cracking the filaments (see Fig. 1.20). There are just few cracks still barely visible, which might be related to the pyrolysis but also to the handling and cutting of the samples before the analysis.

The pyrolysis of scaffolds produced with HF ink was also performed in flowing nitrogen. The inert atmosphere resulted in a SiOC residue upon ceramization, instead of the SiO₂ residue which is obtained when heating in air [17]. The resulting scaffolds were analyzed by means of SEM micrographs (see Fig. 1.21); these scaffolds did not show any crack or defect. The results suggest that the oxidation of the Si-CH₃ groups in the silicone preceramic polymer above 350°C [53], which is a very exothermic reaction [54,55], was at least partially responsible for the formation of the cracks.

Fig. 1.22 shows the cross-section of a scaffold printed with HF and pyrolyzed in air (a) and in nitrogen (b); the struts were micro-porous, with an average pore size of ~1 μm and a max pore size below 10 μm. The porosity was likely generated during CO₂ release, and was estimated to be ~17 vol% for both samples. Although it is true that the porosity would lower the mechanical strength of the scaffolds, it would be beneficial for bioceramic applications, as it would facilitate osteoblasts attachment and spread and improve the osteoconductivity of the material [56,57].

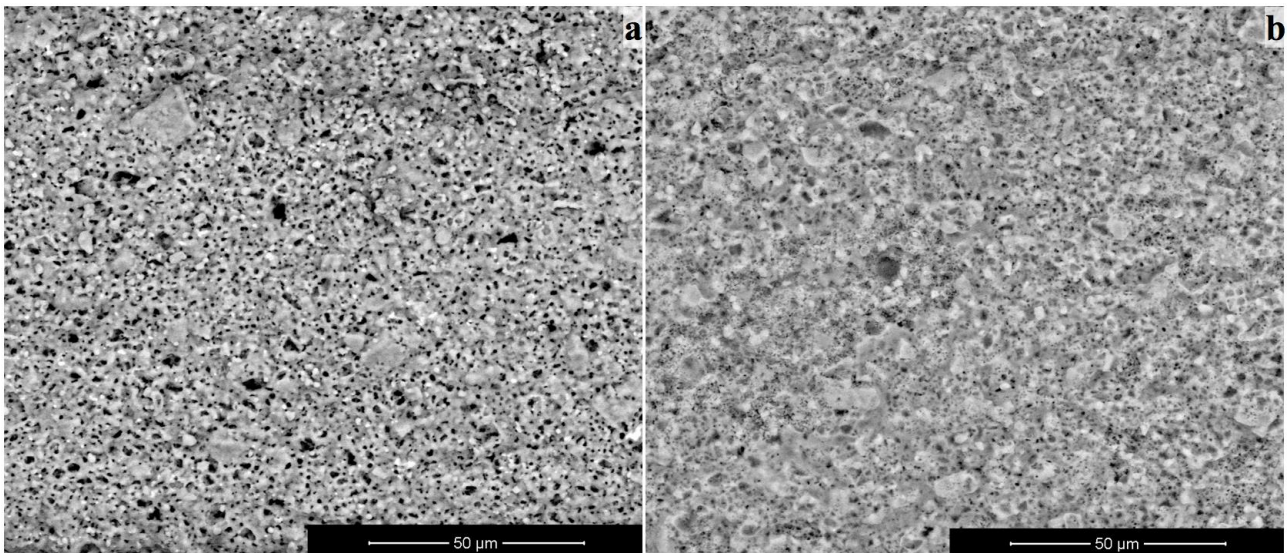


Fig. 1.22 - Microstructural details of a scaffold printed with HF, (a) pyrolyzed in air and (b) in nitrogen, from SEM images [39].

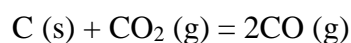
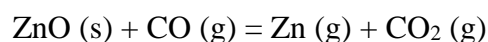
Crystalline phase assemblage

The crystalline phases developed by HF ink after pyrolysis at 1200°C for 1 h in air and in nitrogen were investigated (Fig. 1.23).

After heat treatment in air, HF yielded virtually pure hardystonite ($\text{Ca}_2\text{ZnSi}_2\text{O}_7$); no secondary phases and no traces of unreacted ZnO or other raw materials were detected.

HF treated in nitrogen, however, did not develop hardystonite as the main crystalline phase. The main phases that formed were two polymorphs of wollastonite (CaSiO_3), para- and pseudo-wollastonite, along with only small traces of hardystonite. No other Zn containing phases or significant residual glassy phase were present, which suggested that most part of the Zn left the sample during the heat treatment. The same results were obtained using argon instead of nitrogen, a sign that the latter did not have a direct role in the loss of Zn.

The carbonaceous residuals from the ceramization of the preceramic polymer do not decompose in inert atmosphere; the ZnO most likely underwent a carbothermal reaction with them and reduced to metallic Zn. According to the Ellingham diagram relative to Zn, this reaction is estimated to happen ~950 °C [58]. At the pyrolysis temperature employed (1200°C), therefore, ZnO carbothermal reduction to metallic Zn could proceed via the solid-gas intermediate reactions [59]:



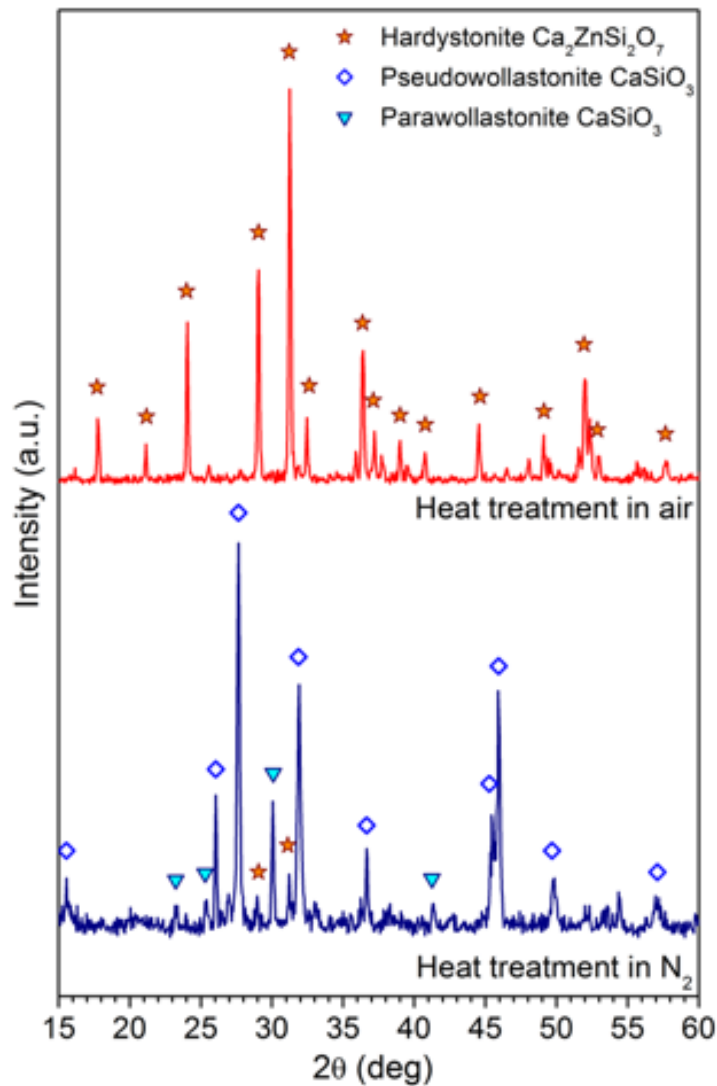


Fig. 1.23 - Diffraction patterns of HF ink pyrolyzed at 1200 °C in air (top) and nitrogen (bottom) [39].

If a carbothermal reaction is not occurring, then an oxygen partial pressure lower than 10^{-12} atm is necessary to reduce ZnO to metallic Zn at 1200 °C according to the same diagram for the reaction $2\text{ZnO} = 2\text{Zn} + \text{O}_2$. This value is not achievable by the setup in use with flowing nitrogen, and therefore the oxygen partial pressure by itself cannot explain the reduction of ZnO.

The reduced metallic Zn most probably evaporated at high temperature as its boiling point is 907°C; the presence of Zn traces deposited on the walls of the furnace ceramic tube confirmed this hypothesis. As the composition was deprived of Zn, wollastonite (CaSiO_3) was formed instead of hardystonite ($\text{Ca}_2\text{ZnSi}_2\text{O}_7$); in fact, both phases have the same Ca:Si molar ratio.

XRF analysis was employed to confirm the absence of Zn in the samples treated in nitrogen; the results were reported in

Table 1.3 and indicated clearly that after treatment in nitrogen Zn almost completely disappeared.

The theoretical molar ratio SiO_2/CaO is 1, whereas the measured ones were 1.04 in air and 1.08 in nitrogen. Impurities in the raw materials might explain the slight deviations observed. In particular, the natural calcium carbonate in use contained traces of magnesium, sodium and silicon; the Al_2O_3 contamination likely derived from the ball milling process.

Even if HF in nitrogen did not form hardystonite as the main ceramic phase, this result showed the potential of using a heat treatment in inert atmosphere. One might argue that the difference in the cracking behavior in air and nitrogen might be associated with a different volume shrinkage for the two phases developed. The theoretical volume change associated with hardystonite formation is -10.2 vol%, while for wollastonite is -9.2 vol%; while the shrinkage is relevant and might induce stresses in the scaffolds, these values are too similar to justify alone the differences observed.

Table 1.3 - Composition of samples H0 heat treated in air and in nitrogen, measured by XRF

Oxide (wt%)	Heated in air	Heated in nitrogen
SiO₂	37.2	52.5
CaO	33.5	45.2
ZnO	22.9	0.2
Al₂O₃	2.9	-
Na₂O	2.3	1.2
MgO	0.6	0.9

Physical and mechanical properties of the scaffolds

The physical and mechanical properties of scaffolds produced with H0 and HF inks are reported in Table 1.4. Compared to H0 samples, the compressive strength of HF samples improved by almost three times in the case of pyrolysis in air, and up to five times in the case of nitrogen. This result was expectable considering the almost complete elimination of cracks in the HF samples. The relative density of the HF 3D printed structures pyrolyzed in nitrogen was 0.23 ± 0.002 ; this considered, their compression strength was well in accordance with values reported in literature for macro-porous ceramics produced with other processing techniques. Compared to powder-based technologies, scaffolds produced by DIW generally possess better mechanical properties (compressive strength is up to one order of magnitude higher), as their struts are usually denser [38].

There is no reference in literature of hardystonite foams of similar porosity for a comparison. Samples produced by the polymer sponge replication technique had a compression strength of 0.06 ± 0.01 MPa at 90% total porosity [60]; foams based on a different system (hardystonite/gahnite) had a compression strength of 4.1 ± 0.3 MPa at 85 vol% of porosity [61].

Table 1.4 - Shrinkage, total porosity and compressive strength of H0 and HF scaffolds heat treated in air and in nitrogen

	Shrinkage X (%)	Shrinkage Y (%)	Shrinkage Z (%)	Total porosity (vol%)	Compressive strength (MPa)
H0 in air 1200°C	13 ± 3	13 ± 3	n.d.	77 ± 2	0.6 ± 0.2
HF in air 1200°C	9.0 ± 1.0	8.5 ± 0.5	9.9 ± 1.5	74 ± 3	1.6 ± 0.3
HF in N₂ 1200°C	8.1 ± 0.5	9.1 ± 1.0	10.0 ± 1.0	76 ± 4	2.5 ± 0.6

Conclusions

Bioceramic hardystonite scaffolds were produced by DIW of inks composed of a preceramic polymer and active and inert fillers. The preceramic polymer, together with the addition of fumed silica, had the double role of source of silica and rheology modifier. The preceramic polymer acted as a polymeric binder and increased the viscosity of the ink, while the fumed silica additive induced a “gel-like” behavior by forming a network of silica colloidal agglomerates. The rheology of the inks was investigated and compared with two models proposed in the literature. The experimental results confirmed that the inks were suitable to accurately produce scaffolds with a rod diameter of 350 μm and a spanning distance of 1 mm. Pyrolysis in air led to the desired hardystonite phase, while a heat treatment in nitrogen produced wollastonite polymorphs, most likely due to a carbothermal reduction of the ZnO and subsequent evaporation of metallic zinc. The presence of cracks in the ceramized scaffolds was almost completely eliminated by the addition of a hardystonite inert filler to the ink composition, and the produced scaffolds had mechanical properties adequate for non load-bearing bioengineering applications.

DIW of Ceramic Matrix Composites (CMCs) from a preceramic polymer and fibers

Ceramic matrix composites (CMCs) consist in a ceramic matrix embedding ceramic fibers. Several oxide or non-oxide ceramic materials are used for the matrix and the fibers, which can be weaved in many configurations. Their most valuable applications are in components with highly demanding thermal and mechanical requirements.

Polymers are generally weak and limited to low temperatures. Metals can be used up to 1000 °C – 1200 °C (special alloys), but they possess a low creep resistance and are susceptible to oxidation. Monolithic ceramics can be used operational temperatures up to 2000 °C, have an excellent creep resistance and high stiffness; on the other hand, their low fracture toughness leads to brittle fracture and poor thermal shock resistance. The goal of CMC development is the maintenance of the thermal and mechanical properties of monolithic ceramics in combination with a damage tolerant, quasi-ductile fracture behavior. Compared to metals, CMCs are a significantly lighter, can operate at much higher temperatures and possess good resistance to wear and to aggressive chemicals.

Labeling and classification of CMCs comprises fiber and matrix materials, separated by a slash (/). For example, the term C_f/SiC indicates a CMC made of carbon fibers and a silicon carbide matrix. Usually, oxide fibers are combined with oxide matrices and non-oxide fibers with non-oxide matrices. Oxide fibers are usually made of alumina, mullite or silica, whereas the matrices consist of alumina, zirconia, mullite or other alumino-silicates. Non-oxide fiber materials include carbon and silicon carbide, and the same materials (SiC, C) or mixtures of silicon carbide and silicon (SiSiC) are employed as non-oxide matrices. Residual porosity, usually between 1 and 30 %, is also present in most CMCs [62].

What provides the high fracture toughness of CMCs is the interaction between fibers and matrix during fracture, which must be designed carefully according to two complementary concepts [63,64]:

- **Weak interface:** during fracture, the fibers are pulled out of the matrix and the crack propagation along the interface absorbs fracture energy. The fibers can be coated to reduce adhesion to the matrix.
- **Weak matrix:** if the stiffness of the matrix is lower than that of the fibers, cracks will arise in the matrix and will be deflected at the fibers' interface; the fracture surface and the elongation at break will both increase.

CMCs applications exploit their high thermal shock and creep resistance in high temperature processes as materials for flame tubes, heat exchangers, protective tiles, and various high temperature holders. Thanks to the high wear resistance and the favorable friction properties, they find use as sliding contact bearings, brakes and clutch-plates. Their application in extreme environments like gas turbines allows to increase the operating temperatures and improve energy efficiency, and to design blades with very high rotational speeds. As there are not isotropic, their properties can be tailored in different directions; for example, C_f/SiC composites are used to design components with zero thermal expansion in one or two directions applied as support in precision optics, e.g. in satellite communication or microelectronics, or for calibration of dimensional control tools.

Fibers are cut from the yarns to form short fiber bundles or (in case of continuous fibers) weaved, knitted or braided into textile structures. Non-woven structures like uniaxial or multiaxial fabrics, fleeces and felts can be used; they can also be produced directly from short fibers providing cheaper reinforce materials. The 1D, 2D or 3D fiber structure of the preforms controls the anisotropic properties of the final CMC and can be designed to bear the anisotropic loads expected in each direction. The fibers usually receive a coating applied via a CVD process or wet chemical routes.

The matrix material is generally provided via a fluid phase – either gaseous or liquid.

Metallic silicon melts at 1414 °C and is used to infiltrate the preforms; it is absorbed by capillary forces and, in case of carbon particles present in the matrix, it reacts with them to form silicon carbide. C fibers need to be protected to avoid degradation by the liquid Si metal. This process is called liquid silicon infiltration (LSI).

Slurries with ceramic particles can be infiltrated into the preforms at room temperature (ceramic slurry infiltration, CSI) and the impregnation allows for a quasi ductile manufacturing of complex shapes. After drying, however, sintering is required to consolidate the ceramic matrix. As excessive shrinkage of the matrix would cause cracking of the CMC structure, usually the sintering is just partial and the final component retains an open porosity between 20 and 50 %.

The matrix can also be introduced via a reactive gas, with a process known as chemical vapor infiltration (CVI). It requires a controlled atmosphere of the reactive gases at temperatures above 800 °C and several hours (up to some days) to achieve sufficient densities.

Pre-ceramic polymers (pure or with fillers) are a well-known alternative for the manufacturing of CMCs. The advantages over LSI and CVI include simpler and cheaper equipment, lower process temperatures, shorter cycle times and the capability to produce large and complex parts.

They are infiltrated into the preform in dissolved or molten state; the application of external pressure can support this phase.

During the subsequent heat treatment, the polymers are pyrolyzed and the final ceramic structure is formed. The process is known as polymer infiltration and pyrolysis (or Liquid Polymer Infiltration – LPI).

As the polymer undergoes a volumetric shrinkage during pyrolysis, the whole process has to be repeated, typically 3 to 10 times, to achieve sufficient density of the final CMC; an increase in the ceramic yield of preceramic polymers has led to a lower number of infiltration cycles and to lower pyrolysis temperatures (~850 °C). Components can be machined to near-net shape before full densification and no extensive final machining is needed. On the other hand, shapes that can be produced by infiltration are rather conventional and do not allow the fabrication of lattices with internal complexity and voids.

Some research has been conducted in the field of AM of polymer matrix composites [65–71], but none on the development of CMCs via AM routes. The goal of this section was to overcome part of the limitations faced in terms of mechanical properties in the previous experiments with AM of preceramic polymers, and to develop an ink suitable for DIW which would produce a CMC upon pyrolysis. DIW is still an unexplored approach for the production of highly porous CMCs. This project is still ongoing; therefore, the characterization of the printed structures is not yet complete. It is presented as a proof of concept for the feasibility of this approach.

Materials and methods

Ink preparation

The ink development took advantage of the optimization performed in the previous section for the production of hardystonite scaffolds. The same polymer, Silres MK, was used in this case as a SiOC source. Isopropanol was chosen as a solvent. As the amount of fillers was in any case not sufficient to avoid shape loss during the first stages of the pyrolysis treatment, a commercial catalyst (Geniosil GF91, Wacker Chemie AG, Nünchritz, DE) was added to the mixture with a 0.5 wt% ratio on the MK polymer.

Chopped, uncoated carbon fibers (MF100, Ferrari Carbon Srl, Milano, IT) were used as reinforce material. They were 100 µm long and 7.5 µm thick, and possess superior mechanical properties (tensile strength = 3.5 GPa, Young modulus = 230 GPa).

Given its efficacy, hydrophobic fumed silica (FS, Aerosil R106, Evonik, Essen, Germany) was employed as rheology modifier, when needed, and also provided additional SiO₂. SiC powder (E-ABRASIC F 1000, ESK-SIC GmbH, Frechen, DE; d (v, 6%) = 1 µm, d (v, 50%) = 4.5 µm, d (v, 97%) = 10 µm) was added as inert filler in a successive stage of the experiments.

A dispersant (BYK 430, BYK-Chemie GmbH, Wesel, DE) was employed to assure a good dispersion of the SiC powder in the ink.

The mixing stage of the ink was crucial, as a homogeneous mixture was essential for avoiding the formation of fiber agglomerates capable of clogging the nozzle of the syringe during DIW.

The preparation of the inks involved several steps:

- 1) MK was gradually added to isopropanol and dissolved via mechanical stirring for ~2 hours until a viscous, transparent fluid was achieved; the mixture was kept in a closed beaker to avoid solvent evaporation; the polymer to solvent weight ratio was set at 70:30.
- 2) The SiC powder was gradually added to the mixture together with the dispersant, and the mixture was left overnight under mechanical stirring at low speed (< 200 rpm, to avoid air entrapment and foaming).
- 3) The carbon fibers were gradually added to the mixture and dispersed via mechanical at low speed. Based on previous experiences, ball milling would have led to better dispersed, more homogeneous inks; however, in this case it could damage the fibers and therefore mechanical stirring was preferred.
- 4) Fumed silica was added to the ink under mechanical stirring at low speed until a thick gel was achieved.
- 5) Once the ink was ready, GF91 was added under mechanical stirring to catalyze the cross-linking of the polymer; this needed to be the last step, otherwise the ink would start cross-linking before being extruded in the DIW process.

The first composition developed, labeled CF/MK, did not contain any SiC powder. It was designed to give a pure SiOC matrix upon pyrolysis of the preceramic polymer in nitrogen [72]; the expected volume fraction of carbon fibers in the final CMC was ~0.20.

The second ink developed, named CF/(MK+SiC+FS), was similar to CF/MK but contained some SiC powder as filler. The amount of SiC was set at a weight ratio 1:1 with the SiOC provided by the pyrolysis of Silres MK polymer. Given the presence of the filler, the amount of carbon fibers needed to be decreased for rheological constraints: the expected volume fraction in the CMC decreased to ~0.17.

As the polymeric character of the ink was hindered by the filler, addition of fumed silica was needed in order to achieve a rheological behavior suitable for DIW. Fumed silica was added gradually at the end of the mixing process; its amount was set at ~5 wt% of the total ink.

The final compositions of the inks are reported in

Table 1.5. Typical quantities are shown which were able to be printed without waste before the material became too viscous due to cross-linking.

Table 1.5 – Compositions of CF/MK and CF/(MK+SiC+FS) inks.

Ink	Isopropyl alcohol (g)	MK (g)	SiC (g)	Carbon fibers (g)	Fumed silica (g)	GF91 (mL)	BYK430 (mL)
CF/MK	11.70	27.3	0	4.91	0	0.13	0
CF/(MK+SiC+FS)	11.70	27.3	23.2	6.96	3.48	0.13	1.50

Direct ink writing and ceramization of C/SiOC structures

The device used in this work was commercial fused deposition modelling printer for polymeric materials (Delta Wasp 2040 Turbo, Wasproject, Massa Lombarda, IT) equipped with a paste extrusion system. It comprises a pressurized vessel which is filled with the material; the pressure (applied with compressed air or argon) pushes the material through a Teflon tube into a smaller chamber (~20 mL) at the print head, in which an infinite screw extrudes the ink from the nozzle tip mounted below. The system can mount the same kind of conical nozzles (Nordson Italia S.p.a., Segrate, IT; various sizes ranging from 100 to 1500 μm) as the one employed in the previous section.

The new system, employing a combination of a compressed air piston and screw extrusion, is much more effective; the pressure applied is more uniform and can reach higher values, allowing to extrude inks with higher viscosities. Moreover, the screw provides additional mixing of the ink while extruding it, decreasing the risk of phase separation and breaking eventual big agglomerates.

The layer resolution of the printer is 50 μm . The printer and its equipment are shown in Fig. 1.24.

For this work, nozzles with a diameter of 840 and 410 μm were used. The inks developed could be printed in a time frame of 2 to 3 before the cross-linking occurred.

The green bodies were left overnight to cross-link and dry; then, they were heat treated at a rate of 1°C/min to 1000 °C (1h dwelling time). The heat treatment was conducted under flowing nitrogen (99.99%).



Fig. 1.24 – Delta Wasp 2040 Turbo equipped with paste extrusion system.

Characterization

The ceramization process was investigated by DTA/TG (STA409/429, Netzsch Gerätebau GmbH, Selb, DE),, operating in static air and nitrogen flow using a heating rate of $2\text{ }^{\circ}\text{C min}^{-1}$ up to the maximum temperature of $1200\text{ }^{\circ}\text{C}$. The analysis was conducted for previous works and led to the optimization of the heat treatment.

The phase composition of ceramized powders (obtained through grinding of the filaments after heat treatment at $1000\text{ }^{\circ}\text{C}$) was investigated by XRD (D8 Advance, Bruker Italia Srl, Milano, IT).

The dimensions of the scaffolds were measured by means of a digital caliper. The designed total porosity was calculated as the ratio between the volume occupied by the model scaffold and the volume of the rectangular prism encapsulating the object. The true density of ground filaments after ceramization was measured by means of a helium pycnometer (Micromeritics AccuPyc 1330, Norcross, GA). The total porosity of the scaffolds was calculated by weighing the samples on a digital scale and measuring their size using a digital caliper, taking into account the measured true density.

The compressive strength of the ceramized scaffolds was measured at room temperature using an Instron 1121 UTM (Instron Danvers, MA) at cross-head speed of 0.5 mm/min. It was calculated from the maximum stress recorded during the test. As it was not possible to polish the samples to achieve parallel faces, a compliant layer (Parafilm M, Pechiney Plastic Packaging, Neenah, WI) was used between the plates and the sample surfaces to ensure that the load distribution was homogeneous. The results were reported as mean \pm standard deviation over 25 samples.

The morphology of the scaffolds was investigated through stereomicroscopy (STEMI 2000-C, Carl Zeiss AG, Oberkochen, DE) and scanning electron microscopy (ESEM, Quanta 200, FEI, Hillsboro, OR).

Results and discussion

While developing the inks, preliminary tests were performed in order to assess the maximum amount of fibers with which the ink can be extruded through the desired tip. This quantity is limited by the fact that the addition of fibers also increases the viscosity of the ink. Moreover, when the fiber length is close to the diameter of the nozzle tip, agglomerates can form which would clog the tip and block the extrusion process. The maximum volume fraction that allowed extrusion through a sub-mm nozzle tip was \sim 33 vol% of fibers in the final pyrolyzed composite (with a tip of 840 μ m). As the diameter of the nozzle tip was decreased to 410 μ m, the amount of fibers had to decrease accordingly; CF/SiOC final composition was designed with \sim 20 vol% fibers on the final pyrolyzed CMC and was printed without clogging issues. The ink was used for DIW of composite lattices with orthogonal pores. The chosen geometry was of a 19.6 x 19.6 x 4.8 mm³ lattice, with 400 μ m thick struts and a spanning length of 1.6 mm. During printing, a small overlap (50 μ m) was introduced between the layers in order to improve the adhesion between the filaments.

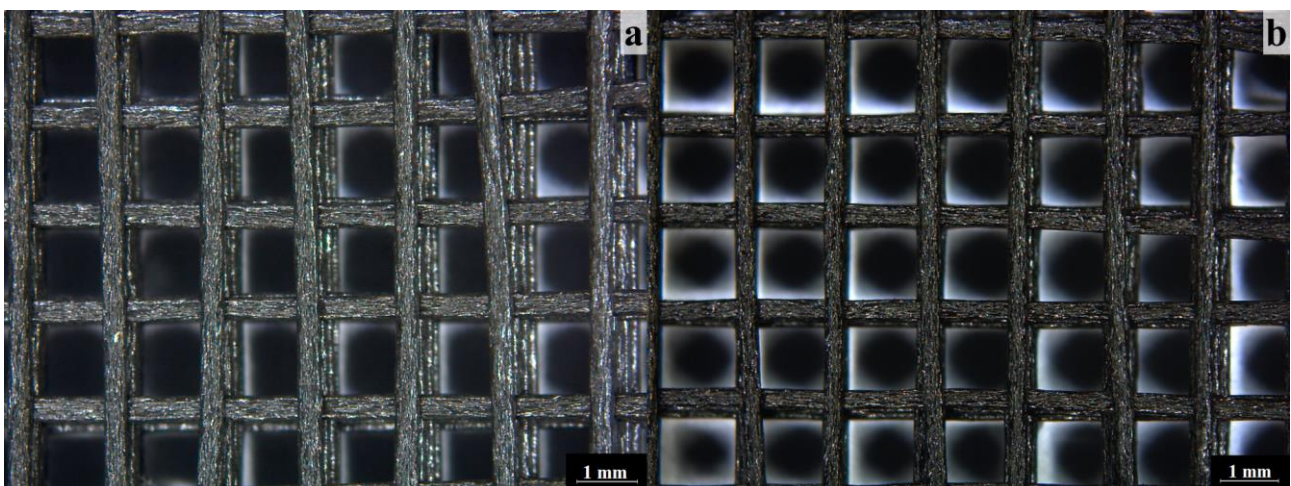


Fig. 1.25 - Stereomicroscope images of lattices printed with CF/SiOC ink: (a) greenbody; (b) pyrolyzed sample.

Fig. 1.25(a, b) shows an example of the printed structures before and after the heat treatment at 1000 °C in nitrogen. The treatment led to formation of amorphous SiOC with a ceramic yield of ~85 wt% (from DTA/TGA analysis; see Fig. 1.19(b) for reference). Both the polymeric and the amorphous SiOC matrix reflected the light from the microscope, thus it is very difficult to make observations on the fiber distribution or on the eventual presence of cracks and defects.

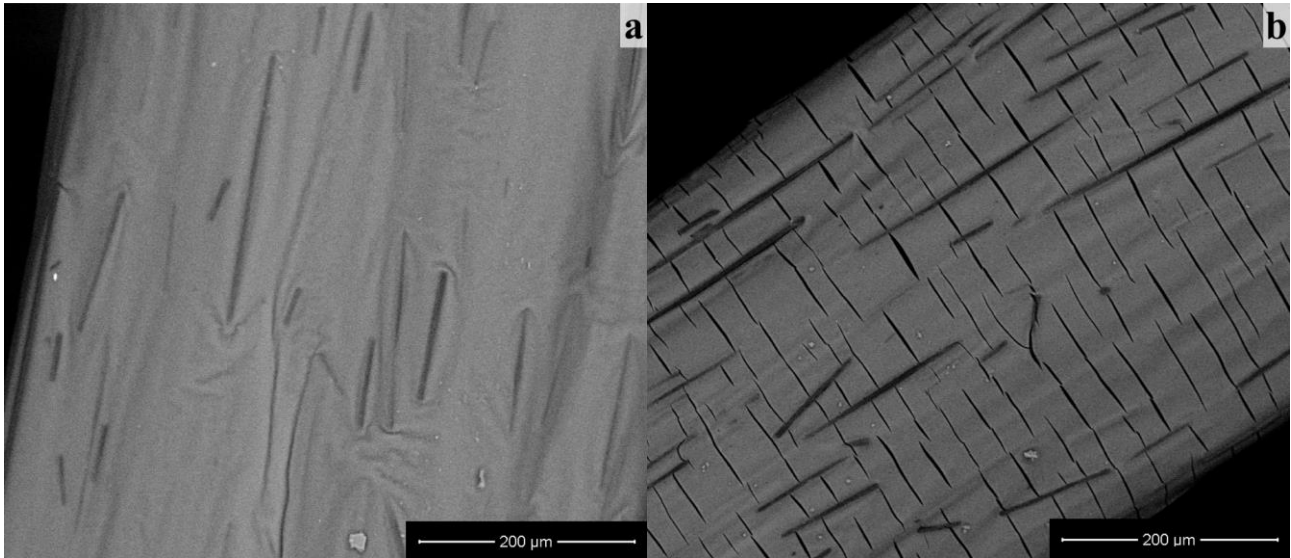


Fig. 1.26 - SEM images of a strut printed with CF/SiOC ink: (a) green body; (b) pyrolyzed sample.

Fig. 1.26(a) is a SEM close-up on a strut printed with CF/SiOC ink before the heat treatment. The filament had no cracks or defects but some wrinkles on the surface in correspondence to the carbon fibers; they were probably associated with the drying and cross-linking stages of the polymer surrounding the fibers. It is interesting to note that the fibers were not oriented randomly, but they tended to align with the extrusion direction; this behavior has already been observed in polymer matrix composites fabricated by FDM or DIW and is due to the shear forces occurring at the nozzle tip during extrusion [66,73]. This observation was of great interest as it can potentially lead to the fabrication of anisotropic structures in which the fibers are aligned to provide higher toughness and resistance in specific sections of the printed component [70].

The effects of heat treatment were clearly visible in Fig. 1.26(b): the filament was extensively cracked, and the cracks propagated perpendicularly to the print direction from the interface between the matrix and the fibers. It is likely that the presence of the carbon fibers hindered the shrinkage of the printed structures; in fact, almost no shrinkage was noticed after the pyrolysis treatment.

The now-ceramic material, unable to absorb the deformation energy, released the stresses through formation of cracks starting at the interface between the matrix and the fibers, where the constraint is maximum.

In the direction perpendicular to the fibers, the matrix was able to shrink, therefore the struts diameter decreased. This finding also suggests that the adhesion between the fibers and the matrix was high, thereby limiting the possibility of independent decoupled shrinkage along the filament axis of the siloxane matrix with respect to the non-shrinking fibers.

A possible solution to this problem would be to lower the amount of fibers used as reinforcement, but it would go against the purpose of the work, as their contribute would not be as significant anymore.

Another option could be the addition of low melting temperature fillers able to provide viscous flow during the ceramization and synthesis of SiOC: this way, the material would be able to deform releases the stresses associated with the shrinkage. This second approach was investigated through the addition of different glass fillers, such as borax and borosilicate glass; results are not shown as the fillers provided no obvious improvements. Cracks disappeared in some cases, but just from the surface; they were still present and went deep into the struts. Moreover, the powders were difficult to disperse homogeneously and resulted in frequent clogging of the nozzle during DIW.

A different approach took inspiration from the previous work with hardystonite powder as inert filler; CF/SiOC ink could also benefit from the mechanism of decreasing the total amount of reactive material undergoing ceramization and therefore shrinkage.

The choice fell on SiC powder because of its chemical affinity with the SiOC matrix, its good thermo-mechanical properties and its wide use in CMCs fabrication; the amount of SiC filler was selected after some preliminary trials, considering both the rheology of the ink and the quality of the lattices after printing and heat treatment; finally, a weight ratio of 50:50 of SiC over the SiOC resulting from MK pyrolysis was chosen.

Although the rheological characterization of the ink has not been performed yet, its behavior was clearly affected by the SiC addition; the polymeric features of the MK solution were not as predominant anymore, therefore a small amount of fumed silica was added as pseudoplasticizing agent with a concentration of ~5 wt% on the total ink. The volume fraction of the fiber reinforcement was also decreased slightly (~17 vol% of fibers on the final pyrolyzed composite), to adapt to the changes in the matrix and lead to an extrudable ink. The final composition of CF/(SiOC+SiC+FS) ink is reported in

Table 1.5.

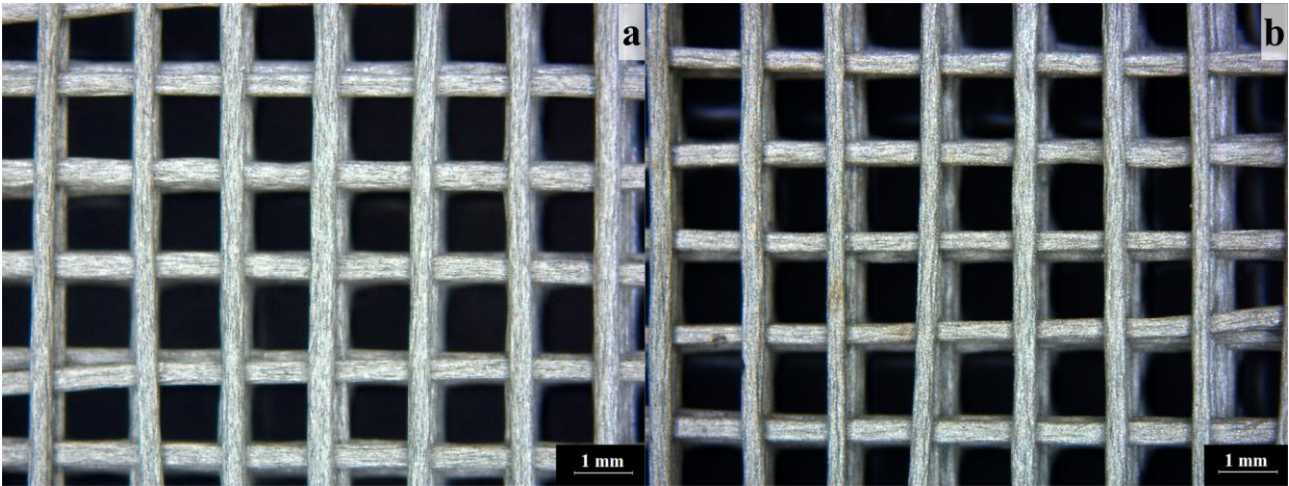


Fig. 1.27 - Stereomicroscope images of structures printed using CF/(SiOC+SiC+FS) ink: (a) green body and (b) pyrolyzed sample.

Fig. 1.27 (a, b) shows an example of the structures printed with the new ink before and after the heat treatment at 1000 °C in nitrogen. Their appearance is different with respect to the previous samples (see Figure 1.24) due to the presence of the powder; also in this case, the shrinkage of the structures along the filament axes was negligible.

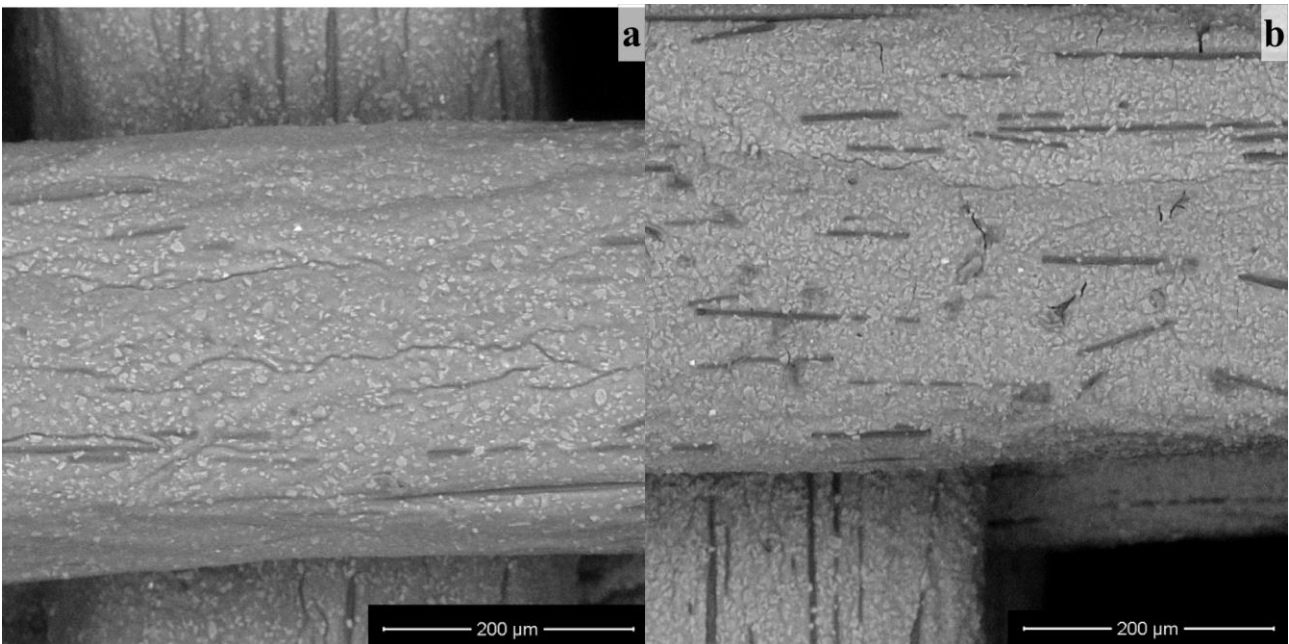


Fig. 1.28- SEM images of a strut printed with CF/(SiOC+SiC+FS) ink: (a) green body and (b) pyrolyzed sample.

Fig. 1.28 shows the surface of a filament printed with CF/(SiOC+SiC+FS) investigated by SEM before and after pyrolysis.

The addition of the inert filler was visible in the green body (Fig. 1.28(a)): the SiC powder was homogeneously dispersed in the filament. Some small cracks and wrinkles developed upon drying, a stage which seemed to affect the structure more than before.

Fig. 1.28(b) validates the addition of inert filler as a solution for the hindered shrinkage: cracks were greatly decreased in number and extension. The few cracks still present seemed less deep and did not show a preferential orientation, and some of them might be still those developed upon drying or might have been caused by handling and cutting of the samples for the analysis.

In fact, each printed component was cut in four parts to provide access to the filament cross-section and to prepare samples for mechanical testing (see Fig. 1.29).

Cutting of the samples was performed in the green state, when the material is less fragile. Each resulting sample should be composed by six struts per each layer, giving a model lattice of $8.4 \times 8.4 \times 4.8 \text{ mm}^3$ for the green sample with a computed total porosity of 77.6 vol%. The average length of the samples measured after heat treatment was $8.24 \pm 0.12 \text{ mm}$, just slightly smaller than the model (as the shrinkage is very little). The height of the samples, on the other hand, was $2.13 \pm 0.12 \text{ mm}$ on average, less than half the designed height. The small overlap between the layer would lead to 4.2 mm, still very different from the observed values.

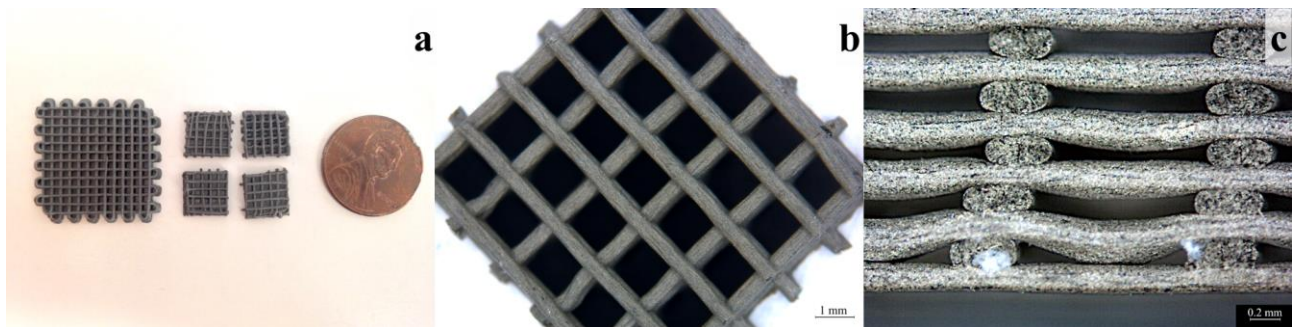


Fig. 1.29 - Samples for mechanical testing: (a) cutting of the CMC lattices; (b) close-up on a cut sample; (c) side microscope view of the sample, showing some deflection but also open porosity.

Fig. 1.29(c) shows the side view of one such sample: it was clear from the picture that filaments did not retain their circular section, but got deformed under the weight of the upper layers developing an elliptical section. The horizontal axis of the ellipses was slightly larger than the filament diameter ($\sim 500 \mu\text{m}$ at the bottom layers) and the vertical one decreased down to $\sim 200 \mu\text{m}$, resulting in a rather flat sample. The rheology of the ink has not been investigated extensively yet, but these results indicate that a stronger gel-like behavior was needed.

Nonetheless, the deflection of the filaments was already limited and the components showed open porosity also in Z direction, indicating that there was some viscosity recovery and that the ink already had some gel-like features.

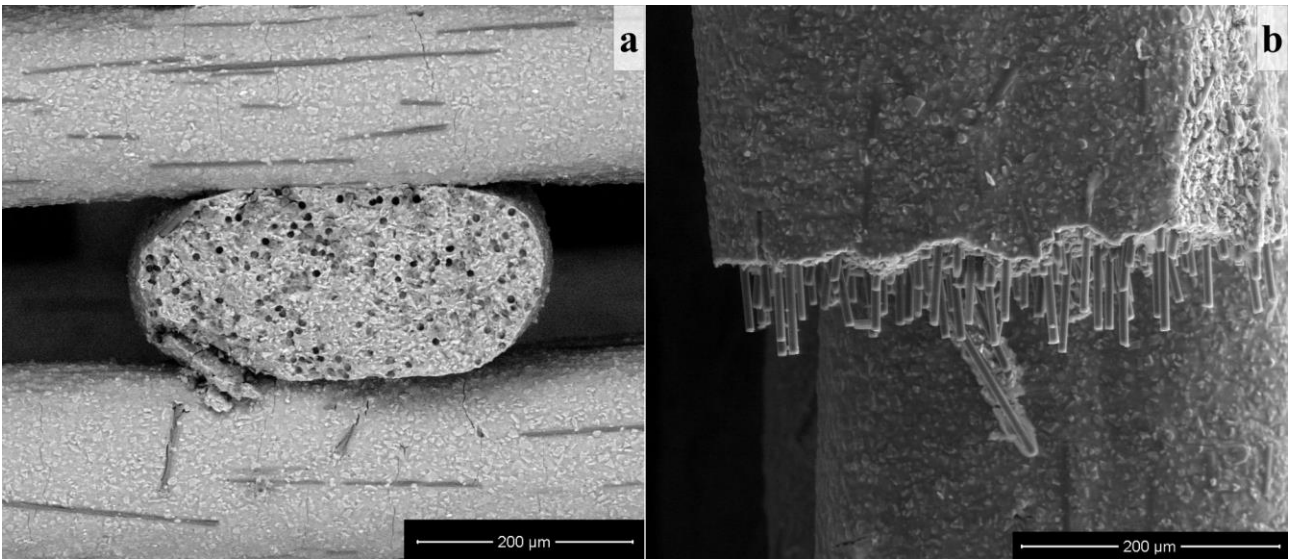


Fig. 1.30 - (a) front view and (b) top view of the sections of ceramized struts printed with CF/(SiOC+SiC+FS) ink via SEM.

Sections of the ceramized struts are reported in Fig. 1.30. Although no specific test was yet conducted, some pull-out of the fibers could be detected, suggesting that the inks developed an appropriate weak interface between the fibers and the matrix, which is crucial for achieving high fracture toughness.

The front view of the strut confirmed the alignment of the fibers in the extrusion direction; the matrix appeared dense (the holes are left by the pull-out of the fibers upon cutting). The fibers also appear to be homogeneously distributed within the section of the strut.

The true density of the struts, measured by means of a helium pycnometer, was 2.41 g/cm^3 ; the measured total porosity of the cut, pyrolyzed samples was $75 \pm 2 \text{ vol}\%$. As the sample height was so different than the designed one, a comparison with the designed total porosity was not meaningful; however, the high value achieved was in accordance with the smaller dimensions of the struts. The feed rate of the DIW process will need to be tailored to approach the volume flow rate of the material being extruded to generate filament with the desired section.

The compressive strength of the ceramized lattices obtained by DIW with CF/(SiOC+SiC+FS) ink was $3.80 \pm 1.23 \text{ MPa}$. Fig. 1.31 reports an example of stress-strain curve of a sample loaded under compression; the behavior was typical of a ceramic cellular architecture [74].

After an initial pseudo elastic behavior (strain up to $\sim 0.5\%$), the first crack appeared and the stress decreased to reach an ideal plateau. The fluctuations around the average value in this second stage are generally attributed to successive brittle failures corresponding to individual struts crushing.

In this domain, the lattice showed a pseudo ductile behavior, although the constitutive material was fragile. When all cells were destroyed, densification was observed.

There is no reference in literature of fiber reinforced SiOC foams of similar porosity for a comparison. However, the samples already possess a higher compressive strength than the formerly produced hardystonite scaffolds for a similar porosity; they also overcame the performances of pure SiOC lattices found in literature (~ 2.5 MPa for a total porosity of ~ 64 vol%) [19]. These findings suggested that the carbon fiber reinforcement was increasing the mechanical properties of the samples; higher values can be expected once no residual cracks would be present in the structure.

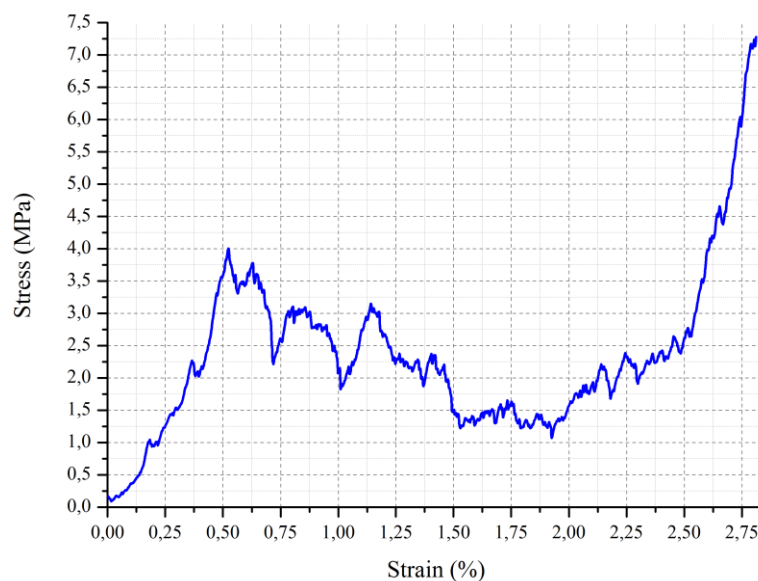


Fig. 1.31 - Stress-strain curve for a CF/(SiOC+SiC+FS) lattice loaded in compression.

Conclusions

DIW of ceramic matrix composites (CMCs) was investigated; the preceramic polymer developed a ceramic matrix (SiOC) upon pyrolysis in inert atmosphere, whereas the reinforcement was provided by the use of chopped carbon fibers.

Suitable formulations were investigated for the extrusion of fine filaments (< 1 mm diameter). Extrusion of inks with a relatively high amount of fibers, above 30 vol% on the CMC, was possible. The main issue encountered was the fact that the fibers hindered the shrinkage of the matrix during pyrolysis, resulting in severe cracks perpendicular to the filament axis. The solution was the addition of SiC powder as passive filler; such addition needed to be counteracted by the addition of fumed silica and a slight decrease in the amount of fibers, in order to maintain a printable ink.

A proper rheological characterization and optimization is still needed, but complex structures with porosity of ~75% and compressive strength of ~4 MPa were printed.

The process is of particular interest for its ability to orient the fibers in the extrusion direction due to the shear stresses generated at the nozzle tip: quantitative analysis on this phenomenon has not been performed yet, but microscopy investigation can already confirm it, opening the path to layer-by-layer design for gradually changing the mechanical properties within an object printed with a single material.

References

- [1] P. Colombo, G. Mera, R. Riedel, G.D. Sorarù, Polymer-Derived Ceramics: 40 Years of Research and Innovation in Advanced Ceramics, *J. Am. Ceram. Soc.* 1837 (2010) no-no. doi:10.1111/j.1551-2916.2010.03876.x.
- [2] M. Narisawa, S. Watase, K. Matsukawa, T. Dohmaru, K. Okamura, White Si-O-C(-H) particles with photoluminescence synthesized by decarbonization reaction on polymer precursor in a hydrogen atmosphere, *Bull. Chem. Soc. Jpn.* 85 (2012) 724–726. doi:10.1246/bcsj.20110357.
- [3] K.J. Kim, J.-H. Eom, Y.-W. Kim, W.-S. Seo, Electrical conductivity of dense, bulk silicon-oxycarbide ceramics, *J. Eur. Ceram. Soc.* 35 (2015) 1355–1360. doi:http://dx.doi.org/10.1016/j.jeurceramsoc.2014.12.007.
- [4] L. Toma, H.J. Kleebe, M.M. Müller, E. Janssen, R. Riedel, T. Melz, H. Hanselka, Correlation between intrinsic microstructure and piezoresistivity in a SiOC polymer-derived ceramic, *J. Am. Ceram. Soc.* 95 (2012) 1056–1061. doi:10.1111/j.1551-2916.2011.04944.x.
- [5] G.D. Sorarù, S. Modena, E. Guadagnino, P. Colombo, J. Egan, C. Pantano, Chemical Durability of Silicon Oxycarbide Glasses, *J. Am. Ceram. Soc.* 85 (2002) 1529–1536. doi:10.1111/j.1151-2916.2002.tb00308.x.
- [6] R. Zhuo, P. Colombo, C. Pantano, E.A. Vogler, Silicon oxycarbide glasses for blood-contact applications, *Acta Biomater.* 1 (2005) 583–589. doi:http://dx.doi.org/10.1016/j.actbio.2005.05.005.
- [7] G. Perale, C. Giordano, F. Daniele, M. Masi, P. Colombo, L. Gottardo, S. Maccagnan, A novel process for the manufacture of ceramic microelectrodes for biomedical applications, *Int. J. Appl. Ceram. Technol.* 5 (2008) 37–43. doi:10.1111/j.1744-7402.2008.02186.x.
- [8] P. Greil, Near Net Shape Manufacturing of Polymer Derived Ceramics, *Key Eng. Mater.* 132–136 (1997) 1981–1984. doi:10.4028/www.scientific.net/KEM.132-136.1981.
- [9] P. Greil, M. Seibold, Modelling of dimensional changes during polymer-ceramic conversion for bulk component fabrication, *J. Mater. Sci.* 27 (1992) 1053–1060. doi:10.1007/BF01197660.
- [10] E. Bernardo, P. Colombo, E. Pippel, J. Woltersdorf, Novel mullite synthesis based on alumina nanoparticles and a preceramic polymer, *J. Am. Ceram. Soc.* 89 (2006) 1577–1583. doi:10.1111/j.1551-2916.2006.00963.x.
- [11] P. Colombo, E. Bernardo, G. Parcianello, Multifunctional advanced ceramics from preceramic polymers and nano-sized active fillers, *J. Eur. Ceram. Soc.* 33 (2013) 453–469. doi:10.1016/j.jeurceramsoc.2012.10.006.

- [12] E. Bernardo, P. Colombo, I. Cacciotti, A. Bianco, R. Bedini, R. Pecci, K. Pardun, L. Treccani, K. Rezwan, Porous wollastonite-hydroxyapatite bioceramics from a preceramic polymer and micro- or nano-sized fillers, *J. Eur. Ceram. Soc.* 32 (2012) 399–408. doi:10.1016/j.jeurceramsoc.2011.08.010.
- [13] E. Bernardo, J.F. Carlotti, P.M. Dias, L. Fiocco, P. Colombo, L. Treccani, U. Hess, K. Rezwan, Novel akermanite-based bioceramics from preceramic polymers and oxide fillers, *Ceram. Int.* 40 (2014) 1029–1035. doi:10.1016/j.ceramint.2013.06.100.
- [14] H. Elsayed, A. Zocca, E. Bernardo, C.M. Gomes, J. Günster, P. Colombo, Development of bioactive silicate-based glass-ceramics from preceramic polymer and fillers, *J. Eur. Ceram. Soc.* 35 (2015) 731–739. doi:10.1016/j.jeurceramsoc.2014.09.020.
- [15] M. Mott, J.R.G. Evans, Solid freeforming of silicon carbide by ink-jet printing using a polymeric precursor, *J. Am. Chem. Soc.* 84 (2001) 307–313. doi:10.1111/j.1151-2916.2001.tb00655.x.
- [16] T. Friedel, N. Travitzky, F. Niebling, M. Scheffler, P. Greil, Fabrication of polymer derived ceramic parts by selective laser curing, *J. Eur. Ceram. Soc.* 25 (2005) 193–197. doi:10.1016/j.jeurceramsoc.2004.07.017.
- [17] A. Zocca, C.M. Gomes, A. Staude, E. Bernardo, J. Günster, P. Colombo, SiOC ceramics with ordered porosity by 3D-printing of a preceramic polymer, *J. Mater. Res.* 28 (2013) 2243–2252. doi:http://dx.doi.org/10.1557/jmr.2013.129.
- [18] A. Zocca, H. Elsayed, E. Bernardo, C.M. Gomes, M.A. Lopez-Heredia, C. Knabe, P. Colombo, J. Gunster, 3D-printed silicate porous bioceramics using a non-sacrificial preceramic polymer binder., *Biofabrication.* 7 (2015) 25008. doi:10.1088/1758-5090/7/2/025008.
- [19] G. Pierin, C. Grotta, P. Colombo, C. Mattevi, Direct Ink Writing of micrometric SiOC ceramic structures using a preceramic polymer, *J. Eur. Ceram. Soc.* 36 (2015) 1589–1594. doi:10.1016/j.jeurceramsoc.2016.01.047.
- [20] Z.C. Eckel, C. Zhou, J.H. Martin, A.J. Jacobsen, W.B. Carter, T.A. Schaedler, Additive manufacturing of polymer-derived ceramics, *Science* (80-.). 351 (2016) 58–62. doi:10.1126/science.aad2688.
- [21] R.R. Harsche, *Synthesis and Processing of Amorphous Si(Al)OC Bulk Ceramics: High Temperature Properties and Applications*, (2004).
- [22] E. Zanchetta, M. Cattaldo, G. Franchin, M. Schwentenwein, J. Homa, G. Brusatin, P. Colombo, Stereolithography of SiOC Ceramic Microcomponents, *Adv. Mater.* 28 (2016) 370–376. doi:10.1002/adma.201503470.

- [23] M. Schulz, Polymer derived ceramics in MEMS/NEMS – a review on production processes and application, *Adv. Appl. Ceram.* 108 (2009) 454–460. doi:10.1179/174367609X422171.
- [24] L.A. Liew, W. Zhang, L. An, S. Shah, R. Luo, Y. Liu, T. Cross, M.L. Dunn, V. Bright, J.W. Daily, R. Raj, K. Anseth, Ceramic MEMS new materials, innovative processing and future applications, *Am. Ceram. Soc. Bull.* 80 (2001) 25–30.
- [25] L.A. Liew, W. Zhang, V.M. Bright, L. An, M.L. Dunn, R. Raj, Fabrication of SiCN ceramic MEMS using injectable polymer-precursor technique, *Sensors Actuators, A Phys.* 89 (2001) 64–70. doi:10.1016/S0924-4247(00)00545-8.
- [26] J. Grossenbacher, M.R. Gullo, V. Bakumov, G. Blugan, J. Kuebler, J. Brugger, On the micrometre precise mould filling of liquid polymer derived ceramic precursor for 300-mm-thick high aspect ratio ceramic MEMS, *Ceram. Int.* 41 (2014) 623–629. doi:10.1016/j.ceramint.2014.08.112.
- [27] S.K. Reddy, N.B. Cramer, T. Cross, R. Raj, C.N. Bowman, Polymer-Derived Ceramic Materials from Thiol-ene Photopolymerizations, *Chem. Mater.* 15 (2003) 4257–4261. doi:10.1021/cm034291x.
- [28] L.A. Liew, Y. Liu, R. Luo, T. Cross, L. An, V.M. Bright, M.L. Dunn, J.W. Daily, R. Raj, Fabrication of SiCN MEMS by photopolymerization of pre-ceramic polymer, *Sensors Actuators, A Phys.* 95 (2002) 120–134. doi:10.1016/S0924-4247(01)00723-3.
- [29] T.A. Pham, D.-P. Kim, T.-W. Lim, S.-H. Park, D.-Y. Yang, K.-S. Lee, Three-Dimensional SiCN Ceramic Microstructures via Nano-Stereolithography of Inorganic Polymer Photoresists, *Adv. Funct. Mater.* 16 (2006) 1235–1241. doi:10.1002/adfm.200600009.
- [30] X. Liu, Y.L. Li, F. Hou, Fabrication of SiOC ceramic microparts and patterned structures from polysiloxanes via liquid cast and pyrolysis, *J. Am. Ceram. Soc.* 92 (2009) 49–53. doi:10.1111/j.1551-2916.2008.02849.x.
- [31] Y. Xu, M. Guron, X. Zhu, L.G. Sneddon, S. Yang, Template synthesis of 3D high-temperature silicon-oxycarbide and silicon-carbide ceramic photonic crystals from interference lithographically patterned organosilicates, *Chem. Mater.* 22 (2010) 5957–5963. doi:10.1021/cm102204e.
- [32] S. Martínez-Crespiera, E. Ionescu, M. Schlosser, K. Flittner, G. Mistura, R. Riedel, H.F. Schlaak, Fabrication of silicon oxycarbide-based microcomponents via photolithographic and soft lithography approaches, *Sensors Actuators, A Phys.* 169 (2011) 242–249. doi:10.1016/j.sna.2011.04.041.
- [33] S. Martínez-Crespiera, E. Ionescu, H.J. Kleebe, R. Riedel, Pressureless synthesis of fully dense and crack-free SiOC bulk ceramics via photo-crosslinking and pyrolysis of a

- polysiloxane, *J. Eur. Ceram. Soc.* 31 (2011) 913–919. doi:10.1016/j.jeurceramsoc.2010.11.019.
- [34] K.A. Davis, J.A. Burdick, K.S. Anseth, Photoinitiated crosslinked degradable copolymer networks for tissue engineering applications, *Biomaterials*. 24 (2003) 2485–2495. doi:10.1016/S0142-9612(02)00582-3.
- [35] P. Innocenzi, G. Brusatin, A comparative FTIR study of thermal and photo-polymerization processes in hybrid sol-gel films, *J. Non. Cryst. Solids*. 333 (2004) 137–142. doi:10.1016/j.jnoncrysol.2003.09.043.
- [36] S. Gardin, R. Signorini, A. Pistore, G. Della Giustina, G. Brusatin, M. Guglielmi, R. Bozio, Photocatalytic Performance of Hybrid SiO₂–TiO₂ Films, *J. Phys. Chem. C*. 114 (2010) 7646–7652. doi:10.1021/jp911495h.
- [37] E. Zanchetta, M. Cattaldo, G. Franchin, M. Schwentenwein, J. Homa, G. Brusatin, P. Colombo, Supporting Information for Stereolithography of SiOC Ceramic Microcomponents, *Adv. Mater.* 28 (2016) 370–376. doi:10.1002/adma.201503470.
- [38] A.R. Studart, U.T. Gonzenbach, E. Tervoort, L.J. Gauckler, Processing Routes to Macroporous Ceramics: A Review, *J. Am. Ceram. Soc.* 89 (2006) 1771–1789. doi:10.1111/j.1551-2916.2006.01044.x.
- [39] A. Zocca, G. Franchin, H. Elsayed, E. Gioffredi, E. Bernardo, P. Colombo, Direct Ink Writing of a Pre-ceramic Polymer and Fillers to Produce Hardystonite (Ca₂ZnSi₂O₇) Bioceramic Scaffolds, *J. Am. Ceram. Soc.* 99 (2016) 1960–1967. doi:10.1111/jace.14213.
- [40] Y. Ramaswamy, C. Wu, H. Zhou, H. Zreiqat, Biological response of human bone cells to zinc-modified Ca–Si-based ceramics, *Acta Biomater.* 4 (2008) 1487–1497. doi:10.1016/j.actbio.2008.04.014.
- [41] C. Wu, J. Chang, W. Zhai, A novel hardystonite bioceramic: Preparation and characteristics, *Ceram. Int.* 31 (2005) 27–31. doi:10.1016/j.ceramint.2004.02.008.
- [42] E.R. Segnit, The System CaO–ZnO–SiO₂, *J. Am. Ceram. Soc.* 37 (1954) 273–277. doi:10.1111/j.1151-2916.1954.tb14036.x.
- [43] S.R. Raghavan, S.A. Khan, Shear-induced microstructural changes in flocculated suspensions of fumed silica, *J. Rheol.* 39 (1995) 1311–1325. doi:10.1122/1.550638.
- [44] J.-N. Paquien, J. Galy, J.-F. Gérard, A. Pouchelon, Rheological studies of fumed silica–polydimethylsiloxane suspensions, *Colloids Surfaces A Physicochem. Eng. Asp.* 260 (2005) 165–172. doi:10.1016/j.colsurfa.2005.03.003.
- [45] M. Zhang, K. Lin, J. Chang, Preparation and characterization of Sr–hardystonite (Sr₂ZnSi₂O₇) for bone repair applications, *Mater. Sci. Eng. C*. 32 (2012) 184–188.

doi:10.1016/j.msec.2011.10.017.

- [46] J.E. Smay, J. Cesarano, J.A. Lewis, Colloidal Inks for Directed Assembly of 3-D Periodic Structures, *Langmuir*. 18 (2002) 5429–5437. doi:10.102/la0257135.
- [47] T. Schlordt, F. Keppner, N. Travitzky, P. Greil, Robocasting of Alumina Lattice Truss Structures, *J. Ceram. Sci. Technol.* 3 (2012) 1–7. doi:10.4416/JCST2012-00003.
- [48] J. Schindelin, I. Arganda-Carreras, E. Frise, V. Kaynig, M. Longair, T. Pietzsch, S. Preibisch, C. Rueden, S. Saalfeld, B. Schmid, J.-Y. Tinevez, D.J. White, V. Hartenstein, K. Eliceiri, P. Tomancak, A. Cardona, Fiji: an open-source platform for biological-image analysis, *Nat. Methods*. 9 (2012) 676–682. doi:10.1038/nmeth.2019.
- [49] J.G. Dellinger, J. Cesarano, R.D. Jamison, Robotic deposition of model hydroxyapatite scaffolds with multiple architectures and multiscale porosity for bone tissue engineering, *J. Biomed. Mater. Res. Part A*. 82A (2007) 383–394. doi:10.1002/jbm.a.31072.
- [50] W.H. Herschel, R. Bulkley, Measurement of consistency as applied to rubber-benzene solutions, in: *Am. Soc. Test Proc*, 1926: pp. 621–633.
- [51] V. Tirtaatmadja, K.C. Tam, R.D. Jenkins, Superposition of Oscillations on Steady Shear Flow as a Technique for Investigating the Structure of Associative Polymers, *Macromolecules*. 30 (1997) 1426–1433. doi:10.1021/ma960098v.
- [52] J.A. Lewis, Direct ink writing of 3D functional materials, *Adv. Funct. Mater.* 16 (2006) 2193–2204.
- [53] R.H. Baney, M. Itoh, A. Sakakibara, T. Suzuki, Silsesquioxanes, *Chem. Rev.* 95 (1995) 1409–1430. doi:10.1021/cr00037a012.
- [54] F. Vivier, D. Santamaria, D. Pellerej, P. Buonficio, M. Sangermano, A Kinetic Analysis of a Thermal Curing Reaction of a Silicon Resin in Solid State, in: J.S. Carpenter, C. Bai, J.-Y. Hwang, S. Ikhmayies, B. Li, S.N. Monteiro, Z. Peng, M. Zhang (Eds.), *Charact. Miner. Met. Mater.* 2014, John Wiley & Sons, Inc., 2014: pp. 63–72.
- [55] D. Yang, W. Zhang, B. Jiang, Ceramization and oxidation behaviors of silicone rubber ablative composite under oxyacetylene flame, *Ceram. Int.* 39 (2013) 1575–1581. doi:10.1016/j.ceramint.2012.07.109.
- [56] A. Bignon, J. Chouteau, J. Chevalier, G. Fantozzi, J.-P. Carret, P. Chavassieux, G. Boivin, M. Melin, D. Hartmann, Effect of micro- and macroporosity of bone substitutes on their mechanical properties and cellular response, *J. Mater. Sci. Mater. Med.* 14 (2003) 1089–1097. doi:10.1023/B:JMSM.0000004006.90399.b4.
- [57] O. Chan, M.J. Coathup, A. Nesbitt, C.-Y. Ho, K.A. Hing, T. Buckland, C. Champion, G.W. Blunn, The effects of microporosity on osteoinduction of calcium phosphate bone graft

- substitute biomaterials, *Acta Biomater.* 8 (2012) 2788–2794. doi:10.1016/j.actbio.2012.03.038.
- [58] H.J.T. Ellingham, Reducibility of Oxides and Sulfides in Metallurgical Processes, *J. Soc. Chem. Ind.* 63 (1944) 125–133.
- [59] A. Berman, M. Epstein, The kinetic model for carboreduction of zinc oxide, *Le J. Phys.* IV. 9 (1999) Pr3–319.
- [60] G. Wang, Z. Lu, D. Dwarte, H. Zreiqat, Porous scaffolds with tailored reactivity modulate in-vitro osteoblast responses, *Mater. Sci. Eng. C.* 32 (2012) 1818–1826. doi:10.1016/j.msec.2012.04.068.
- [61] S.I. Roohani-Esfahani, C.R. Dunstan, J.J. Li, Z. Lu, B. Davies, S. Pearce, J. Field, R. Williams, H. Zreiqat, Unique microstructural design of ceramic scaffolds for bone regeneration under load, *Acta Biomater.* 9 (2013) 7014–7024. doi:10.1016/j.actbio.2013.02.039.
- [62] F. Raether, Ceramic Matrix Composites – an Alternative for Challenging Construction Tasks, *Ceram. Applications.* 1 (2013) 45–49.
- [63] A.G. Evans, D.B. Marshall, Overview no. 85 The mechanical behavior of ceramic matrix composites, *Acta Metall.* 37 (1989) 2567–2583. doi:10.1016/0001-6160(89)90291-5.
- [64] K. Tushtev, J. Horvath, D. Koch, G. Grathwohl, Deformation and failure modeling of fiber reinforced ceramics with porous matrix, *Adv. Eng. Mater.* 6 (2004) 664–669. doi:10.1002/adem.200400094.
- [65] B.G. Compton, J.A. Lewis, 3D-printing of lightweight cellular composites, *Adv. Mater.* 26 (2014) 5930–5935. doi:10.1002/adma.201401804.
- [66] P. Calvert, T.L. Lin, H. Martin, Extrusion freeform fabrication of chopped-fibre reinforced composites, *High Perform. Polym.* 9 (1997) 449–456. doi:10.1088/0954-0083/9/4/008.
- [67] S. Christ, M. Schnabel, E. Vorndran, J. Groll, U. Gbureck, Fiber reinforcement during 3D printing, *Mater. Lett.* 139 (2015) 165–168. doi:10.1016/j.matlet.2014.10.065.
- [68] S.J. Leigh, R.J. Bradley, C.P. Pursell, D.R. Billson, D.A. Hutchins, A simple, low-cost conductive composite material for 3D printing of electronic sensors., *PLoS One.* 7 (2012) e49365. doi:10.1371/journal.pone.0049365.
- [69] D. Kokkinis, M. Schaffner, A.R. Studart, Multimaterial magnetically assisted 3D printing of composite materials, *Nat. Commun.* 6 (2015) 8643. doi:10.1038/ncomms9643.
- [70] R.M. Erb, R. Libanori, N. Rothfuchs, A.R. Studart, Composites Reinforced in Three Dimensions by Using Low Magnetic Fields, *Science (80-.).* 335 (2012) 199–204.
- [71] H.L. Tekinalp, V. Kunc, G.M. Velez-Garcia, C.E. Duty, L.J. Love, A.K. Naskar, C.A. Blue,

- S. Ozcan, Highly oriented carbon fiber-polymer composites via additive manufacturing, *Compos. Sci. Technol.* 105 (2014) 144–150. doi:10.1016/j.compscitech.2014.10.009.
- [72] P. Colombo, M. Modesti, Silicon Oxycarbide Ceramic Foams from a Pre ceramic Polymer, *J. Am. Ceram. Soc.* 82 (1999) 573–578.
- [73] J. Peng, T.L. Lin, P. Calvert, Orientation effects in freeformed short-fiber composites, *Compos. Part A Appl. Sci. Manuf.* 30 (1999) 133–138. doi:10.1016/S1359-835X(98)00110-9.
- [74] L.J. Gibson, M.F. Ashby, *Cellular solids. Structure and properties*, (1997) 502. doi:10.1017/CBO9781139878326.

2. Geopolymers

Geopolymers are inorganic materials with a chemical composition similar to that of zeolite and a variable microstructure (amorphous to semi-crystalline). Their synthesis involves the reaction between SiO_2 and Al_2O_3 species in a highly alkaline medium, leading to the formation of a continuous three-dimensional network. The exchange of silicon for aluminum in the network structure results in a net negative charge which is compensated by alkali cations. These materials can consolidate at low, even room temperature, leading to amorphous microstructures; heat treatment at temperatures $> 500\text{ }^\circ\text{C}$ results in semi-crystalline structures resembling zeolites ones [1].

In the late 1970's, Davidovits coined the term geopolymer to classify the newly discovered inorganic polymeric materials produced via polycondensation reaction; he also classified these silicate and aluminosilicate materials according to the Si:Al atomic ratio (see Fig. 2.1).

Table 2.1 - Silicate and aluminosilicate classification based on Si:Al atomic ratio.

Si:Al atomic ratio	Nomenclature	Applications
0	Siloxo	Bricks, ceramics, fire protection.
1	Sialate	Cements and concretes, radioactive waste encapsulation.
2	Sialate-siloxo	Foundry equipments, tools for Ti processing, fire protection fiber glass composites (heat resistance up to $1000\text{ }^\circ\text{C}$).
3	Sialate-disiloxo	Sealants for industry (up to $600\text{ }^\circ\text{C}$), tools for Al SPF.
> 3	Sialate link	Fire and heat resistant fiber composites.

The atomic ratio Si:Al in the poly(sialate) structure determines the properties and applications. A low ratio Si:Al (< 3) produces a 3D-Network that is very rigid. The higher the Si:Al ratio, the higher the polymeric character provided to the geopolymeric material.

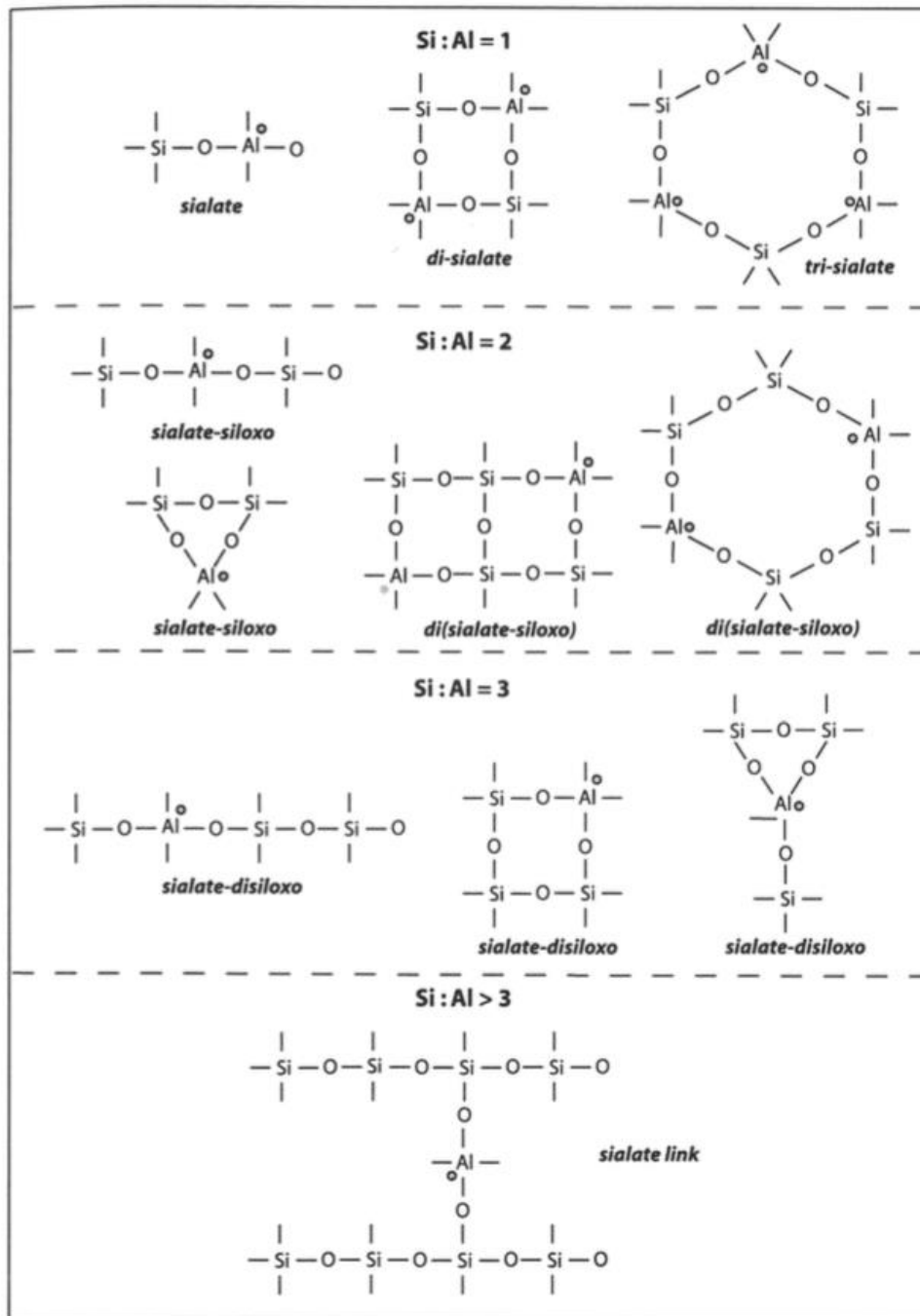


Fig. 2.1 - Aluminosilicate classification based on Si:Al atomic ratio [1].

Most of the geopolymer compositions are synthesized following the alkaline route, which involves the polycondensation reaction of dehydroxylated aluminium silicate (such as calcinated kaolinite or metakaolin, general formula $\text{Al}_2\text{O}_3 \cdot 2\text{SiO}_2$) within an alkaline medium comprising hydroxides and alkali-silicates.

However, geopolymers can also be synthesized via an acidic route, mainly in a phosphoric acid-based medium, leading to poly(phosphor-siloxo) and poly(alumino-phospho) phases.

The geopolymerization reaction involves several phases as schematized in Fig. 2.2. First, the poly(siloxo) layers of the aluminosilicate source are depolymerized by the alkaline (or acidic) medium, leading to the formation of ortho-sialate molecules; then, the interaction between these molecules and the alkaline species in solution leads to the polycondensation into oligomers (gelation) and polymeric network (solidification and hardening).

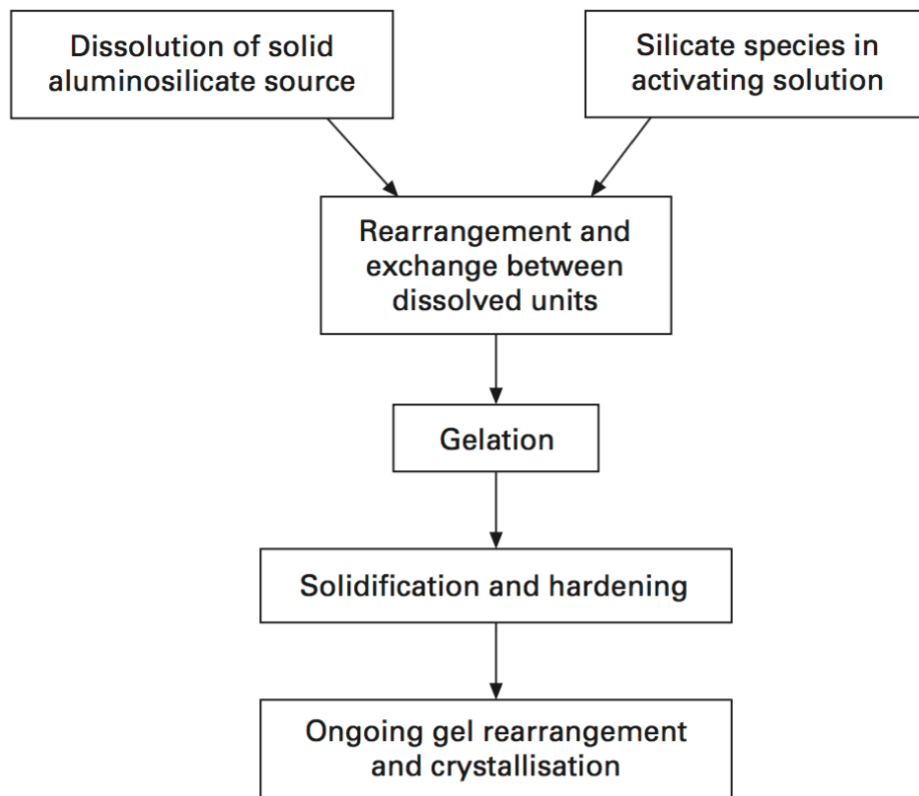
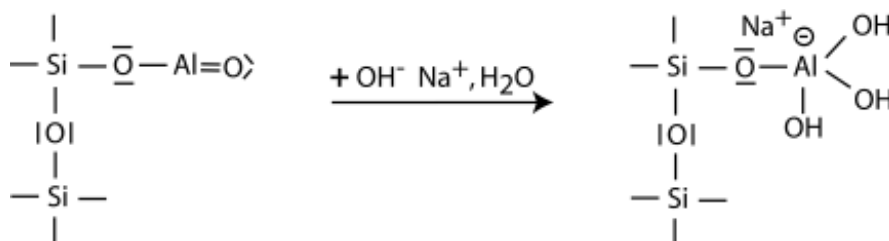


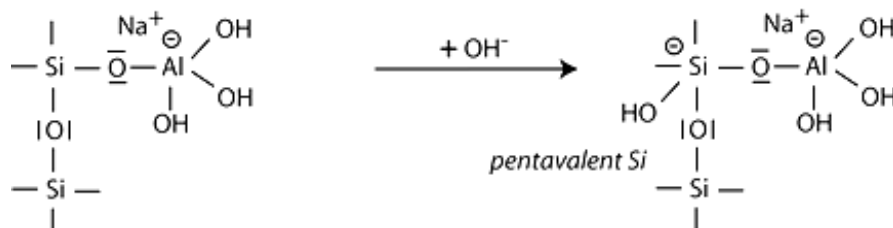
Fig. 2.2 - Geopolymerization steps [2].

An example of geopolymerization reaction starting from metakaolin calcinated at 750 °C is here reported for clarity; it refers to Na⁺ as alkaline cation [3]. The geopolymerization kinetics for Na-poly(sialate-siloxo) and K-poly(sialate-siloxo) are slightly different, probably due to the different dimensions of the Na⁺ and K⁺ cations; however, the mechanism can be generalized to K⁺ and other cations.

Step 1: alkalination tetravalent Al formation in the sialate side groups:



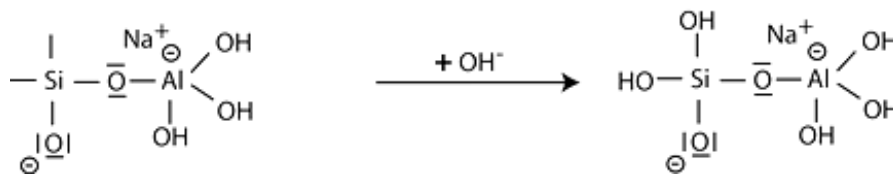
Step 2: alkaline dissolution and OH⁻ attachment to Si, which turns into a penta-covalent site:



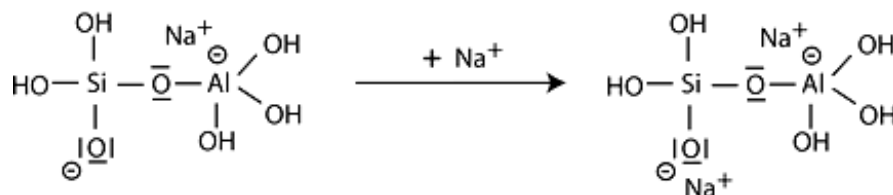
Step 3: formation of silanol Si-OH and siloxo Si-O⁻:



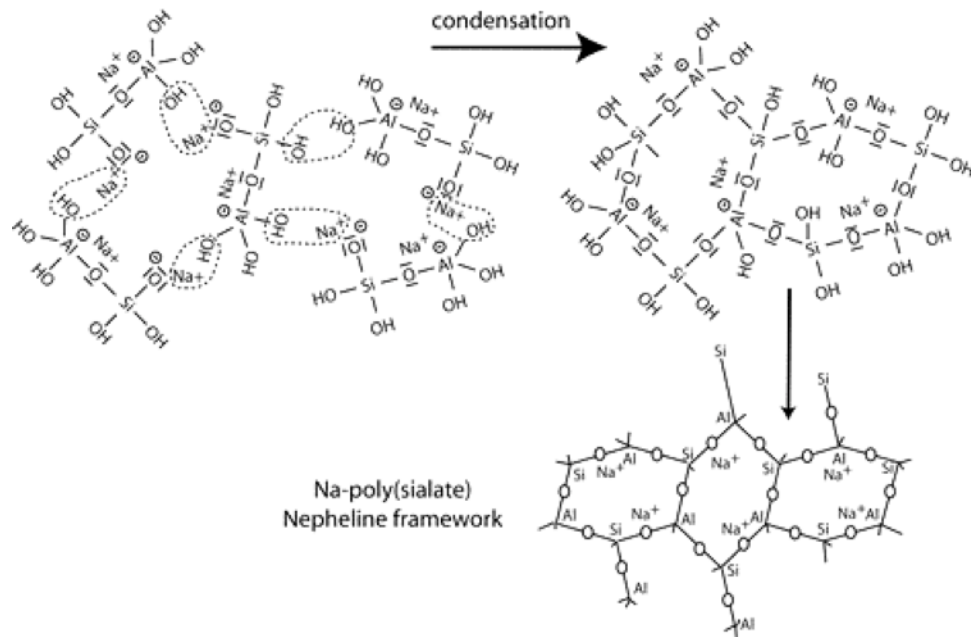
Step 4: further formation of Si-OH groups and isolation of the primary ortho-sialate unit:



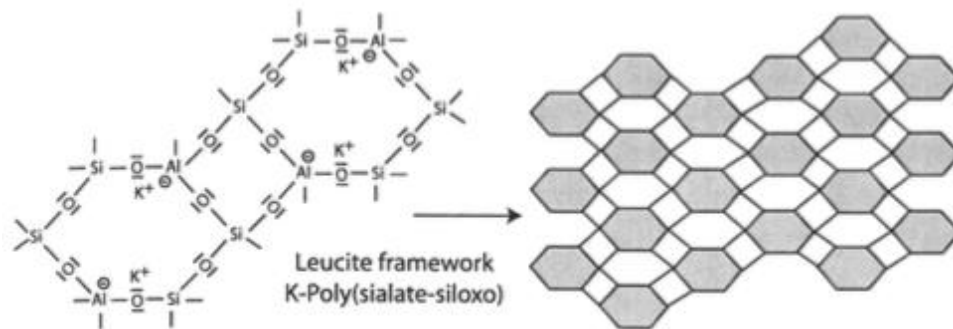
Step 5: reaction of Si-O⁻ with Na⁺ and formation of Si-O-Na terminal bond:



Step 6: condensation between primary ortho-sialate units, reactive groups Si-O⁻Na⁺ and aluminum hydroxyl OH-Al to create a cyclo-tri-sialate structure; NaOH is liberated and reacts again leading to further polycondensation into Na-poly(sialate) nepheline framework.



Reaction with KOH and potassium silicates follows the same mechanisms and leads to formation of a K-poly(sialate-siloxo) leucite framework.



The primary area of application of geopolymers is currently in the development of low-CO₂ construction materials as a greener alternative to Portland-based cements; they can provide other technological advantages over traditional construction materials. Other applications include host matrix in waste encapsulation, as a low-cost ceramic (either used directly or as a precursor for calcination), and in fire protection of structures.

All mentioned applications do not require complex processes: geopolymer production has so far been performed through simple casting of the geopolymeric slurry into molds or pre-forms. The focus on conventional manufacturing has so far limited the exploration of other applications, such as filters and catalyst carriers, which could take advantage of the geopolymer zeolite-like composition and intrinsic mesoporosity [2]; in fact, complex shapes and high aspect ratio are needed which cannot be fabricated by casting.

Geopolymer foams can be produced adding preoxides and oils to the slurry; in fact, geopolymer gelcasting can be combined with a saponification reaction of different oils and fats with the hydroxides present in the slurry leading to formation of an open pores network [4,5]. Similar foams have recently been proven as suitable for filtering applications [6].

However, the use of precisely designed, non stochastic printed structures could potentially enhance the mechanical properties of the porous components, provide a better control of pressure drop and fluid dynamics inside the part and improve their performances consistently compared to foamed components. In a very recent publication, Xia and Sanjayan reported on the use of geopolymers associated with powder-based 3D printing; they were able to print samples with good accuracy, but densification is still an issue (which is typical of a powder-based approach) and it reflects on poor mechanical properties[7]. Few 3D printing companies and research groups started experimenting with large scale additive manufacturing of standard cement and concrete and are trying to progress to geopolymer based ones, but their focus is almost entirely on working time and mechanical resistance for the fabrication of simple shape buildings[8,9]. Little work has been so far conducted on direct ink writing of geopolymers, which would be less time consuming with respect to other AM technologies, would not produce any waste material and would allow to fabricate more complex shapes.

Negative replica of PLA printed structures with geopolymers

Partially published in:

Franchin, G., Colombo, P.: Porous Geopolymer Components through Inverse Replica of 3D Printed Sacrificial Templates. J. Ceram. Sci. Tech. 2015, 6 (2), 105-112 [10]

The goal of this section was to combine a negative replica technique with geopolymer casting; the requirements in terms of rheological behavior for the infiltrating slurries were much less stringent in comparison to the strict control needed for the fabrication of high-quality structures by direct printing, and allowed to experiment with different compositions and shapes.

Materials and Methods

Slurry preparation

A synthetic metakaolin (Argical 1200S, Imerys S. A., Paris, FR) and class F fly ash (#200 mesh; Tractebel Energia, Florianopolis, BR) were used as geopolymeric precursors; potassium hydroxide pellets (KOH, Dinâmica Química Contemporânea Ltda, Sao Paulo, BR) and potassium silicate solution (KSIL 0465, Crosfield Italia Srl, Montorio, IT) were used as alkaline activators. Their composition is reported in Table 2.2.

Table 2.2 – Chemical composition of the raw materials.

Reagent	SiO ₂ (wt%)	Al ₂ O ₃ (wt%)	K ₂ O (wt%)	Fe ₂ O ₃ (wt%)	CaO (wt%)	H ₂ O (wt%)
Argical 1200 S	55	39	< 1	1.8	< 0.6	/
Class F fly ash	55.3	19.8	2.3	10.2	1.3	/
KSIL 0465	22.5 - 24	/	11 – 12.5	/	/	64.5 – 66.1

The first step in the preparation of the geopolymer slurry was the preparation of a 15M KOH solution. Once KOH had dissolved completely in distilled water, a solution of potassium hydroxide and potassium silicate was prepared in a mixer (500 rpm, 5 min), according to the following weight ratio: KSIL 0465/KOH (15M) = 1.86. The alkaline solution was prepared 24 hours in advance to let the silicate dissolve completely [11].

The geopolymer slurry was designed according to the following molar ratios: SiO₂/Al₂O₃=4, K₂O/SiO₂=0.25 and H₂O/K₂O=15.83.

The metakaolin powder was added at room temperature and stirred at 800 rpm for 30 min, followed by the addition of the fly ash and stirring at 1000 rpm for other 30 min. An addition of 50 wt% of fly ash with respect to Argical was used.

Negative replica of PLA sacrificial templates

Sacrificial templates were designed and printed with the Powerwasp Evo (Wasproject, Massa Lombarda, IT) FDM printer presented in the previous chapter. A poly(lactic acid) filament (PLA, 3 mm diameter; Wasproject, Massa Lombarda, IT) was used to print the lattices with a layer height of 100 μm and a layer width of 350 μm (corresponding to the nozzle diameter).

The chosen geometries were four different templates of 15 x 15 x 15 mm³ with open interconnected channels with 3 x 3 mm² sections or 1.5 x 3 mm² sections. Three sides of each mold had closed walls in order to avoid leaking of the slurry during infiltration, and the fourth was closed with a lid.

Fig. 2.3 shows the different template designs (left) as well as the inverse lattices (right). The solid struts in the PLA scaffold would become the macropores in the inverse replica structure.

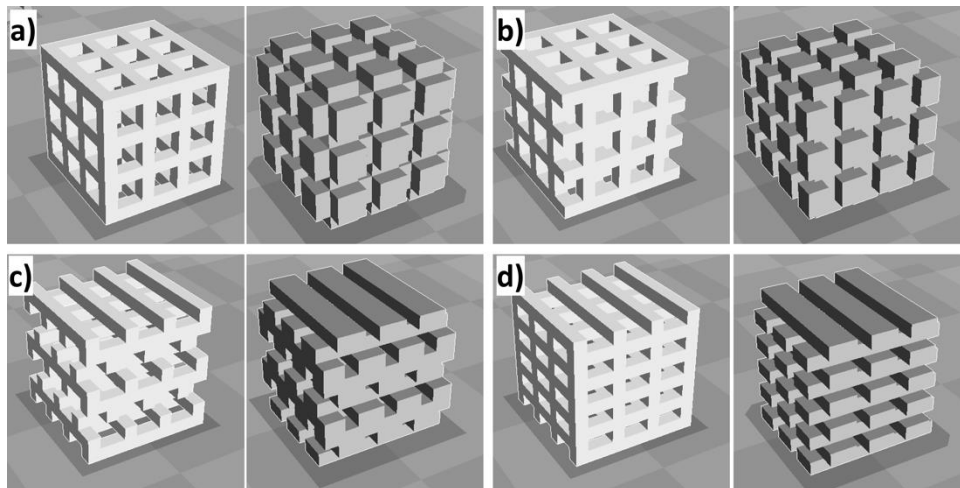


Fig. 2.3 - 3D rendering of the sacrificial templates. Templates used for the geopolymer impregnation (left) and inverse lattices (right) [10].

Right after mixing, the slurry was poured into the molds and then left under rotary-pump-vacuum (~ 0.1 Pa) for 15 min. The molds were then sealed with cling film and left at room temperature for 48 - 72 hours to allow for the completion of the geopolymerization reaction.

In order to remove the sacrificial PLA templates, the samples were first directly immersed in KOH 15M at 72 °C for 24 hours; the basic solution carried out a nucleophilic attack of the polymer chain links, leading to their partial hydrolysis and condensation [12]. Samples were then washed with hot water to extract the PLA; this step also confirmed the extent of the geopolymerization reaction, since unreacted material would be sensitive to water and undergo swelling or complete destruction [1]. Finally, the samples were heat treated at 330°C for 24 hours in a tube furnace under air flux (heating rate = 1 °C/min).

The coupled chemo-thermal treatment was already reported to remove the PLA completely with no damage to the geopolymeric structure in the case of geopolymer additivated with PLA fibers [13].

Characterization

The morphology and microstructure of the samples were investigated using an optical stereoscope (STEMI 2000-C, Carl Zeiss AG, Oberkochen, DE) and a SEM (ESEM, Quanta 200, FEI, Hillsboro, OR). X-Ray diffraction analysis (D8 Advance, Bruker Italia Srl, Milano, IT) was performed on powdered samples with Cu K α radiation (10–70° 2 θ , 2 s/step).

The true density of the ground geopolymer was measured with a helium pycnometer on finely crushed powders (Accupyc 1330, Micromeritics, Norcross, GA). The open, closed and total porosity of the struts was quantified by the Archimedes' method using water as the infiltrating fluid. The designed total porosity was calculated as the ratio between the volume occupied by the model lattice and the volume of the cube encapsulating the object. The total porosity of the lattices was calculated by weighing the samples on a digital scale and measuring their size using a digital caliper, taking into account the measured true density. Specific surface area (SSA) data were collected through N₂ adsorption experiments at liquid nitrogen temperature using a Quantachrome Nova Station A (Quantachrome Instruments, Boynton Beach, FL). All samples were degassed at 250°C prior to the nitrogen adsorption measurements. The Brunauer-Emmett-Teller specific surface area was determined by the multipoint BET method using the adsorption data in the relative pressure (P/P₀) range of 0.05 – 0.3.

Results and Discussion

PLA templates infiltrated with the solidified geopolymer slurry are shown in Fig. 2.4, together with details of the PLA templates; small discrepancies from the model lattices were due to the limits of the FDM deposition, which tends to accumulate excess material in small areas and is affected by gravity when printing overhangs. With the aid of the rotary-pump-vacuum, the slurry penetrated in all designed macroscopic cavities and no voids or bubbles could be detected.

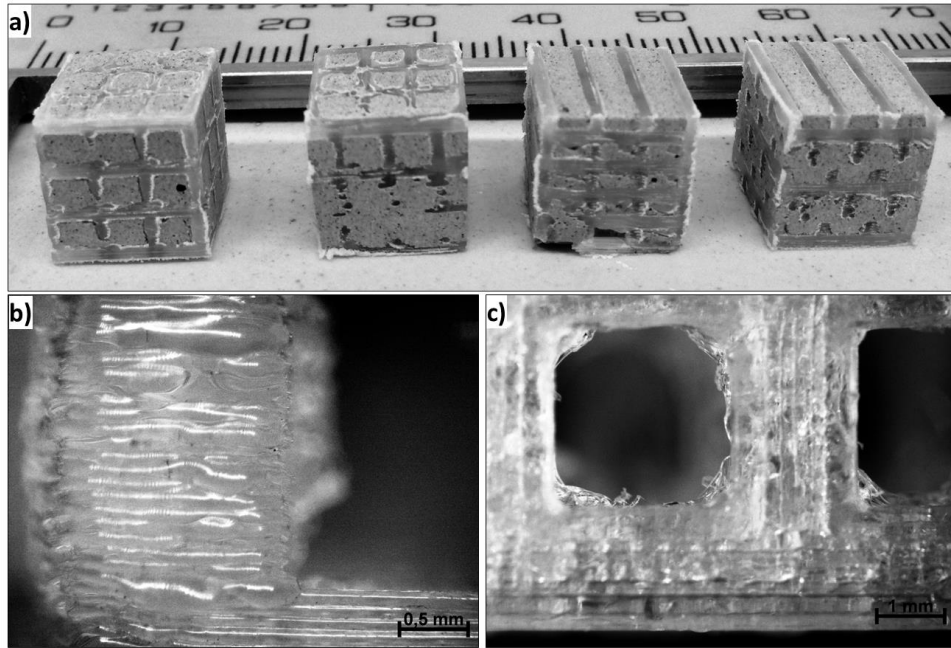


Fig. 2.4 -Picture of some PLA templates infiltrated with the geopolymer slurry (a), and stereomicroscope details of the PLA template ((b): side view; (c): top view) [10].

The PLA removal process combined a chemical and a thermal treatment. A simple direct heat treatment of the impregnated samples resulted in the destruction of the samples or in severe cracking of the components: the large mismatch in the thermal expansion of the geopolymer and the polymeric template led due to the development of high thermal stresses upon heating. The chemical treatment, on the other hand, was not sufficient for a complete decomposition of the sacrificial template.

A combination of the two treatments resulted in the geopolymeric lattices shown in Fig. 2.5. The inverse replica of the printed structures looked very accurate; the structures showed negligible shrinkage. Occasional cracks could still be observed, suggesting the need to further improving the removal step of the PLA template.

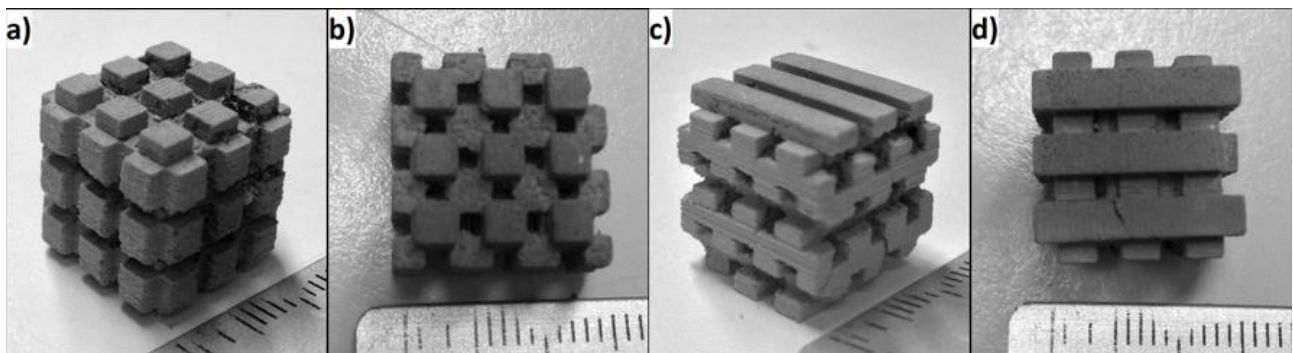


Fig. 2.5 - Inverse replica of the four lattices after complete PLA degradation [10].

Fig. 2.6 shows close-ups of the top and side of the structure in Fig. 2.5(a). No bubbles were observed in the geopolymeric struts. The slurry replicated also the roughness corresponding on the layer-by-layer build up of the PLA template; the detailed and accurate replicas obtained indicated that the proposed approach based on the FDM of highly interconnected sacrificial templates is suitable for the fabrication of complex macroporous ceramic parts.

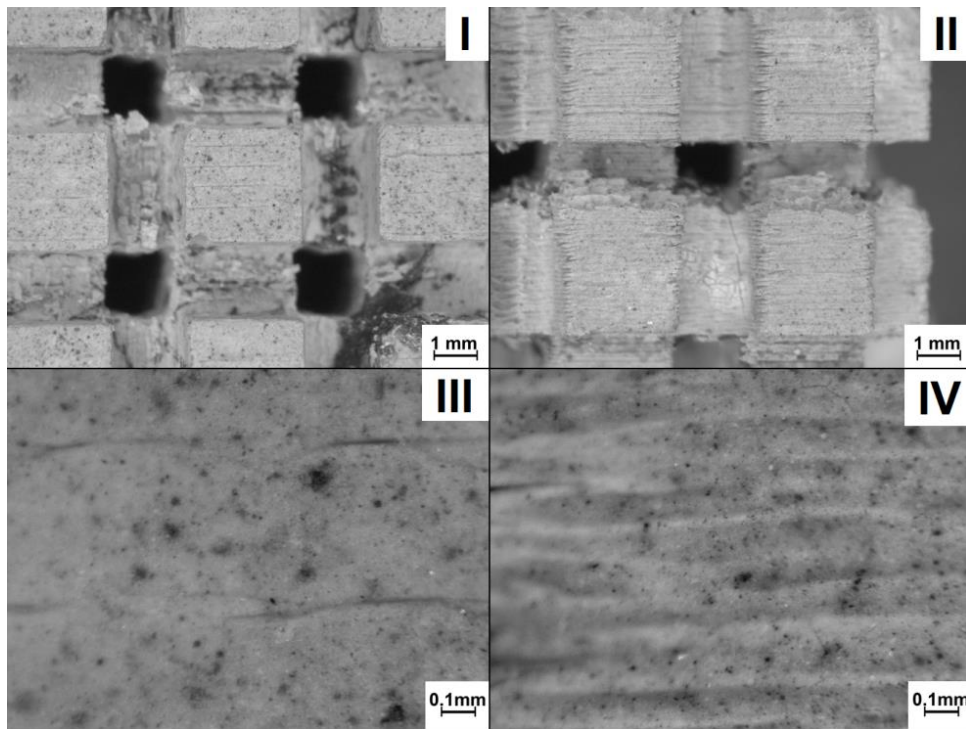


Fig. 2.6 - Stereomicroscopic images of a lattice: (a) (I) top view; (II) side view; detail of top (III) and (IV) side surfaces showing their morphological characteristics (template-derived roughness) [10].

SEM images of the geopolymer are shown in Fig. 2.7. Residual fly ashes (particularly rich in Fe and Ti) was embedded in an amorphous/microcrystalline alumino-silicate matrix; several small pores (1 - 10 μm) could be detected. They were probably due to the evaporation of the excess water, as it is unlikely that residual air was present in the slurry after pulling vacuum.

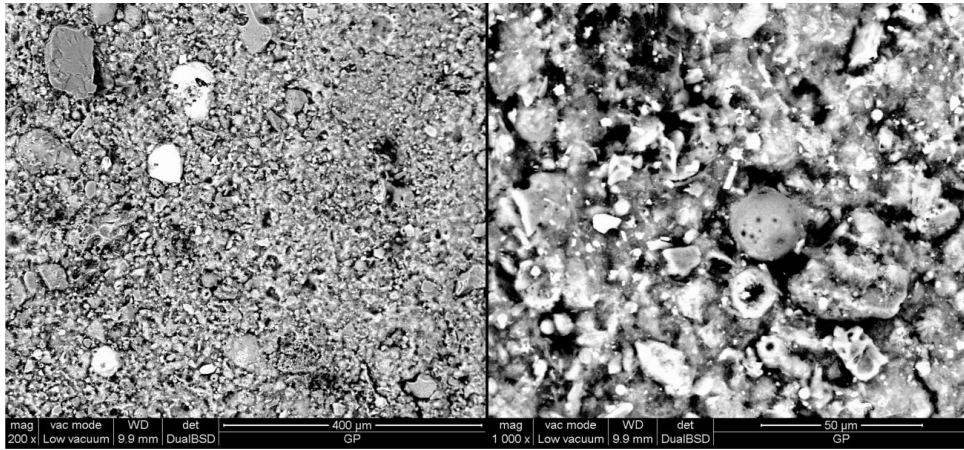


Fig. 2.7 -SEM images of the microstructure of the geopolymer [10].

Crushed geopolymer powder was investigated by XRD analysis, which reported a mainly amorphous matrix with quartz and muscovite impurities typical of metakaolin based geopolymers not treated at high temperature [14].

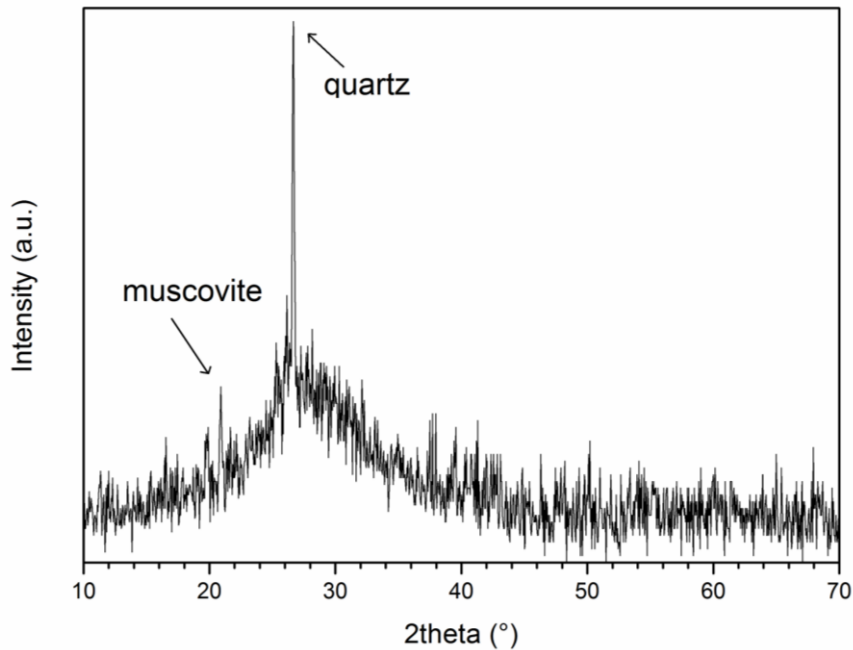


Fig. 2.8 -XRD analysis after heat treatment at 330 °C [10].

Geopolymer struts had a bulk density of $1.30 \pm 0.01 \text{ g/cm}^3$ and an apparent one of $2.23 \pm 0.01 \text{ g/cm}^3$; their true density was $2.4367 \pm 0.0002 \text{ g/cm}^3$. The total porosity of the struts and of the lattices is reported in Table 2.3. The designed macroporosity was different among the various lattice models, ranging from 35.2% to 40%. The total porosity of the structures ranged from ~66% to ~71%, indicating that the absolute contribution of the struts porosity to the total porosity was ~30 vol%.

Table 2.3 - Porosity of lattices and struts.

Lattice structure type	a	b	c	d
Measured total porosity (vol%)	66.2 ± 1.0	70.9 ± 3.1	66.4 ± 0.8	70.2 ± 2.2
Model macroporosity (vol%)	35.2	40	36	40
Struts total porosity (vol%)		46.72 ± 0.42		
Struts open porosity (vol%)		41.87 ± 0.67		

While the macroscopic open channels, with a designed size and volume, would enable suitable permeability for liquid or gas through the porous scaffold, the solid struts would be responsible for the interaction with the fluid when the component is used for filtration or as a catalytic support. The porosity of the struts was almost entirely open and interconnected.

The N₂ adsorption and desorption curves are reported in Fig. 2.9; the isotherms could be classified as type IV, according to the International Union of Pure and Applied Chemistry (IUPAC). Both micropores (diameter < 2 nm, detected by N₂ adsorption at P/P₀ < 0.15) and mesopores (diameter = 2 - 50 nm, detected by the hysteresis at higher values of relative pressure) were present. The inherent chemical micro- and mesoporosity of geopolymers is due to the polycondensation of aluminosilicates during geopolymerization reaction, which produces water, and on the fact that their morphology at the nanometric scale is based on the assemblage of small spheroidal particles [1]. As this inherent porosity developed during the geopolymerization reaction, it was not affected by the application of vacuum during infiltration. The specific surface area of the samples was 22.991 m²/g, in accordance to values reported in literature for potassium containing geopolymers based on metakaolin and fly ash [15–20]. Preliminary mechanical testing resulted in an average compressive strength value of ~8.5 MPa for samples with an architecture (a).

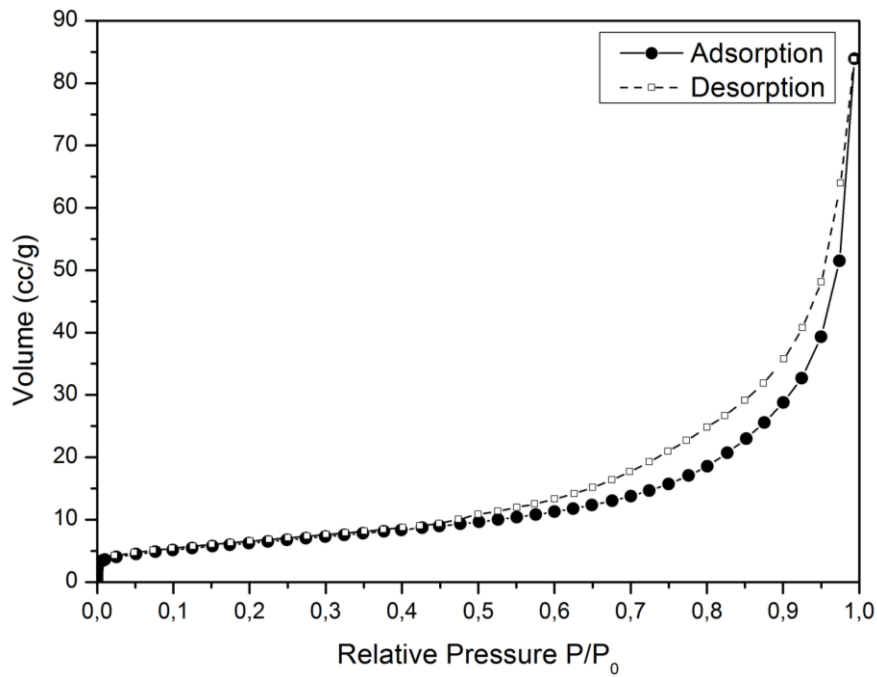


Fig. 2.9 -Adsorption and desorption isotherms on powders obtained by crushing a geopolymer scaffold [10].

As a proof-of-concept, a geopolymer slurry containing oil and hydrogen peroxide was employed for the infiltration to generate foamed struts via a peroxide/saponification combined route [4]. Fig. 2.10 shows struts with an additional level of porosity, with partially interconnected pores ranging from ~50 to ~300 μm .

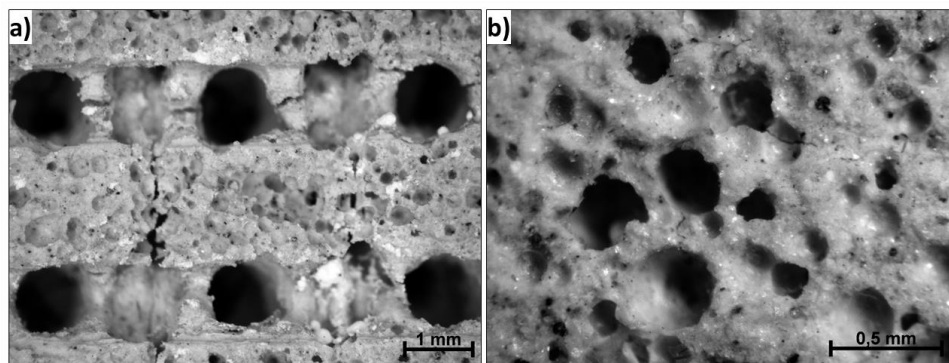


Fig. 2.10 -Image of a sample (with an architecture obtained by infiltration of the structure shown in Fig. 2.3(a)), in which the slurry contained oil and hydrogen peroxide. (a) general view; (b) detail at higher magnification [10].

Conclusions

Geopolymer components with controlled porosity were designed and produced by negative replica of PLA sacrificial templates with different patterns fabricated by FDM. A geopolymer slurry was used to produce accurate inverse replicas by impregnation in vacuum conditions and subsequent geopolymerization reaction; the template was successfully removed by a combined chemical and thermal treatment. The advantages of this process over geopolymer AM were that no careful optimization of the rheology of the ceramic slurry was necessary, and that drawbacks such as layer-by-layer inhomogeneous build up could be avoided. Geopolymer features were not affected by the processing, and the samples possessed highly interconnected macroscopic channels and micro- and meso-porosity in the struts, making them potentially attractive for filtering or catalyst support applications.

DIW with geopolymeric inks

Partially under publication in:

Franchin, G., Scanferla, P., Zeffiro, L., Elsayed, H., Baliello, A., Giacomello, G., Pasetto, M., Colombo, P.: Direct Ink Writing with Geopolymeric Inks. J. Eur. Ceram. Soc. 2017 (accepted 19/01/2017)

The goal of this section was to develop geopolymeric inks for DIW. It was a particularly challenging task, because the inks were subjected to ongoing (polycondensation/geopolymerization) reactions which continuously modified their rheological properties over time. Time has been involved as the 4th dimension in so-called 4D printing technologies with the aim of producing objects able to change their configuration or function depending on external stimuli [21–23]; geopolymeric slurries could be good candidates as smart materials for 4D printing once their reaction over time could be effectively controlled.

Materials and methods

Ink preparation

Four geopolymer mixtures were investigated, all comprising: metakaolin (Argical 1200S, Imerys S.A., Paris, FR) as source of alumino-silicate building blocks; a soluble sodium silicate solution (SS2942, Ingessil S.r.l., Montorio, IT); sodium hydroxide NaOH (Ika Werke GmbH & Co. KG, Staufen im Breisgau, DE); distilled water. The composition of the metakaolin and of the sodium silicate solution are summarized in Table 2.4.

Table 2.4 - Composition of the metakaolin and of the silicate solution in use

Reagent	SiO ₂ (wt%)	Al ₂ O ₃ (wt%)	Na ₂ O (wt%)	H ₂ O (wt%)
Argical 1200 S	55	39	<1	/
SS 2942	28.35	/	9.77	61.88

First, a solution of sodium silicate, sodium hydroxide and water was prepared with the following molar ratios: Na₂O/SiO₂ = 0.709, H₂O/Na₂O = 13. The solution was prepared at least 24 hours in advance and was stored at 4 °C; its composition is summarized in Table 2.5.

All ink formulations had the following molar ratios: Na₂O/SiO₂ = 0.263; SiO₂/Al₂O₃ = 3.8; Na₂O/Al₂O₃ = 1. Concerning the content of water, the first ink had a molar ratio H₂O/Na₂O = 13.78. The second ink was derived from the first one with the addition of 7 wt% of poly(acrylic acid) sodium salt with an average molecular weight of 5100 g/mol (PAA, Sigma-Aldrich, St. Louis, MO)

as a rheology modifier. PAA is frequently used as a thickening agent in aqueous based systems as it creates an entanglement of polymer chains imparting a shear thinning behavior to the ink. The third ink possessed a decreased water content, with a molar ratio $H_2O/Na_2O = 13$.

The fourth ink derived from the third one with the addition of 5 wt% of poly(ethylenglycole) PEG with an average molecular weight of 1000 g/mol (Sigma-Aldrich, St. Louis, MO) with the same role as that of PAA. The four inks were labeled: GP 13.78, GP 13.78 PAA, GP 13 and GP 13 PAA respectively, and their formulation is summarized in Table 2.6. The density of the inks was calculated using the rule of mixture from the theoretical density of the individual raw materials.

For samples GP 13.78 PAA and GP 13 PEG, the additives were added to this solution under mechanical stirring at 500 rpm for 5 minutes at room temperature. Metakaolin powder was then added to the solution under mechanical stirring at 1000 rpm for 10 minutes at room temperature.

Table 2.5 - Chemical composition of the alkaline solution.

	SS 2942 (g)	NaOH (g)	H ₂ O (g)
Alkaline solution	400	56.64	53.56

Table 2.6 - Formulation of the different inks.

	Argical 1200S (g)	Alkaline solution (g)	H ₂ O (g)	PAA (g)	PEG (g)	Density (g/cm ³)
GP 13.78	32.26	50	1.84	/	/	1.75
GP 13.78 PAA	32.26	50	1.84	5.89	/	1.53
GP 13	32.26	50	/	/	/	1.78
GP 13 PEG	32.26	50	/	/	4.11	1.73

Rheological characterization

A rotational rheometer (MCR 302, Anton Paar, Graz, A) equipped with a 50 mm diameter plate-plate geometry was used, with a set temperature of 20°C and a gap of 1 mm. Since the rheological behavior is crucial for the DIW process, several experiments were conducted in order to fully characterize our mixtures. Specifically,

- 1) **Steady rate sweep:** shear rate increasing from 0.01 to 100 1/s;
- 2) **Dynamic strain sweep:** deformation varying from 0.001% to 100% or 200% with a frequency of 1 Hz;
- 3) **Dynamic frequency sweep:** frequency varying from 0.1 to 100 Hz with a deformation of 1%;

- 4) **Viscosity recovery**, in two steps: first, a shear rate of 1 s^{-1} for 60 s was applied, followed by the application of a controlled shear stress of 15 Pa for 120 s in order to measure the recovery of viscosity.

The shear rate needed to be high enough to overcome the initial yield stress of the ink; in the second stage, the shear stress needed to be lower than the yield stress to allow recovery. Values were chosen according to the results of the first two tests.

- 5) **Storage (G') and loss (G'') moduli recovery**, in two steps: in the first step, a strain of 10% with a frequency of 1 Hz was applied for 1 min; after that, a strain of 0.1% with a frequency of 1 Hz was applied and the recovery of G' and G'' over time was measured.
- 6) **Working time**: constant deformation of 0.01% with a frequency of 0.1 Hz over 1 hr.

The measurements were repeated at different time intervals in order to investigate the effect of the ongoing poly-condensation (geopolymerization) reactions on the ink properties.

Direct Ink Writing

After mixing, the ink was transferred into a plastic syringe, which served as a cartridge for direct ink writing. Each syringe can contain up to 30 mm^3 of ink. The cartridges were mounted on two different DIW systems: a cartesian one (Powerwasp Evo, Wasproject, Massa Lombarda, IT) equipped with a mechanical piston, and a Delta one (Delta Wasp 2040 Turbo, Wasproject, Massa Lombarda, IT) equipped with a pressurized vessel and an infinite screw for paste extrusion. Both devices were described in Chapter 1; no difference was detected between samples printed with one or the other.

The ink was extruded at room temperature through the tip of a tapered capillary nozzle (Nordson Italia S.p.a., Segrate, IT) to form a geopolymeric filament that was deposited onto a flexible polyimide substrate. The substrate was generally kept in air, but could also be immersed in a hydrophobic liquid (typically oil) to limit drying and clogging issues. Printing was carried out at ambient temperature.

The extrusion occurred at a predetermined flow rate and deposition speed. After patterning one layer, the nozzle was incrementally raised in the z-direction to generate the next layer. This process was repeated until the desired structure was formed. 3D periodic lattices composed of a simple tetragonal geometry, for example, could be assembled by patterning an array of parallel filaments in the x-y plane such that their orientation was orthogonal to the layers immediately above and below a given layer. Alternatively, the nozzle could be gradually raised in the z-direction as the print progresses to build objects in a spiral fashion. Solidification via geopolymerization occurred either at room temperature or by heating the printed component at relatively low temperatures ($< 60^\circ\text{C}$).

The samples produced for this work were printed through a nozzle with a diameter of 840 μm ; the layer height was set at 600 μm to provide a small overlap between the layers and therefore better adhesion.

Different geometries were printed: from single wall vase-like structures for proof of concept and process validation through tetragonal lattices for characterization, to more complex porous structures for filtration purposes.

Physical and mechanical characterization

The morphology of the scaffolds was investigated by an optical stereoscope (STEMI 2000-C, Carl Zeiss AG, Oberkochen, DE). The designed porosity of the CAD file was calculated as the ratio between the volume occupied by the struts (modeled as dense elliptical cylinders) and the volume of the rectangular prism encapsulating the object. The porosity of the struts was evaluated by image analysis of SEM images using Fiji software[24]. The true density of powdered geopolymers after reaction was measured by means of a helium pycnometer (Micromeritics AccuPyc 1330, Norcross, GA). The total porosity of the lattices was therefore calculated as the ratio between their bulk and true density.

The compressive strength of the samples was measured with a Instron 1121 UTM (Instron Danvers, MA) with a cross head speed of 1 mm/min; at least five samples were tested for each geometry. After trimming of the edges, samples had a size of 20 x 20 x 7.2 mm³, corresponding to 12 superimposed layers.

Results and discussion

Rheological properties of the inks

Geopolymeric network formation via polycondensation of silicate and aluminate groups proceeds through the formation of oligomers, which in the initial stages of reaction are likely to behave as a weak gel structure.

A previous study on metakaolin-based geopolymer mixtures compared them with suspensions of plate-like clay particles in aqueous solutions, demonstrating that they possessed a weak shear thinning behavior with an initial yield stress [25].

The shear thinning character decreased with increasing solid content and could also reach Newtonian and shear thickening behavior. A higher amount of solid also increased the initial yield stress and the apparent viscosity of the mixtures.

A Bingham pseudoplastic behavior, i.e. shear thinning with initial yield stress, was also found in fly ash based geopolymer slurries [26].

The first objective of this rheological characterization was therefore to validate such hypothesis; if needed, the Bingham shear thinning behavior could be either forced or enhanced by the addition of organic polymers as rheology modifiers.

Modeling the extrusion process as the flow of a viscous fluid through a tube, the shear rate applied to the ink can be estimated by Eq (1.4); in the experiments here presented, the estimated shear rate was between 50 and 100 1/s.

Fig. 2.11(a, b) shows the flow and viscosity curves of the four inks, plotting the shear stress τ (Pa) and the viscosity η (Pa·s) against the shear rate $\dot{\gamma}$ (1/s). All tests were performed 2 min after the end of the mixing stage. Unfortunately the inks, GP 13 PEG in particular, lacked in adhesion to the rheometer plates and tended to be expelled from the side even at very low shear rates (1-2 1/s); therefore, just short segments of the flow and viscosity curves could be measured which did not represent the printing window, but were significant in determining the behavior of the inks.

Shear thinning behavior was confirmed for pure geopolymer mixtures GP 13.78 and GP 13, as an initial decrease in the viscosity values was detected at low shear rates; nevertheless, at shear rates of ~ 10 1/s their viscosities had already reached a plateau of ~ 20 Pa·s and ~ 30 Pa·s respectively. The rapid destruction of freshly formed alumino-silicate bonds due to the increasing stress is likely responsible of such behavior. Sample GP 13.78 PAA had higher yield stress and viscosity values; the slope of the flow curve decreased with the increasing shear rate also at higher values, testifying a more significant shear thinning behavior. Sample GP 13 PEG possessed an even higher yield stress and viscosity in comparison to the previous one, possibly also due to its lower water content.

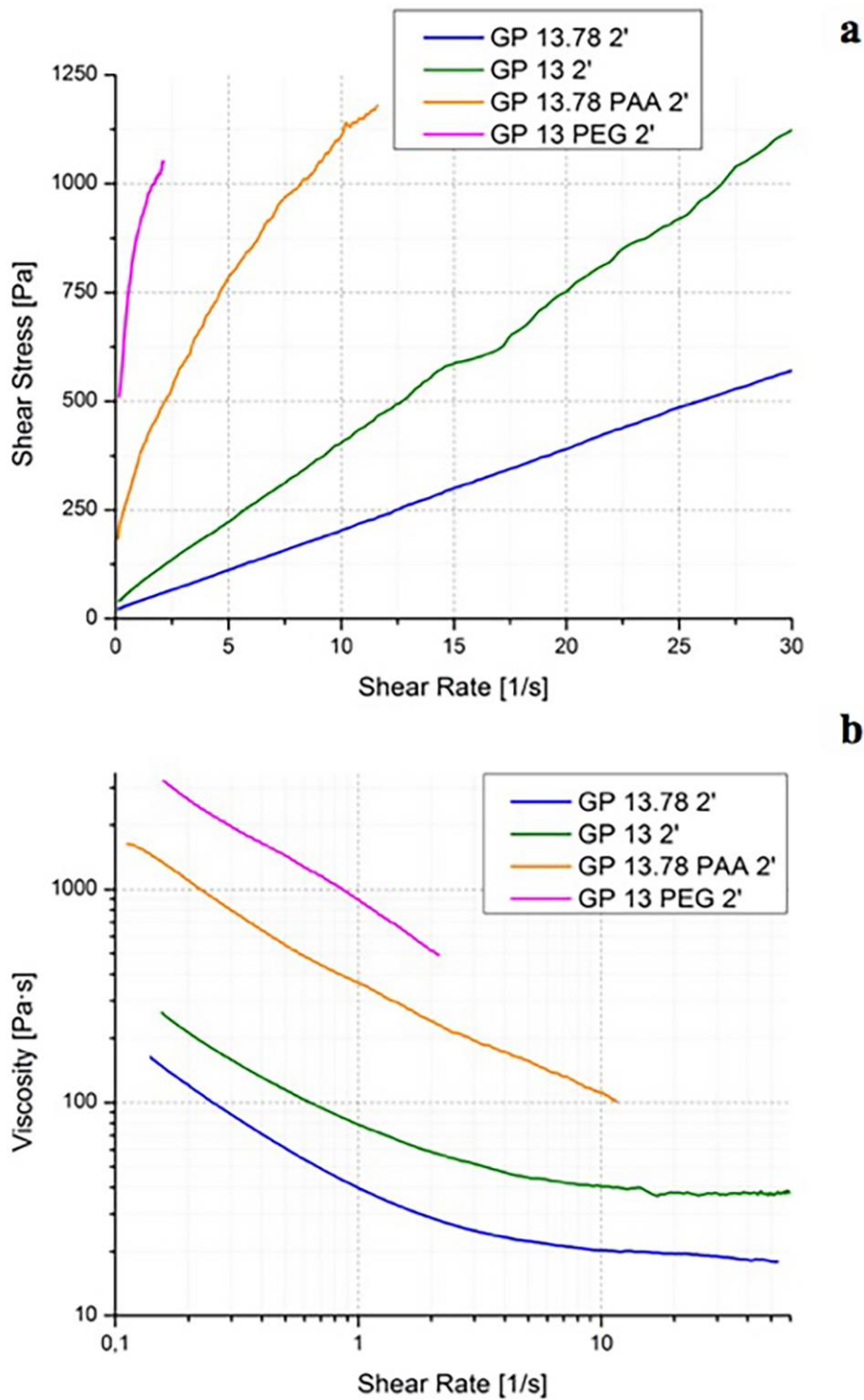


Fig. 2.11 – Steady rate sweep test performed on the four inks: (a) flow curves and (b) viscosity curves, 2 min after mixing.

Dynamic oscillation tests allowed to assess whether the inks had a transition to low rigidity systems at higher shear stress values. Measuring in oscillatory mode allowed to partially overcome the adhesion issues previously mentioned.

Fig. 2.12(a) shows a log–log plot of the storage moduli G' (Pa) and loss moduli G'' (Pa) of the inks after 5 min from the mixing stage as a function of the strain γ (%). All materials followed a similar trend:

- 1) at low to intermediate strain, both G' and G'' increased with the strain, with $G' > G''$;
- 2) at high strain, both G' and G'' decreased rapidly and intersected; to this stage corresponded a variation in slope for the shear stress (see Fig. 2.12(b)).
- 3) after that, their values stabilized again.

This behavior could be classified as type IV in the LAOS system, and could be explained if a reversible gel nature was assumed: the geopolymer network in formation was responsible of the elastic component, but the microstructural arrangement of the material could still be gradually destroyed by stresses above the yield stress, allowing the flow. Since these curves did not have a clear transition point, the values of yield stress were determined at the intersection between the G' and G'' curves. This method resulted in lower values for τ_y compared to different criteria applied in literature (i.e. that τ_y corresponded to the τ value for which $G' = 0.9 G'_{(eq)}$), thus being more conservative [27].

For pure geopolymer inks GP 13.78 and GP 13, G' and G'' showed rather low values and there was just a slight difference between them; the yield stress set to low values as well. The lower amount of water in the second ink caused a slight translation of G' , G'' and τ to higher values. In GP 13.78 PAA and GP 13 PEG inks, the Bingham shear thinning behavior was purposely enhanced to produce inks more suitable for DIW and able to retain the shape of the filament once extruded, even in case of suspended parts. G' and G'' differentiated more and showed higher values in the first segment, and so did the yield stress. The highest value reached by G' as well as the yield stress for each ink are reported in Table 2.7.

Table 2.7 - Maximum G' values and yield stress values from the dynamic strain sweep test performed on the four inks.

	GP 13.78	GP 13.78 PAA	GP 13	GP 13 PEG
τ_y (Pa)	1.5	20	2.5	80
G'_{max} (Pa)	500	10800	1500	67200
G'_{Smay} (Pa)	390	341	397	385

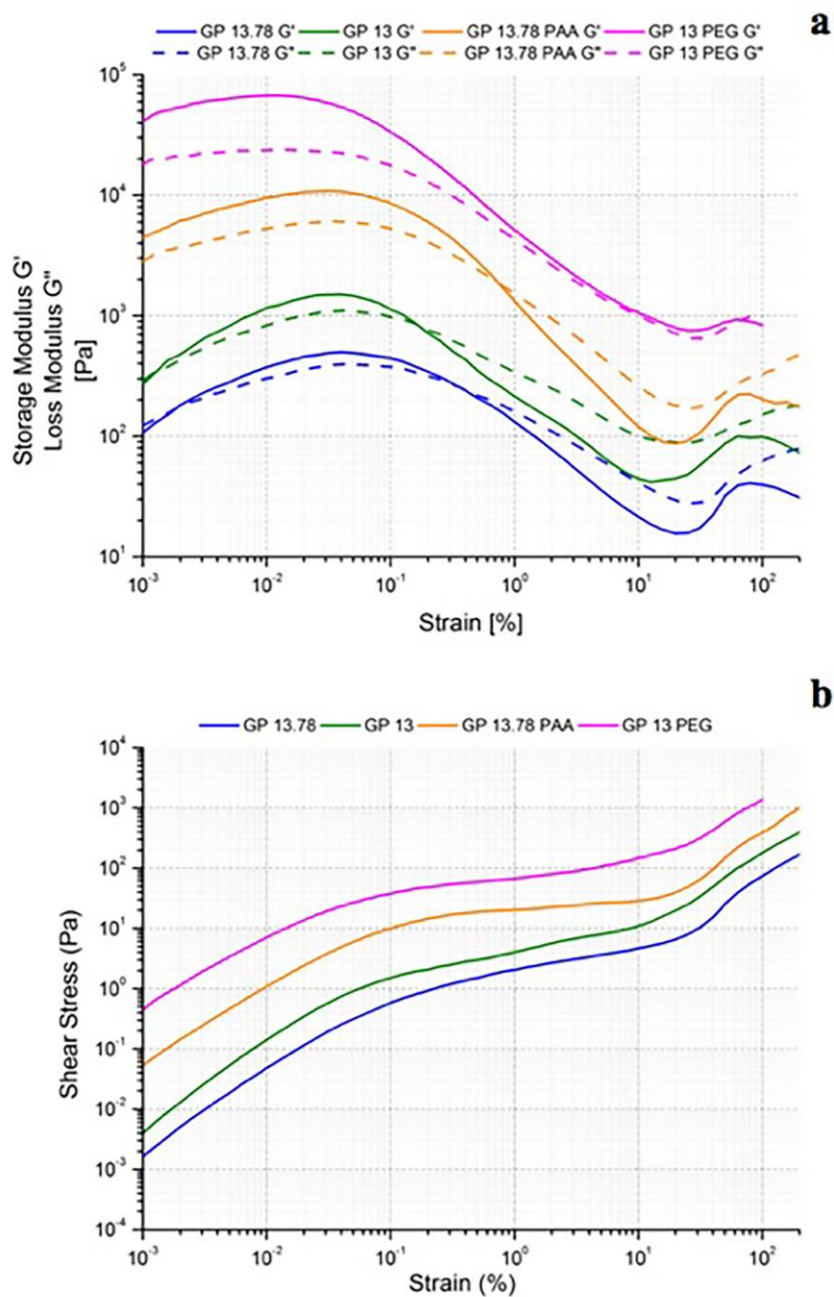


Fig. 2.12 - Dynamic strain sweep test performed on the four inks, 5 min after mixing: (a) G' and G'' moduli and (b) shear stress are plotted over strain.

The condition on G' which allowed minimal deflection, formulated by Smay et al. and reported in Eq. (1.1), was calculated for the four inks; note that in this case the printing process was performed in air instead of oil bath. The diameter of the filament was set at 800 μm and the spanning length at 2.4 mm (the biggest spacing that was used to fabricate samples for mechanical testing); values are reported in Table 2.7.

Based on the results, all inks could potentially be employed for DIW of geopolymeric lattices with such unsupported features; however, the two pure geopolymeric inks GP 13.78 and GP 13 are close to their limit; a low content of additive increased the gap dramatically and would allow for much bigger unsupported struts

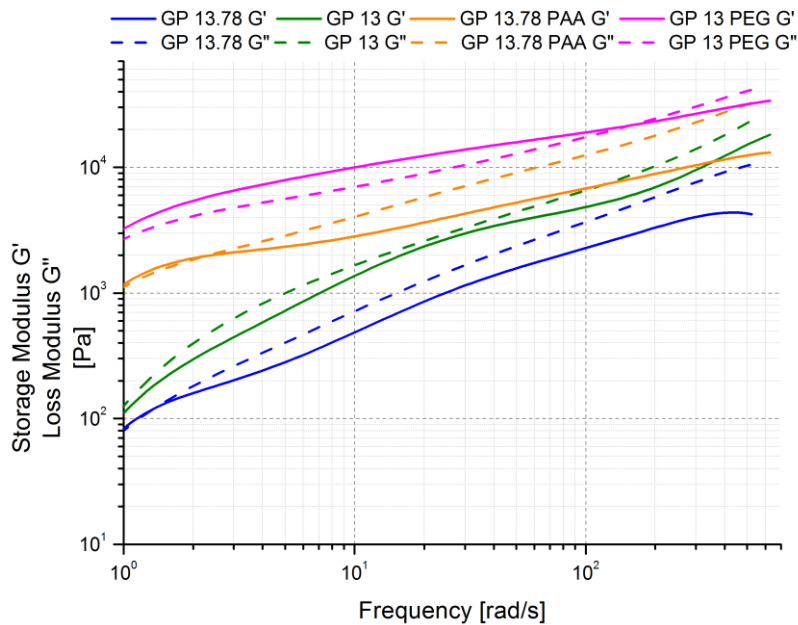


Fig. 2.13 - Dynamic frequency sweep test performed on the four inks.

It has to be mentioned that the strain sweep test alone cannot guarantee that the inks possess the structure of a (reversible) gel material; therefore, in order to further validate our theory and acquire more information, frequency sweep tests were conducted. Fig. 2.13 reports the values for G' and G'' for the four inks after 5 min from the mixing stage; if we compare the resulting curve with typical results for polymers and gels, we observe that in the frequency range all inks seemed to be beyond the crossover point, with G' and G'' increasing slightly over a wide frequency range [28]. This could be caused by a weakly crosslinked structure such as that occurring in a soft gel or a weakly bonded dispersion, but also by a wide molecular weight distribution of the uncross-linked geopolymer chains. In any case, the two tests together confirmed the typical gel behavior for the geopolymer inks. Note that inks GP 13.78, GP 13 and GP 13.78 PAA were all beyond the transition region, in the so called glassy region. For ink GP 13.78 PAA, the transition region could be detected at ~ 0.3 Hz. Ink GP 13 PEG, on the other hand, was in the rubbery plateau with $G' > G''$ up to ~ 20 Hz; this made it so far the most indicated material for extrusion processes such as DIW [28].

The most important feature of an ideal ink for direct ink writing is the ability to retain the shape after each filament is deposited, which corresponds to a quick viscosity recovery with no shear stress applied.

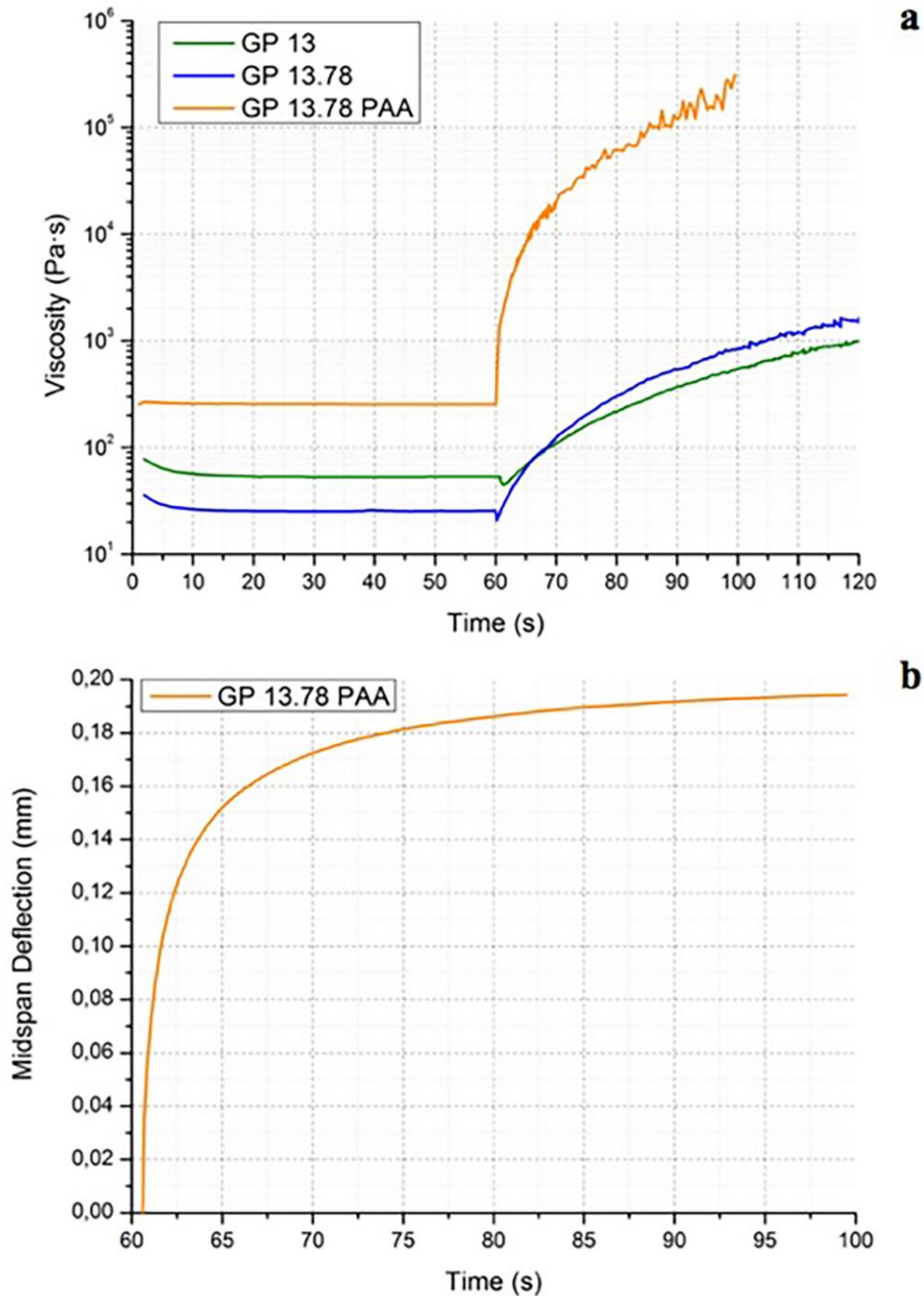


Fig. 2.14 – (a) Viscosity recovery test performed on Gp 13.78, GP 13 and GP 13.78 PAA inks; (b) Midspan deflection calculated for GP 13.78 PAA ink for a 2.4 mm spanning length.

Fig. 2.14(a) shows the result of the viscosity recovery test conducted on three out of the four inks; due to the aforementioned adhesion issues, it was not possible to apply a shear rate high enough to break the gel network in GP 13 PEG.

Pure geopolymeric inks GP 13.78 and GP 13 showed a viscosity increase after the first step, but the viscosity recovery required a long time (20 – 30 s for an increase of one order of magnitude) and did not reach sufficient values.

Although the viscosity of GP 13.78 PAA started from a higher value (~one order of magnitude), its recovery in the second step was way faster. The viscosity increased by two orders of magnitude in the first ~10 s, reaching a plateau value. This result confirms that the slurry had an appropriate rheology for DIW, as the increase of viscosity (increase in rigidity of the system) occurs in a very short period of time, therefore reducing the deformation of the printed, unsupported structures of the scaffold.

The deflection profile in the middle of the filament was calculated according to Schlordt et al. model (see Eq. (1.2)) and is reported in Fig. 2.14(b) [29]. The shape of the curve resembled that of the recovery test. This finding indicated that the filaments deformed in the first few seconds immediately after coming out of the extrusion nozzle, but the viscosity of the inks quickly increased and therefore also the deformation tended to reach a plateau value, because further deformation was completely hindered by the increase of viscosity. For a spanning distance of 2.4 mm, the final calculated deflection was ~0.19 mm, which confirms that the desired geometry can be printed accurately using this ink.

The midspan deflection for the same spanning distance, calculated for GP 13 and GP 13.78, was of ~9 mm; this value could not be real (as the spanning height of the structures was > 1 mm), but confirmed that a structure printed with these inks would collapse and not retain its shape.

In order to evaluate GP 13 PEG behavior, similar tests were conducted in oscillatory mode, thus recording G' and G'' instead of viscosity. The sudden change in the applied strain led to highly scattered data; therefore, fitted trends are reported in Fig. 2.15).

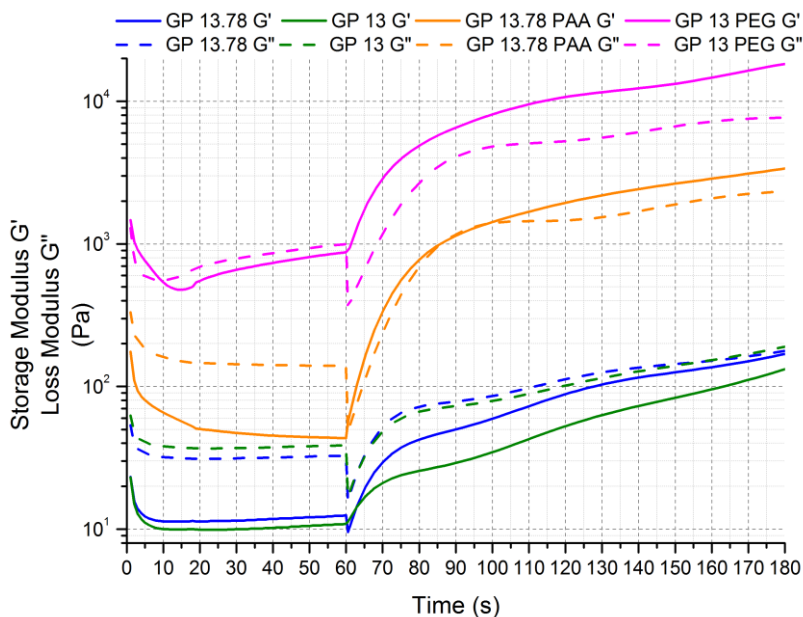


Fig. 2.15 - G' and G'' recovery test performed on the four inks.

The inks behavior resembled what observed for the viscosity recovery: pure geopolymer inks GP 13.78 and GP 13 showed only a moderate recovery of G' and G'' moduli and required a long time. GP 13.78 PAA started from higher values of G' and G'' (also in accordance with frequency sweep curves), yet still compatible with the extrusion process; once the shear stress was not applied anymore, G' increased by one order of magnitude in the first 15 s. It was not possible to completely break the GP 13 PEG gel phase in the initial stage (and again it was not possible to apply a higher strain due to the poor adhesion to the plates). However, G' increased significantly, from ~ 900 Pa to ~ 5000 Pa in the first 20 s of the second phase; G' also overcame G'' in the second stage, whereas for the other inks it remained lower or at the same value. This finding suggested that the latter ink possessed higher elasticity after extrusion and therefore more keen on retaining the shape with minimal deflection. Comparing these trends with the viscosity recovery ones, a very low midspan deflection could be expected from ink GP 13 PEG, even if its calculus was not possible. The two tests seemed to suggest a higher recovery for inks with higher water content, a phenomenon not yet understood.

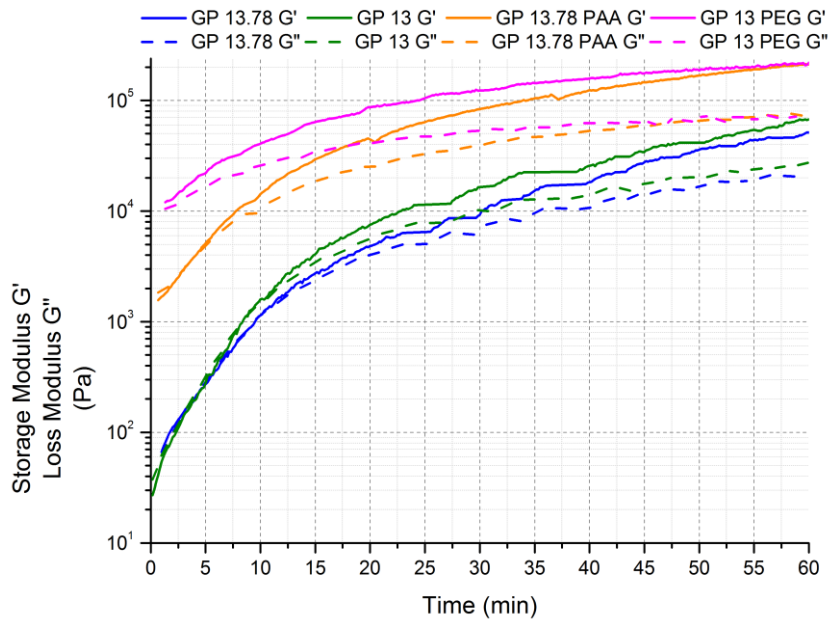


Fig. 2.16 - G' and G'' moduli behavior over time in the four inks.

Finally, the progression of the geopolymerization over time was investigated together with its effect on the rheological properties of the inks (Fig. 2.16). The measurements were perturbed by external movements happening around the instrument as they required a relatively long time and were conducted with a very low strain.

The higher amount of water present in ink GP 13.78 was responsible for a slight decrease of the G' and G'' curves with respect to those for sample GP 13; the curve trends, however, were equivalent. Ink GP 13.78 PAA possessed higher G' and G'' values from the start, but the presence of the additive seemed to decrease its reactivity; in fact, G' and G'' values grew at a slower rate. The retarding effect of the additives on the inks was confirmed and extremely significant in ink GP 13 PEG; G' and G'' modules started from higher values but grew at a much slower rate, to the point that they superimposed the values for sample GP 13.78 PAA by the end of the test. Possible explanations of the retarding effect of the additives on the geopolymerization could be their steric hindering effect; their hydrophilic character and ability to absorb water, which could lead to a shielding of the $-OH$ groups in the metakaolin, and impede water and ion diffusion necessary for its depolymerization.

The wider plateau detected in the latter case made again GP 13 PEG the best option for printing for longer times without having to significantly vary the process parameters.

GP 13 PEG was therefore chosen as printing ink and employed for the fabrication of geopolymeric components – both dense parts and lattices.

Experimentally, it was found that the ink could be printed for ~1.5 to 2 hours after mixing before it became too viscous. This limit obviously depended from the equipment in use (for which no viscosity threshold was provided by the company). However, it was observed that extruding the ink at an advanced stage of reaction would result in a clumpy, disrupted filament which would not further react. The same behavior was observed by mechanically mixing geopolymeric slurries at different times, and suggested that breaking the geopolymeric network in advanced stage of formation would not be reversible.

Production and characterization of porous lattices

After optimization of the models, based on suitable a computer-aided design (CAD) software, the selected ink (GP 13 PEG) was used to fabricate objects and lattices with unsupported features; a feed rate of ~10 mm/s was set and the flow rate was adjusted accordingly.

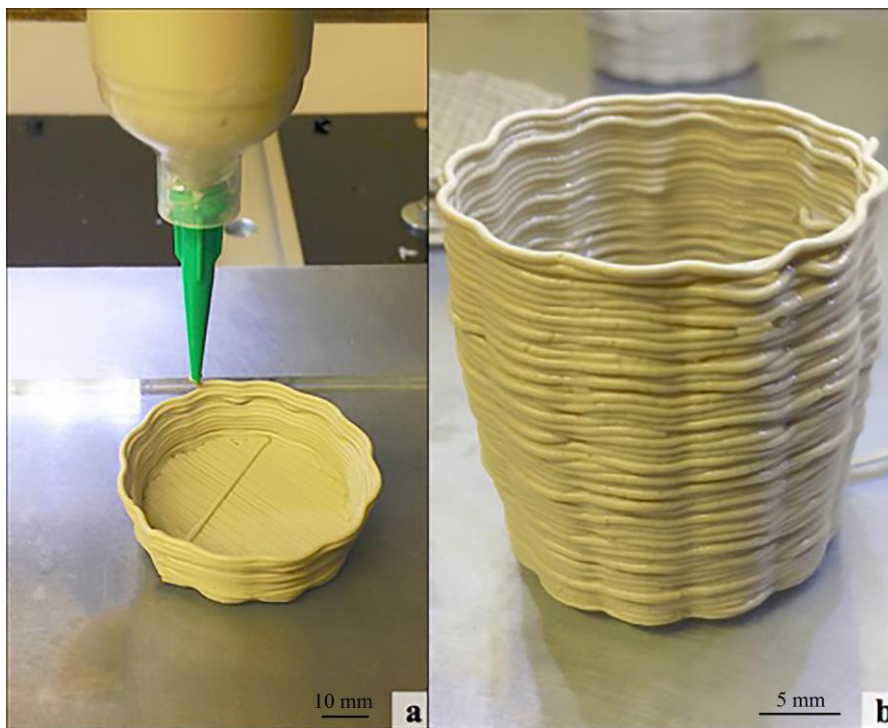


Fig. 2.17 - Printing process and printed single wall vase.

Fig. 2.17 shows the printing process and some examples of the printed structures. To validate the ability of the ink in terms of shape retention, a graded lattice with increasing spacing between subsequent struts was designed (see Fig. 2.18); the unsupported length increased from 1.5 mm to 4 mm with a 0.5 mm step.

The filaments showed very limited sagging and deformation, and the side pores remained open even with a spanning length of 4 mm, which confirmed that the rheological properties of the ink were suitable for printing such porous geometry.

Image analysis on geopolymerized structures gave an average strut diameter of 0.738 ± 0.024 mm. For a designed spacing of 2 mm, the distance between the center of two struts was of 1.802 ± 0.031 mm. Comparing these values with the nozzle diameter and the designed spacing resulted in a linear shrinkage of $\sim 10\%$. The filaments sagged by 0.050 ± 0.015 mm, which corresponds to less than 7% of their measured diameter, and this result can be considered very successful.

Note that the filaments retained a circular section and the overlap between the filaments, resulting from the set layer height, was of 0.143 ± 0.028 mm, corresponding to $\sim 20\%$ of the filament diameter. The purpose of it was to provide a stronger adhesion between the layers, which appeared optimal.

No cracks or surface defects were visible in the samples. The pores visible in the struts were probably due to water and PEG evacuation during the consolidation of the geopolymer or to air entrapped during the preparation of the ink.

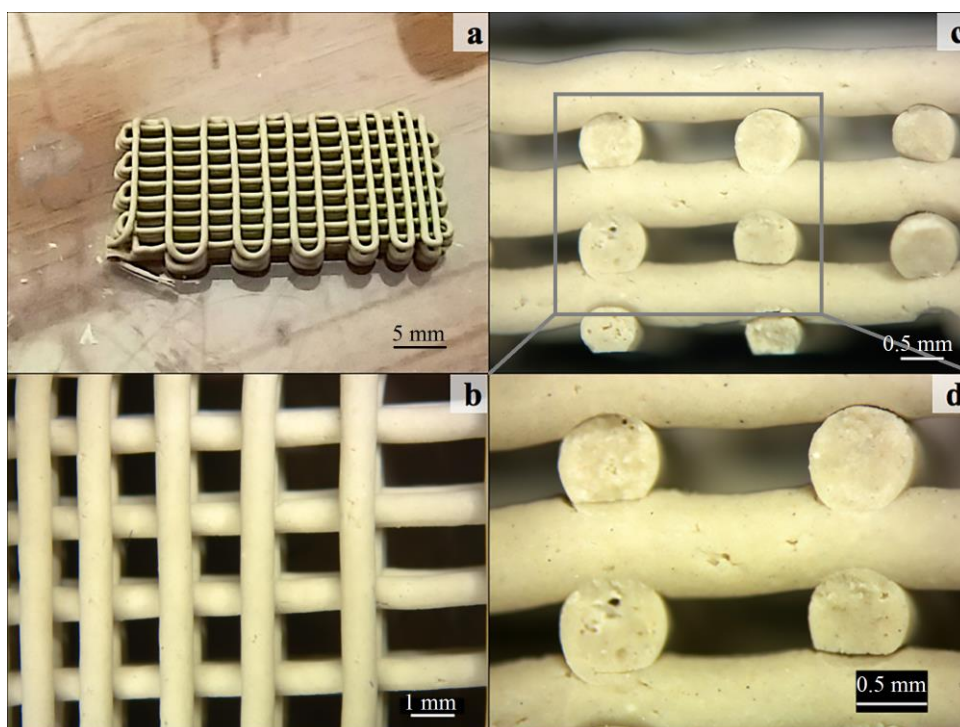


Fig. 2.18 - . Lattice with a gradient in spacing: (a) overview, (b) top view (mark is 1 mm), (c) and (d) side views (marks are 0.5 mm).

Lattices for mechanical testing were produced with different filament spacing, to evaluate the effect of total porosity on the compressive strength.

All of them were designed as tetragonal lattices with orthogonal layers of 0.8 mm wide parallel struts. The spanning distance between the struts was set at 1.2 mm, 1.6 mm and 2.4 mm, corresponding to a designed porosity of 46.59%, 59.16% and 71.73% respectively. The different structures are shown in Fig. 2.19(a). The total porosity of the lattices and their compressive strength is summarized in Table 2.8 and plotted in Fig. 2.19(b).

Table 2.8 - Porosity and compressive strength of different types of lattices

	Designed porosity (vol%)	Total porosity (vol%)	Compressive strength (MPa)
1.2 mm	46.59	49.81 ± 1.98	11.5 ± 1.9
1.6 mm	59.16	59.38 ± 1.56	4.7 ± 1.5
2.4 mm	71.73	71.27 ± 0.75	2.0 ± 0.5

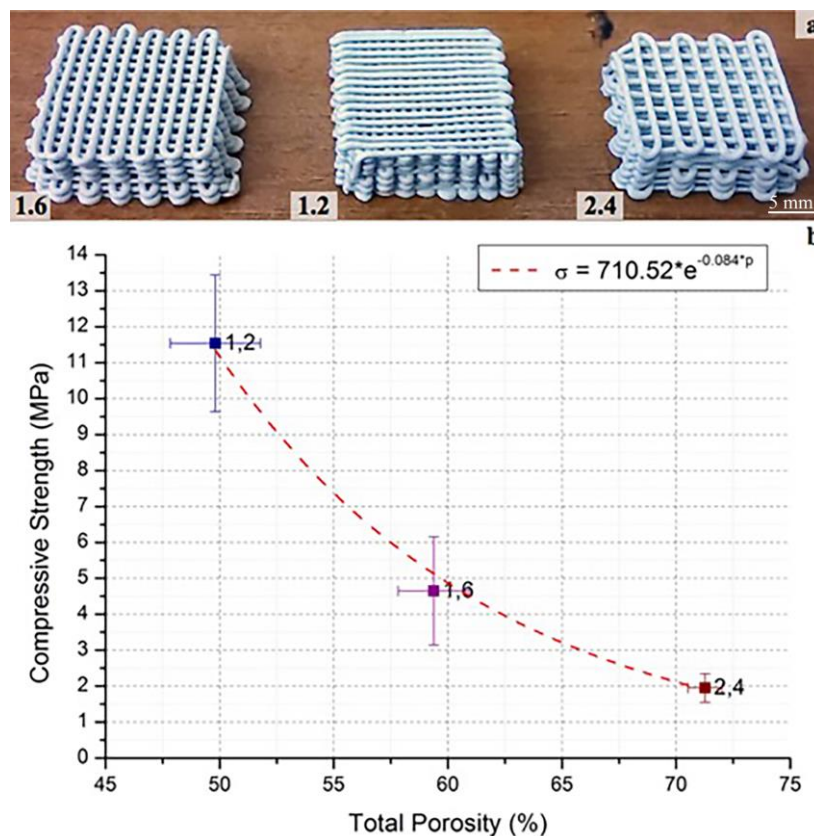


Fig. 2.19 - (a) Lattices with (I) 1.6 mm, (II) 1.2 mm and (III) 2.4 mm spanning distance; (b) compressive strength vs porosity plot for the three types of lattices.

The measured porosity was consistent or just slightly higher (for lattices with 0.8 mm spanning distance) than the designed one. The differences were due to two contrasting contributions: the slight overlap between the layers on one side and the porosity present in the struts on the other side. As expected, there was a clear correlation between the porosity of the printed lattices and their mechanical properties.

Lattices with ~49.8 vol% porosity possessed a compressive strength of ~11.5 MPa, which decreased to ~4.7 MPa for ~59.4 vol% and to ~2.0 MPa for ~71.3 vol%. Data were fitted according to Ryshkewitch exponential model [30]:

$$\sigma = A \cdot e^{-B \cdot p} \quad (2.1)$$

where σ (MPa) is the compressive strength, p (vol%) is the total porosity of the samples and A , B are experimental parameters and were found to be $A = 710.52$ MPa and $B = 0.084$ with a correlation factor $R^2 = 0.991$. There seemed to be a good accordance between data and fitting.

There is no reference in literature of geopolymeric lattices with similar porosity for a comparison. Geopolymeric foams produced by combined saponification/peroxide technique had a compressive strength of 2.38 ± 0.47 MPa at 70.3 ± 1.3 vol% total porosity, similar to what obtained for lattices with a spanning distance of 2.4 mm [5]; varying the amount of oil and peroxide, a compressive strength of 8.83 ± 2.38 MPa at $72.6 \pm$ vol% total porosity and up to 25.96 ± 5.12 MPa at 62.0 ± 0.5 vol% total porosity were achieved in the same work. Although these values are much higher than what achieved by the printed lattices, it should also be noted that they refer to pores 10 to 50 times smaller.

Case study

Although the focus of this work was on one specific geopolymer formulation, other proofs of concept are here reported which can testify the versatility and the opportunities afforded by the combination of material and process.

One of the key features of geopolymer materials is their environmental sustainability, as they can be produced starting from waste materials, i.e. fly ashes and slags from the foundry industries.

An ink based on class F fly ashes (#200 mesh; Tractebel Energia, Florianapolis, BR) with average composition reported in Table 2.2 was developed. The negative charge of the aluminate groups can be effectively balanced by potassium ions, some amount of which is already present as K_2O in the fly ashes; therefore, sodium silicate and hydroxide were replaced by potassium silicate (KSIL 0465, Crosfield Italia Srl, Montorio, IT) and hydroxide (Ika Werke GmbH & Co. KG, Staufen im Breisgau, DE) respectively. The formulation employed previously for the negative replica of 3D printed PLA lattices was adapted [10]; Na lignosulfonate (Sigma-Aldrich, St. Louis, MO) was used as retarder with a concentration of 0.6 wt% and PAA was used as gelling agent with a concentration of 6 wt%.

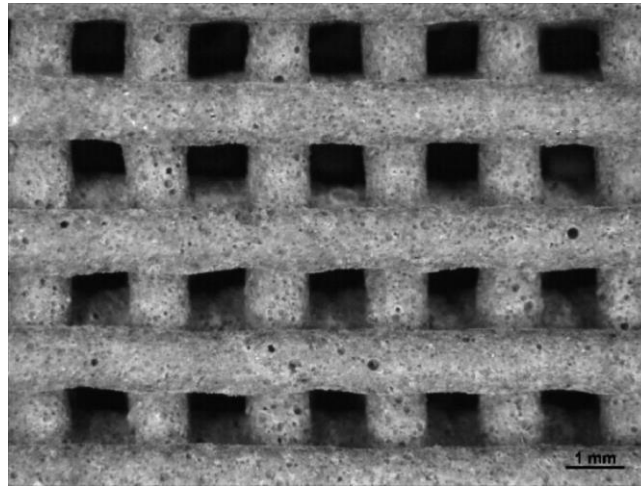


Fig. 2.20 - GP lattice from fly ashes and K.

A different printing medium was investigated, i.e. sunflower oil instead of air; the oil provided more support to the spanning structures and therefore limited sagging. Lattices printed with the same nozzle and 2 mm spacing were successfully printed (see Fig. 2.20). The choice of printing in oil had the double goal of providing slower water evaporation and support to the spanning struts, and producing more porous, lighter components; in fact, the oil reacted with KOH via the saponification route employed for foam fabrication [4].

Conclusions

Geopolymer inks with optimized rheological properties for DIW were successfully developed; several inks with different water content and different kind and amount of additives were compared and the best formulation was selected, i.e. GP 13 PEG. The ink possessed a Bingham shear thinning behavior which enabled the extrusion as well as the retention of the produced shape even in the case of unsupported struts.

Highly porous ceramic components (porosity up to ~71 vol%) with features of ~0.8 mm and unsupported parts with very limited sagging (less than 7% of the struts diameter) were produced and characterized; their mechanical properties were investigated and correlated with their porosity.

Finally, our approach was successfully extended to other formulations, such as fly ash and potassium based geopolymer slurries. Tailoring of the porosity was also possible by taking advantage of saponification in oil. Such ceramic lattices could be suitable for many applications, including air and water filtration, lightweight structures and so on.

Future work would be focused on solving the issues which currently limit the industrialization of the process, i.e. the limited working time window, the use of highly alkaline solutions, the strong dependence of the inks from the environmental conditions: in fact, temperature and humidity have a strong influence on the ink rheology and reactivity.

References

- [1] J. Davidovits, *Geopolymer - Chemistry and applications*, 3rd ed., Institut Geopolymere, 2011.
- [2] J.L. Provis, J.S.J. van Deventer, *Geopolymers. Structures, Processing, Properties and Industrial Applications*, 2009. doi:10.1533/9781845696382.
- [3] J. Davidovits, *Geopolymers based on natural and synthetic metakaolin - A critical review*, 2 (2016).
- [4] M.S. Cilla, M.R. Morelli, P. Colombo, Open cell geopolymer foams by a novel saponification/peroxide/gelcasting combined route, *J. Eur. Ceram. Soc.* 34 (2014) 3133–3137. doi:10.1016/j.jeurceramsoc.2014.04.001.
- [5] C. Bai, G. Franchin, H. Elsayed, A. Conte, P. Colombo, High strength metakaolin-based geopolymer foams with variable macroporous structure, *J. Eur. Ceram. Soc.* 36 (2016) 4243–4249. doi:10.1016/j.jeurceramsoc.2016.06.045.
- [6] R.M. Novais, L.H. Buruberri, M.P. Seabra, J.A. Labrincha, Novel porous fly-ash containing geopolymer monoliths for lead adsorption from wastewaters, *J. Hazard. Mater.* 318 (2016) 631–640. doi:10.1016/j.jhazmat.2016.07.059.
- [7] M. Xia, J. Sanjayan, Method of formulating geopolymer for 3D printing for construction applications, *Mater. Des.* 110 (2016) 382–390. doi:10.1016/j.matdes.2016.07.136.
- [8] Geobeton 3D, (n.d.). <http://geobeton.ru/en/product/geopolimer/?v=cd32106bcb6d> (accessed October 14, 2016).
- [9] R. Ciapponi, V. Fausti, M. Tonizzo, *Losing the Edge*, (n.d.). www.piulab.it/single-post/2016/06/14/Losing-The-Edge (accessed October 14, 2016).
- [10] G. Franchin, P. Colombo, Porous Geopolymer Components through Inverse Replica of 3D Printed Sacrificial Templates, *J. Ceram. Sci. Technol.* 6 (2015) 105–112. doi:10.4416/JCST2014-00057.
- [11] V.J. Chen, L.A. Smith, P.X. Ma, Bone regeneration on computer-designed nano-fibrous scaffolds, *Biomaterials.* 27 (2006) 3973–3979. doi:10.1016/j.biomaterials.2006.02.043.
- [12] P. Coszach, J.-C. Bogaert, J. Willocq, Chemical recycling of PLA by hydrolysis, *US 8431683 B2*, 2013.
- [13] K. Okada, A. Imase, T. Isobe, A. Nakajima, Capillary rise properties of porous geopolymers prepared by an extrusion method using polylactic acid (PLA) fibers as the pore formers, *J. Eur. Ceram. Soc.* 31 (2011) 461–467. doi:10.1016/j.jeurceramsoc.2010.10.035.
- [14] M.C. Bignozzi, S. Manzi, I. Lancellotti, E. Kamseu, L. Barbieri, C. Leonelli, Mix-design and characterization of alkali activated materials based on metakaolin and ladle slag, *Appl. Clay*

Sci. 73 (2013) 78–85. doi:10.1016/j.clay.2012.09.015.

- [15] J.L. Bell, P.E. Driemeyer, W.M. Kriven, Formation of ceramics from metakaolin-based geopolymers. Part II: K-based geopolymer, *J. Am. Ceram. Soc.* 92 (2009) 607–615. doi:10.1111/j.1551-2916.2008.02922.x.
- [16] P. Duxson, G.C. Lukey, J.S.J. Van Deventer, Physical evolution of Na-geopolymer derived from metakaolin up to 1000 °C, *J. Mater. Sci.* 42 (2007) 3044–3054. doi:10.1007/s10853-006-0535-4.
- [17] L. Li, S. Wang, Z. Zhu, Geopolymeric adsorbents from fly ash for dye removal from aqueous solution, *J. Colloid Interface Sci.* 300 (2006) 52–59. doi:10.1016/j.jcis.2006.03.062.
- [18] T.W. Cheng, M.L. Lee, M.S. Ko, T.H. Ueng, S.F. Yang, The heavy metal adsorption characteristics on metakaolin-based geopolymer, *Appl. Clay Sci.* 56 (2012) 90–96. doi:10.1016/j.clay.2011.11.027.
- [19] D. MedPELLI, J.M. Seo, D.K. Seo, Geopolymer with hierarchically meso-/macroporous structures from reactive emulsion templating, *J. Am. Ceram. Soc.* 97 (2014) 70–73. doi:10.1111/jace.12724.
- [20] M. Strozi Cilla, M. Raymundo Morelli, P. Colombo, Effect of process parameters on the physical properties of porous geopolymers obtained by gelcasting, *Ceram. Int.* 40 (2014) 13585–13590. doi:10.1016/j.ceramint.2014.05.074.
- [21] J. Choi, O.-C. Kwon, W. Jo, H.J. Lee, M.-W. Moon, 4D Printing Technology: A Review, *3D Print. Addit. Manuf.* 2 (2015) 159–167. doi:10.1089/3dp.2015.0039.
- [22] S. Tibbits, 4D Printing, *Archit. Des.* 84 (2014) 116–121. doi:10.1002/ad.1710.
- [23] A. Sydney Gladman, E.A. Matsumoto, R.G. Nuzzo, L. Mahadevan, J.A. Lewis, Biomimetic 4D printing, *Nat. Mater.* 15 (2016) 413–8. doi:10.1038/nmat4544.
- [24] J. Schindelin, I. Arganda-Carreras, E. Frise, V. Kaynig, M. Longair, T. Pietzsch, S. Preibisch, C. Rueden, S. Saalfeld, B. Schmid, J.-Y. Tinevez, D.J. White, V. Hartenstein, K. Eliceiri, P. Tomancak, A. Cardona, Fiji: an open-source platform for biological-image analysis, *Nat. Methods.* 9 (2012) 676–682. doi:10.1038/nmeth.2019.
- [25] M. Romagnoli, C. Leonelli, E. Kamse, M. Lassinantti Gualtieri, Rheology of geopolymer by DOE approach, *Constr. Build. Mater.* 36 (2012) 251–258. doi:10.1016/j.conbuildmat.2012.04.122.
- [26] A. Palomo, P.F.G. Ban II, A. Fernández-Jiménez, D.S. Swift, Properties of alkali-activated y ashes determined from rheological measurements, *Adv. Cem. Res.* 17 (2005) 143–151. doi:10.1680/adcr.2005.17.4.143.
- [27] J.E. Smay, J. Cesarano, J.A. Lewis, Colloidal Inks for Directed Assembly of 3-D Periodic

Structures, *Langmuir*. 18 (2002) 5429–5437. doi:10.102/la0257135.

- [28] S. Goodyer, Measuring Polymers using a Rotational Rheometer in Oscillatory Mode Product Manager for Rheology, in: Telford Polym. Assoc., 2013: pp. 1–35.
- [29] T. Schlördt, F. Keppner, N. Travitzky, P. Greil, Robocasting of Alumina Lattice Truss Structures, *J. Ceram. Sci. Technol.* 3 (2012) 1–7. doi:10.4416/JCST2012-00003.
- [30] E. Ryshkewitch, Compression Strength of Porous Sintered Alumina and Zirconia, *J. Am. Ceram. Soc.* 36 (1953) 65–68. doi:10.1111/j.1151-2916.1953.tb12837.x.

3. Glass

Partially published in:

Klein, J., Stern, M., Franchin, G., Kayser, M., Inamura, C., Dave, S., Weaver, J. C., Houk, P., Colombo, P., Yang, M., and Oxman, N.: Additive Manufacturing of Optically Transparent Glass. 3D Printing and Additive Manufacturing 2015, 2 (3), 92-105 [1]

Silica-soda-lime glass represents ~90% of manufactured glass, as it is used for windowpanes, bottles and containers for food and beverages and other commodity items. It is particularly valuable due to its affordability, chemical stability, reasonable hardness, and obviously transparency.

Manufacturing of soda-lime glass and silicate glass in general is rather traditional: flat glass panels are formed by the Pilkington float glass process; while container glass for bottles and jars is formed by blowing and pressing techniques. Other, more complex parts, can be fabricated by glass molding, and artistic glass remains mostly hand-blown.

The extrusion of molten glass is applied in the artistic milieu as a traditional glass manufacturing practice, and glass artisans are able to produce glass canes or stringers through manual glass extrusion, ranging in diameter from fractions of a millimeter to several millimeters.[2] Large scale manufacturing processes have also been developed for glass extrusion. The application of pressure to force glass flow through a die extends the glass working range to higher viscosities, and enables the production of rods and tubes with complex sections but still simple shapes [3].

To date, research on AM of glass has been overall limited. The most common approach was binder jetting applied to glass powders, which overcame their high melting temperatures but led to components with very limited strength; moreover, they were opaque due to the light scattering from glass powders caused by incomplete densification by viscous sintering [4–6]. DIW was also investigated for the manufacturing of glass components, with particular interest in Bioglass® formulations for bone tissue engineering. As the green body embedding glass particles underwent sintering, however, it encountered the same limitations of binder jetted glass parts [7–9].



Fig. 3.1 - Attempts of AM with glass: powder-bed based approaches by (a) Klein, S. et al. and (b) ExOne; (c) wire fed SLM [5,6,10].

Even Selective Laser Melting (SLM) was not able to overcome this issue: products remained opaque and possessed poor mechanical properties [11]. In a more recent work, the researchers substituted the powder with a glass wire which is fed into a laser heated melt pool with a wire feeder [10]. Starting with a fully dense feedstock was shown to minimize the formation of trapped bubbles and pores and therefore to facilitate the fabrication of transparent components. Building of rectangular walls with a flat top profile and transparency equal to furnace cast pieces (after polishing) was reported, but the process still lacked in control and repeatability.

Very recently, Corning Inc. filed a patent for the production of transparent glass parts combining powder raw material (in a powder bed, slurry or paste form) and vacuum aided sintering of the green bodies [12]; examples of glass components fabricated according to this process have not yet been shown.

The goal of this chapter was to demonstrate, and report on an extrusion-based AM process using molten glass in order to produce optically transparent components. As no FDM or DIW device existed which was able to process glass at the high temperatures needed, a novel, fully functional 3D printer was designed and fabricated.

Materials and methods

Glass 3D Printer (G3DP)

The concept, the design and the construction of the glass 3D printer were carried out in house. The final assembly and its schematics are shown in Fig. 3.2.

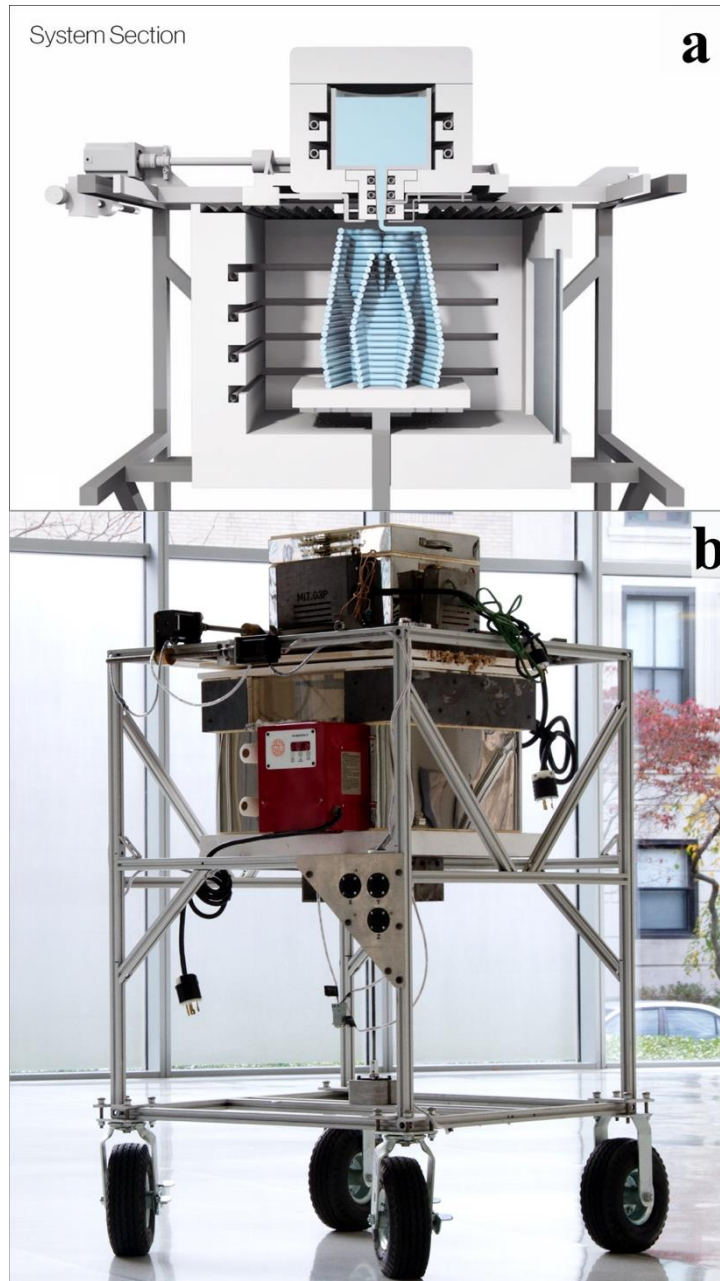


Fig. 3.2 - (a) Schematics of the printer (section) [1]; (b) Glass 3D Printer (G3DP; credits: Inamura, C.).

Each component of the system was designed as a modular unit, to allow quick and specific development of different features. The primary component of the system was a vertical assembly of the following three temperature control systems; a crucible kiln, a nozzle kiln, and an annealing kiln.

All kilns were made of refractory ceramics (alumina-silica fiberboard or refractory bricks) and provided resistive heating thanks to FeCrAl elements. Temperatures in each zone were monitored through thermocouples placed inside each kiln. The crucible kiln was responsible for glass melting and fining; glass was contained in a refractory crucible placed inside the crucible kiln. The crucible included a bottom hole where the nozzle was inserted; this was machined from alumina bisque rods and enabled the direct deposition of glass with precise control on layer height without introducing defects in the printed part. The nozzle kiln provided control over the flow of glass. Molten glass was deposited directly into the annealing kiln, which maintained the temperature above the glass transition temperature (T_g) during the process and performed the subsequent annealing cycle on the printed part. The annealing build chamber had fiberboard doors to provide access to the nozzle (for manual start and stop of the glass flow) and to the printed object, and a transparent ceramic (Neoceram[®]) window to monitor the print job. The three kilns assembly was supported by an external frame structure made of aluminum extrusions and steel plates.

A three axes linear provided motion control through a motion gantry system comprised of a stepper motor and a lead screw in each axis. X-Y control was achieved by driving the crucible kiln and nozzle kiln assembly on a mobile carriage; the Z motor mounted at the base of the frame controlled the mobile build platform inside the stationary annealing kiln.

CAD objects were defined in Rhinoceros 5.0 environment and described as a non-uniform rational basis spline (nurbs) surfaces. The surfaces were sliced into layers using a custom C# script in Grasshopper Build 0.9.76.0. The script drew a continuous helix around the model structure accommodating for the specific filament diameter of extruded glass. Layer height, curve discretization and printing rate could be modified; users could also define specific velocities for each point. The toolpath was then represented in Cartesian coordinates in the form of G-code and imported into the open source printing software Repetier-Host V1.0.6. Repetier firmware, adapted for accelerations, velocities and size of the build platform, was used to direct the printer.

Materials and process characterization

As the input glass source, commercial soda-lime glass nuggets (System 96[®] Studio Nuggets[™], Spectrum[®] Glass Company, Inc., Woodinville, WA) were placed in the crucible kiln. The crucible kiln could contain ~2kg of molten glass, which was frequently replenished during a print job to ensure that a roughly constant level of molten glass was maintained through the process. The glass composition was analyzed at Corning Inc. (Corning, NY) by means of X-ray Fluorescence (XRD). Corning also provided a value for the glass density. The glass transition temperature and its CTE were measured by means of a dilatometer (DSC 404, Netzsch Gerätebau GmbH, Selb, DE) with a heating rate of 10 °C/min.

Glass dynamic viscosity η strongly depends on temperature; its dependence can be modeled using the Vogel-Fulcher-Tammann (VFT) equation [13–15]:

$$\log \eta(T) = A + \frac{B}{T - T_0} \quad (3.1)$$

Where η [Pa·s] is the dynamic viscosity of the glass, T [°C] is its temperature, and A , B and T_0 are experimental values depending on the glass composition. Viscosity values were measured at different temperatures at Corning Inc. (Corning, NY) with proprietary equipment and fitted using the VFT equation to estimate A , B and T_0 .

Two types of glass frits were used to explore the incorporation of color into the printed objects, Reichenbach R-19 Gold Topaz, F0 frit (size < 1 mm), and R-11 Heliotrope, F2 frit (size 2-4 mm) (Farbglashütte Reichenbach GmbH, Reichenbach, DE).

The temperature distribution in the kiln cartridge was simulated using Solidworks[®] Flow Simulation Computational Fluid Dynamics (CFD) software. The crucible and nozzle were modeled as a three parts assembly: the crucible, the nozzle body and the nozzle tip (which was not heated and stuck out into the annealing chamber). The properties of a software-defined 96% alumina material were assigned to all parts. In a first approach (reported in the published work [1]) the system was simplified by setting the crucible and the nozzle body as volumetric heating elements. In the more refined iteration reported here, the heating was provided by the cylindrical enclosures in direct contact with the glass containers, resembling the crucible kiln (at 1040°C) and the nozzle kiln (at 1010°C). The ambient temperature was set at 480°C to simulate the printing chamber. Heat conduction followed the discrete transfer model, and the default outer wall thermal condition was driven by the heat transfer coefficient. The fluid properties were modeled based on the density and predicted viscosity with respect to temperature, and standard float silica soda lime glass was used as reference for the heat transfer coefficient and thermal conductivity. The crucible was considered to be completely filled with fluid, and the flow was driven by gravity.

Infrared images were acquired from the build chamber window during a printing process using a FLIR T335 equipped with a T197000 high temperature option, and analyzed using FLIR Tools software (FLIR® Systems, Inc., Cambridge, MA).

Parts fabrication and characterization

Glass nuggets were heated in the crucible to 1165 °C for 4 hours; the glass was then fined for additional 2 hours at the same temperature to eliminate bubbles. During this phase, the nozzle was kept at a lower temperature (T ~800 °C) to prevent glass flow. Alternatively, to accelerate the process, already molten glass from a furnace was directly loaded to the crucible. Next, the crucible and nozzle temperatures were set to 1040 °C and 1010 °C respectively, while the temperature of the annealing kiln was set to 480 °C. Once the set temperature was reached, glass started flowing due to gravity; however, the flow could be terminated at the end of each print by cooling the nozzle tip with compressed air, and reinitiated at the beginning of the following print by heating the nozzle tip with a propane torch. Once the printing process was completed, the crucible and nozzle were drained by increasing their temperature up to 1165 °C. The annealing cycle, as summarized in Table 3.1, was then carried out in the annealing kiln. For increased part production, objects were removed from the build chamber and placed in an external annealing kiln kept at 480 °C until the end of the printing session. Then, they were annealed following the same cycle. Post processing of the object for display and characterization included cutting, grinding and polishing.

Table 3.1 - Annealing cycle.

Cooling rate (°C/h)	T interval (°C)	Dwelling time (h)
-	480	1
25	480-400	-
50	400-150	-
50	150-80	-
120	80-20	-

Samples were imaged by means of micro Computer Tomography (microCT; XRA-002 X-Tek MicroCT, XTek Inc., Cincinnati, OH) system, and the 3D reconstruction was carried out using CT-Pro (Nikon Metrology Inc., Brighton, MI); generated surface renderings were performed using the open source image processing package Fiji [16]; Rhinoceros 5.0 was used to evaluate the objects' deviation from the CAD file.

Samples for characterization were obtained by printing and then cutting down rectangular prisms with a diamond saw. The cut surfaces were diamond ground and polished with cerium oxide. The samples were then sputter-coated with gold and imaged by means of scanning electron microscopy (Tescan Vega SEM, Tescan Orsay Holding, A.S., Brno-Kohoutovice, CZ and FESEM Zeiss Ultra 55, Carl Zeiss AG, Oberkochen, DE).

The samples were observed under a polariscope with tint plate (Model 243 6", PTC® Instruments, Los Angeles, CA) to determine residual stress patterns developed during glass cooling.

The flexural behavior of the glass bars was investigated using an Instron 8841 and an Instron 5500R (Illinois Tool Works Inc., Glenview, IL) equipped with a 3 points bending fixture. Tests were performed at a cross-head speed of 0.05 to 0.12 mm/min. A compliant layer (Scotch® Permanent Outdoor Mounting Tape, 3M, Saint Paul, MN) was used between the bottom fixtures and the sample surfaces in some orientations. Results are reported descriptively due to the limited number of samples examined.

Results and discussion

Materials and process characterization

Glass composition and properties are reported in Table 3.2 and Table 3.3.

Table 3.2 - Chemical composition (wt%) of the glass in use.

SiO₂	Na₂O	CaO	K₂O	Al₂O₃	ZnO	BaO	B₂O₃	Sb₂O₃	Other
70	16.23	5.43	0.53	1.8	1.01	2.4	1.99	0.24	> 0.1

Table 3.3 - Physical properties and characteristic points of the glass in use.

Density (g/cm ³)	CTE (1/K)	Strain point (°C)	T_g (°C)	Annealing point (°C)	Softening point (°C)	Working point (°C)
2.36	11 x 10 ⁻⁶	490	508	515	678	966

Experimental values of viscosity with respect to temperature are reported in Fig. 3.3; they led to the definition of the following values for A , B and T_0 in the VFT equation:

$$\log \eta(T) = -2.47 + \frac{3962.7}{T - 241.5} \quad (3.2)$$

The equation enabled the prediction of glass viscosity at each temperature and thus the estimation of thermal response of glass and process tailoring. The fitting was very accurate with a correlation coefficient $R^2 = 0.99997$.

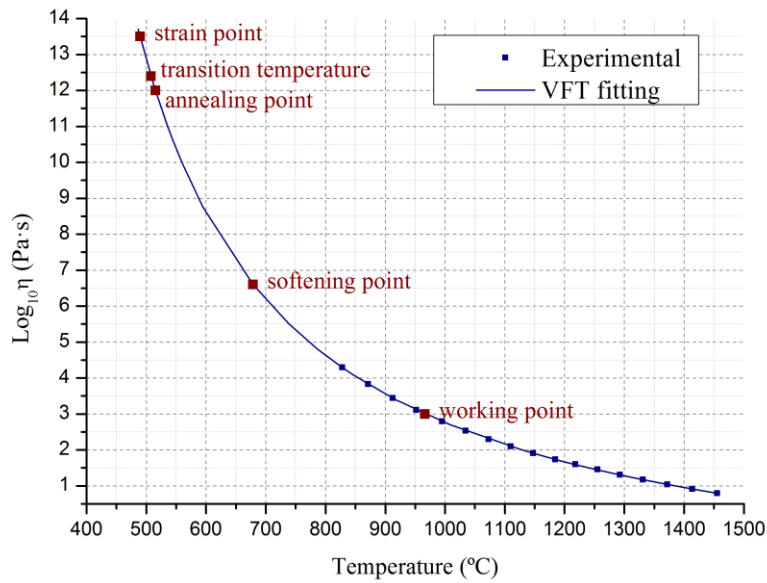


Fig. 3.3 - Glass viscosity with respect to temperature: experimental values and VFT fitting.

Based on viscosity data, an operating temperature of ~ 1000 °C was selected, slightly above the glass working point ($\eta \sim 10^3$ Pa·s). The slightly higher temperatures set for the crucible and nozzle accounted for heat losses due to frequent refilling and to the exposed nozzle tip respectively.

The annealing chamber was set slightly below the glass annealing temperature ($T_a \sim 515$ °C) to account for its thermal inertia.

The CFD model (Fig. 3.4(a)) reported temperatures of ~ 948 °C for the nozzle's outer surface and ~ 965 °C for the glass at the nozzle exit. The differences from the first model iteration lied both in the more accurate model and in the adoption of a different nozzle geometry.

The glass temperature value measured from the infrared images (Fig. 3.4(b)) was slightly lower than that estimated by the model, in the range of 890 – 920 °C.

Such difference was probably due to some simplifying assumptions made during the simulation, i.e. the crucible and nozzle kilns as uniform heating sources in direct contact with the crucible and nozzle assembly. It is also worth noting that a precise temperature measurement at the nozzle exit was not possible due to the setup and to the printer configuration, and that the temperature decrease in the extruded glass was extremely relevant. Moreover, the glass temperature at the nozzle exit was close to the IR camera threshold value, making the measurement not highly accurate.

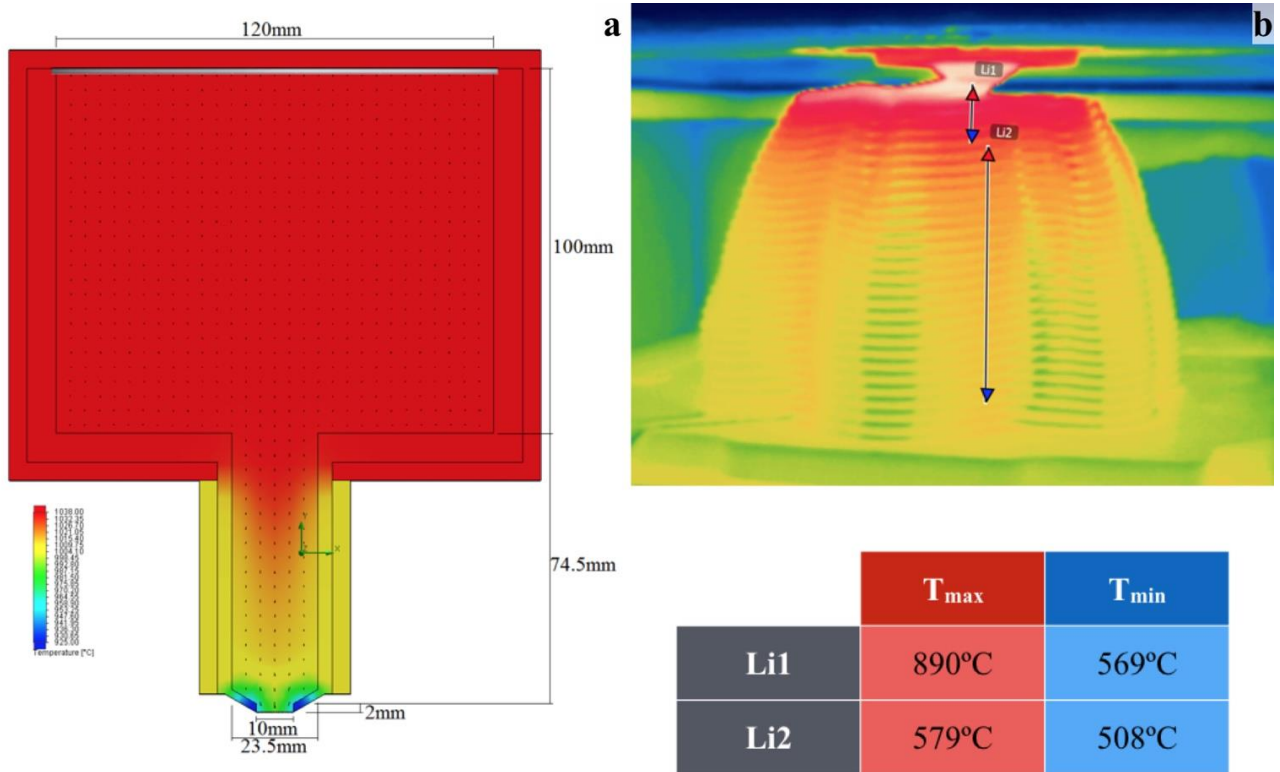


Fig. 3.4 - (a) CFD model of the crucible-nozzle assembly showing temperature simulation and (b) IR image of the printing process (credits: Witcher, F.).

What was clear from the image is that temperature decreased drastically in the printed object as new layers were deposited, creating a gradient of more than 300°C between the most recent 5 layers. This led to a viscosity increase of five orders of magnitude, which was crucial to the stability of the object during printing. Note that the whole object remained in the 500 – 570 °C temperature range, which corresponded to the annealing temperature of the glass; therefore, no cracks or significant deformations occurred during printing.

The flow rate of glass through the nozzle was a determining factor for process calibration, helping to avoid undesired accumulation or lack of material on the printed object. The glass flow was modeled as the laminar flow of a viscous fluid through a tube [17]; such assumption was largely justified by the fact that in the process conditions the Reynolds number, a dimensionless parameter used to predict flow patterns, was $\sim 2.1 \cdot 10^{-4}$, indicating a linear flow with predominance of viscous forces over inertial ones. The volume flow rate Q [m³/s] through a cylindrical tube is given by the Hagen-Poiseuille law [17]:

$$Q = \frac{\Delta P}{R} = \left(\frac{\pi r^4}{8\eta L} \right) \cdot (\rho g \Delta h) \quad (3.3)$$

Where ΔP [Pa] is the pressure drop at the bottom of the tube and $R = \frac{8}{\pi} \eta \frac{L}{r^4}$ [Pa/(m³/s)] is the resistance to flow. R is determined by two factors: geometry of the tube (primarily its radius) and glass viscosity.

The nozzle was designed through several iterations in order to be optimized with respect to two factors: glass flow and adhesion of glass to its tip (favored by low tapering angles). Based on the understanding that the final smallest diameter drives the overall flow resistance, the depth of the nozzle at its orifice (i.e. the length of the channel with the smallest dimension through which the glass flows) was minimized; the portion of the nozzle tip sticking out of the nozzle kiln was kept as small as possible to minimize thermal losses. The features of the final nozzle and assembly are reported in Fig. 3.4(a) and Table 3.4.

Table 3.4 - Geometry of the crucible and nozzle assembly and corresponding resistance to the glass flow.

	r (mm)	L (mm)	R (Pa·s/m³)	R (%)
Crucible	60	80	1.61 x 10 ⁷	0.1
Nozzle body	11.75	74.5	1.02 x 10 ¹⁰	54.9
Nozzle tip	5	2	8.34 x 10 ⁹	45.0
Total		156.5	1.85 x 10¹⁰	100.0

Glass exiting the nozzle at ~965 °C had a dynamic viscosity $\eta \sim 1020$ Pa·s. Since the process was gravity driven, the pressure drop was a function of the molten glass level inside the crucible. At the beginning of a new printing job, the crucible was filled up to a height $L \sim 80$ mm, resulting in a pressure drop $\Delta P \sim 3.6$ kPa.

The resistance to the flow was provided by the whole crucible and nozzle assembly (differently from what previously reported [1], where only the final part of the nozzle was considered); leading to an estimated volume flow rate of $Q \sim 200$ mm³/s. Dividing by the orifice area, a linear flow rate of $\tilde{v} \sim 2.5$ mm/s was calculated. As the glass level in the crucible decreased, Q decreased linearly; consistency during printing was achieved by frequently refilling the crucible to the initial height.

The printing process was tailored according to the temperature and resultant viscosity and flow rate. The layer height was set at 4.5 mm in order to provide a wide contact area between the layers; therefore, the resulting cross section of the deposited filament resembled an ellipse.

The nozzle enabled direct deposition of material according to its position along the z axis, rather than in reference to the height of the previous layer; therefore, any variation in flow rate affected the printed wall width rather than its height.

Different printing rates were tested while keeping the temperatures and the layer height constant. Driving the extruder at a slightly greater rate than the natural flow resulted in thinner layers and helped achieve a more homogeneous filament, since the pulling prevented the buildup of glass excess at the nozzle. Printing rates in the range of 5.8 – 6.3 mm/s were finally adopted. In order to achieve effective adhesion to the building platform, the first layer's printing rate was decreased by 25%, enabling the glass to settle on the platform.

The resulting layer width was predicted by modeling the filament cross section as an ellipse, with a smaller axis $2a = 4.5$ mm corresponding to the fixed layer height. The layer width is given by:

$$Q = \pi ab \cdot \text{feed rate} \quad (3.4)$$

Where πab is the cross section area, and a and b are the ellipse semi-axes. This resulted in an estimated layer width of $2b \sim 9$ mm.

Printing parameters are reported in Table 3.5.

Table 3.5 - Printing parameters.

Pressure (Pa)	Q (mm³/s)	f (mm/s)	Printing rate (mm/s)	Layer height (mm)	Estimated layer width (mm)
3623	195	2.5	6.1	4.5	9

Geometric primitives printed for evaluation purposes rapidly evolved into a range of shapes and cross sections embodying overhangs and other morphological features. Some exploratory designs are shown in Fig. 3.5, together with their design parameters reported in Table 3.6.

Table 3.6 - Design parameters of the 3D printed objects in Fig. 3.5.

	A	B	C	D	E	F
Feed rate (mm/s)	4.5	5.8	6.1	6.1	6.1	6.3
Minimum radius (mm)	16	30	22	28	21	8
Maximum draft angle (°)	20	0	28	29	28	32

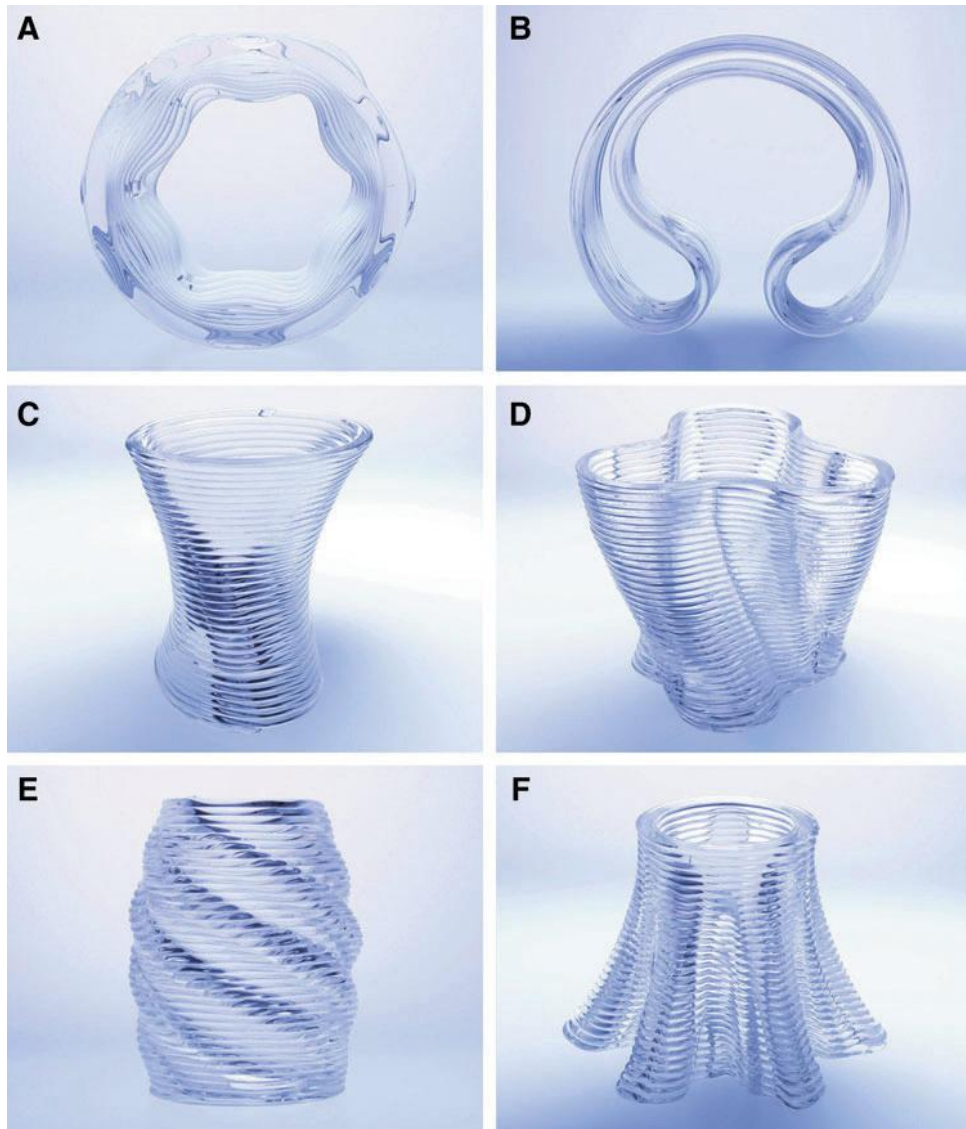


Fig. 3.5 - Some 3D printed objects exploring different design parameters: (A, B) focus on layer width; (C) smaller radii, higher drafting; (D) changes in concavity/convexity in plane; (E) changes in concavity/convexity out of plane; (F) smallest radii and highest draft angles. The layer height of 4.5 mm can be used as reference for dimensions (credits: Inamura, C.) [1].

A range of different shapes were printed with the aim of identifying the capabilities and limitations of the system and of quantitatively characterizing the most effective parameters to build successful parts. In the optimal printing conditions, parts with draft angles up to 40° and turning radii down to 14 mm were printed. Changes of convexity within the same layer were also found to be a constraint and resulted in deviation from the CAD model. Distortions were likely caused by accumulation of glass at the nozzle face and by some misaligned pull force due to surface tension between the glass on the nozzle face and the just deposited layer. Geometries - where the change in convexity occurs not within a single layer, but over the entire height of the part - were created to avoid such issues.

Characterization of the printed objects

The accuracy and precision of the printing process were estimated by comparing a 3D reconstruction of a printed cylinder with its source file (Fig. 3.6). The cylindrical prism design had a smooth surface with a wall width of 9 mm and a constant outer diameter of 85 mm.

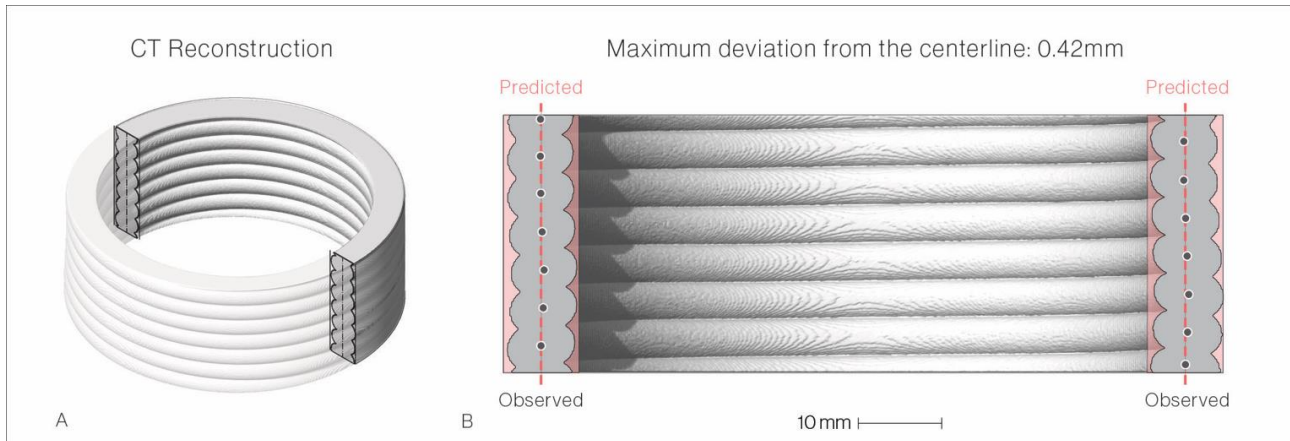


Fig. 3.6 - Micro CT reconstruction of a glass cylinder compared to its source file: (a) 3D reconstruction and (b) section [1].

The actual cylinder, as expected, was comprised of distinct layer as a result of the extrusion-based manufacturing process. The measured layer height was 4.5 mm as per G-code, and remained consistent through the analyzed section. The wall width was slightly but consistently overestimated in the CAD file: the average measured layer width was 7.95 ± 0.19 mm.

This variation was a function of both head pressure based on glass level and nozzle orifice manufacturing tolerances. The deposition of the glass layers, however, appeared highly precise: the deviation of the filament centers from the centerline was 0.18 ± 0.13 mm over the analyzed section (or ca. 2.25% of the total wall width).

The maximum deviation observed was 0.42 mm. Therefore; at this stage of development 0.5 mm could be considered a conservative value for the dimensional tolerance of printed glass objects.

SEM images of wall sections (Fig. 3.7) demonstrated a high homogeneity through the layers and suggested strong adhesion between them.

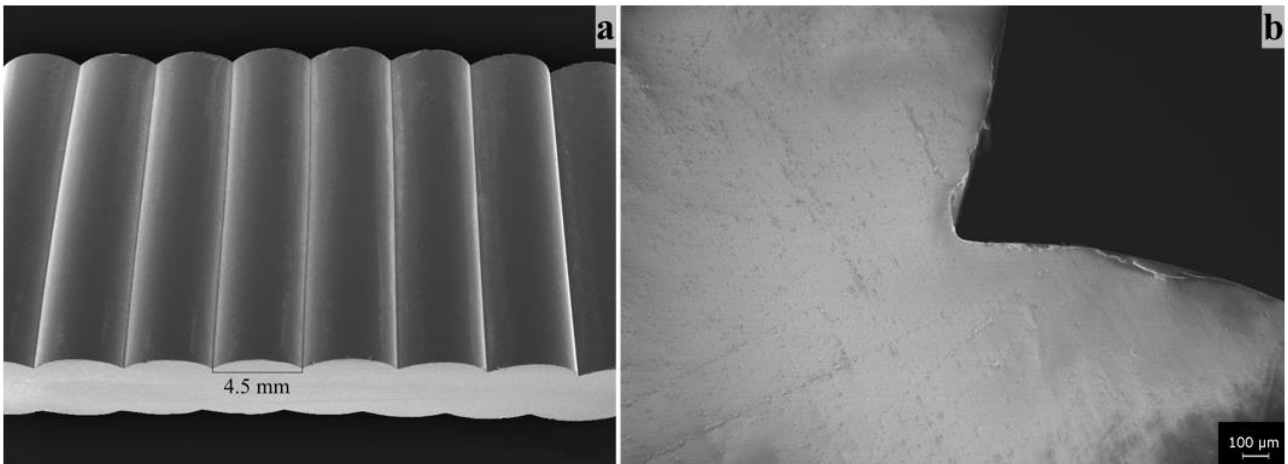


Fig. 3.7 - (a) SEM image of a cut and polished sample (credits: Weaver, J. C.); (b) SEM of the interface between two layers [1].

Preliminary mechanical testing was performed in order to evaluate the adhesion between the layers (generally critical in a 3D printing process). It was observed that, although the interface between layers acted as a stress concentrator, the crack did not occur at the interface but penetrated the layer (see Fig. 3.8), a sign that the printed glass part could be considered as a monolith. Homogeneous stress distribution with negligible stress concentration along the layers was confirmed also by means of polariscopy.

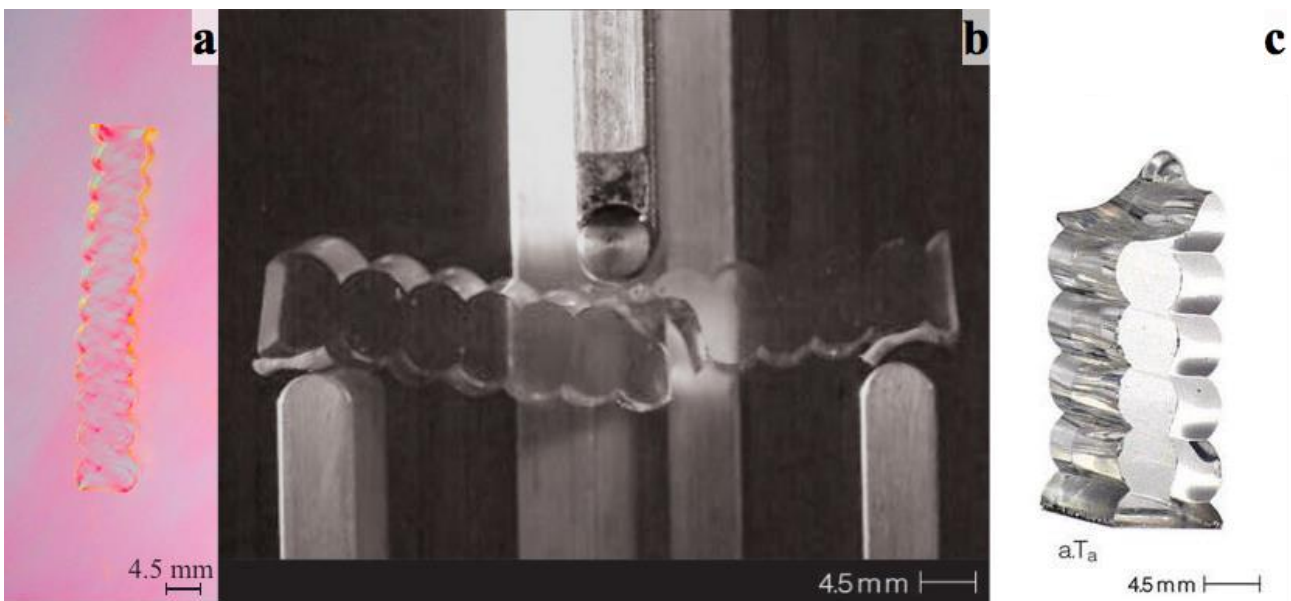


Fig. 3.8 – (a) cut and polished sample under polarized light; (b) 3 points bending test (credits: Hounsell, K.); (c) the sample after fracture [1].

Another evidence of the high quality of the interface was provided by the very little image distortion occurring in z direction, as visible in Fig. 3.9(a).

Light refraction and scattering caused by the layered surface texture, on the other end, offered new perspectives on light control and additional optical properties (see Fig. 3.9(b)), that could be exploited for examples for the creation of objects, such as lamp shades, displaying particular visual effects.

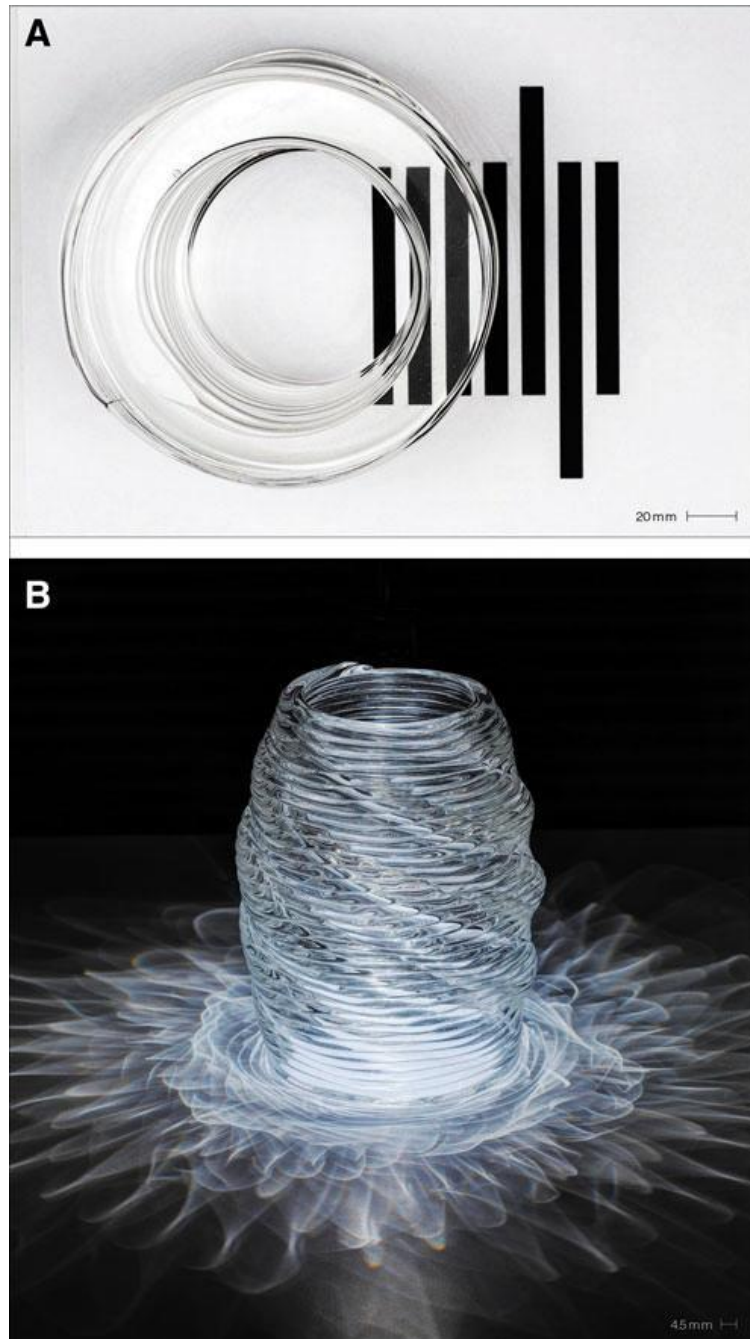


Fig. 3.9 - Optical properties and caustic patterns of printed parts. (A) Top view of a 70mm tall cylinder showing a high level of transparency; (B) caustic patterns created by illumination from a suspended overhead LED (credits: Ryan, A.)

[1].

Case studies

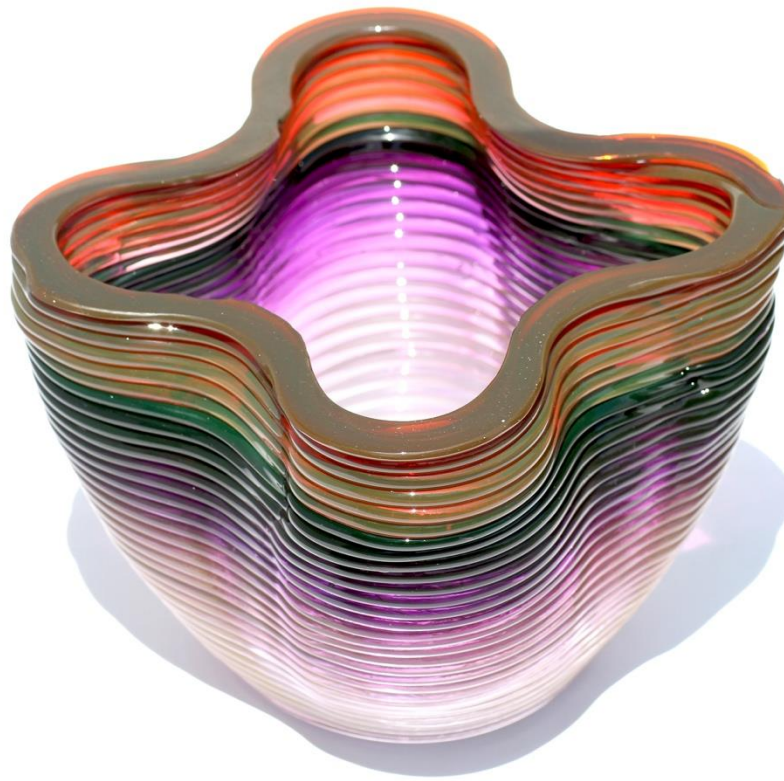


Fig. 3.10 - Example of a color printed object; layer height of 4.5 mm can be used as reference for dimensions (credits: Imanura, C.).

A preliminary test with colored glass frits demonstrated that it is possible to print objects containing multiple colors (Fig. 3.10). The frits were individually added to the crucible partially filled with molten glass; due to their relatively low melting point and mass, they melted within minutes and became homogeneous within the glass bath. It appears that the printing process was not noticeably affected by the addition of the colored frits; additional evaluation is, of course, necessary to determine the feasibility and repeatability of these effects, currently under way at the Mediated Matter group.

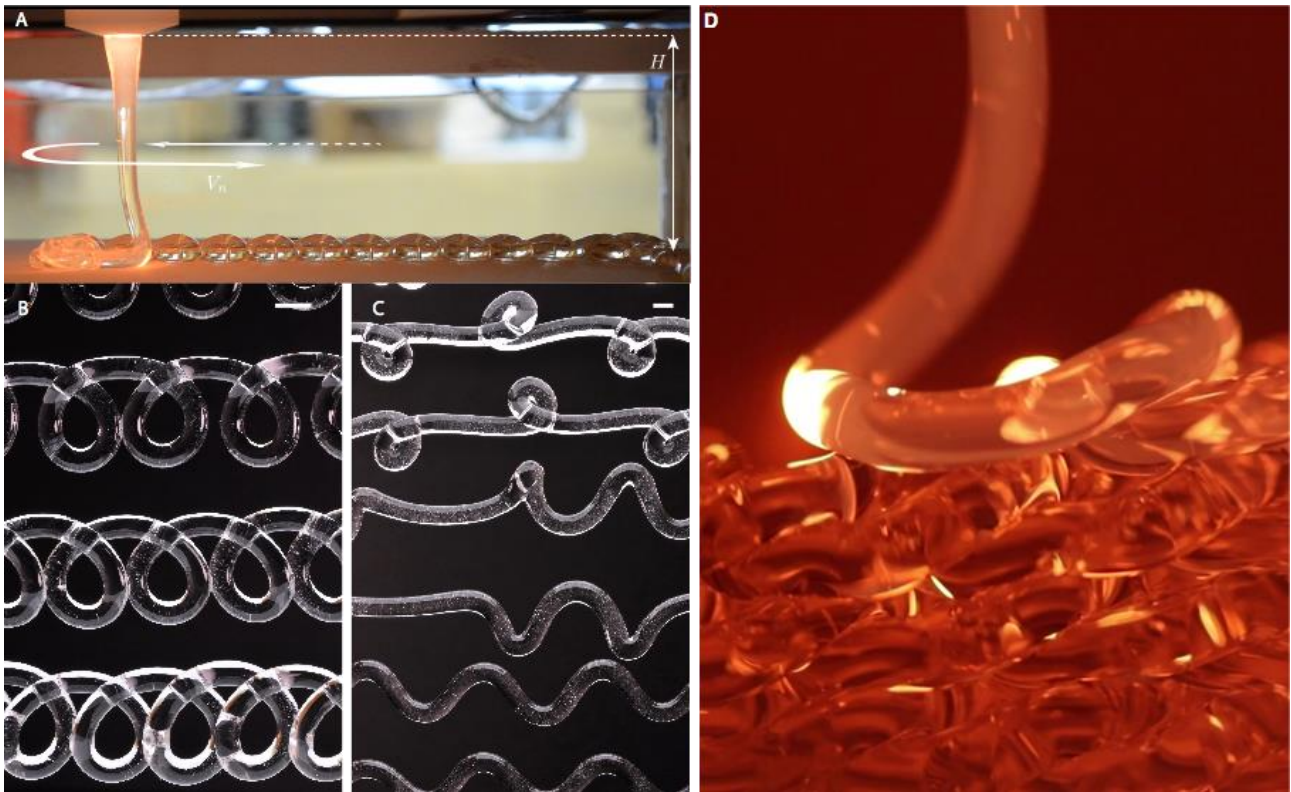


Fig. 3.11 – (a) Deposition of molten glass from an offset. (b) low advection speed: translated coiling patterns; (c) higher advection speed: from alternating loops (top) to W patterns (bottom). (d) multiple layer deposition (credits: Brun, P.-T.) [18].

Deposition of molten glass from an offset was also explored with different relative speeds of nozzle and substrate. The formation of different patterns including meanders, W patterns, alternating loops and translated coiling was observed by varying the advection speed of nozzle relative to the impinging speed of the falling glass (Fig. 3.11) [19]. Those features, arising from a fluidic instability, have been described and predicted by P.-T. Brun (MIT Math Department) through a minimal geometrical model [18]. They may be used as building blocks for the fabrication of larger objects combining the digital precision of the printer at a given scale and the formation of patterns at smaller scale.

Similarly, the creation of delicate suspended features with large overhangs was observed (Fig. 3.12), attributed to a variation of the glass flow rate due to the decreasing glass level in the crucible. Accurate control of feed rate and acceleration may allow to emulate this phenomenon in a controlled manner, thereby achieving designed interstitial spaces between printed layers. This capability may provide for the production of lighter architectural components that transition between structural typologies and also for additional functionalities such as transport and filtering of fluid media.

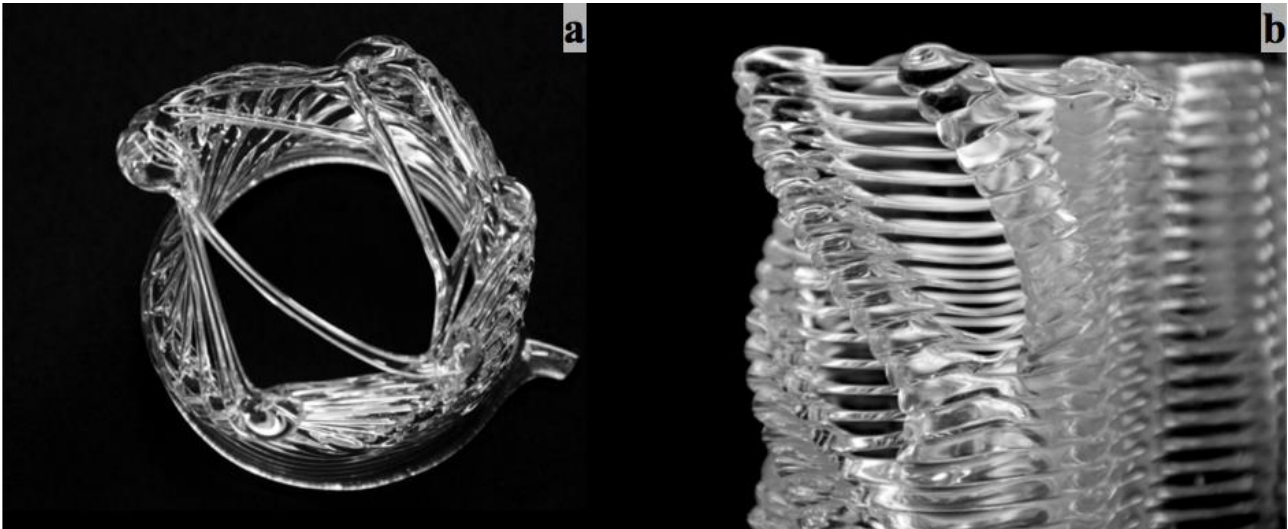


Fig. 3.12 - (a) top view and (b) side view of a glass component showing suspended struts with large overhangs (credits: Lizardo, D.).

Conclusions and Future Work

This work comprised the development of a novel extrusion-based AM approach for the production of objects starting from molten glass. The system processed glass from the molten state to annealed components of complex, digitally designed forms. Process optimization involved glass viscosity measurements and modeling as well as control over parameters such as pressure head, temperatures in the different equipment zones, and printing rate. The printer's capabilities were characterized in fabricating objects possessing draft angles and tight radii. Proofs of concepts were presented for the integration of colors, the control on viscous flow instability and the creation of suspended struts. Mastering these phenomena would lead to tailored optical properties as well as to new functionalities.

Preliminary characterization of the produced parts showed that it was possible to print with high precision and accuracy, and that a strong adhesion between layers existed and resulted in high transparency and low image distortion through the layers, for the first time in the history of glass AM.

Future developments of this process would include the fabrication of a higher performance system with the capability of printing increasingly complex objects, with finer resolution and additional functionalities. Improvements could comprise a more accurate temperature control and faster heating-cooling ramps, optimization of the nozzle tip, the addition of a piston and of an automated feeding system [20]. Higher structural and environmental performance for the printed parts could be achieved through geometric complexity and topological optimization; the fabrication of bespoke glass objects would provide the opportunity for developing complex scaffolds, fluidics and custom made products for specific applications.

References

- [1] J. Klein, M. Stern, G. Franchin, M. Kayser, C. Inamura, S. Dave, J.C.J.C. Weaver, P. Houk, P. Colombo, M. Yang, N. Oxman, G. Franchin, M. Kayser, C. Inamura, S. Dave, J.C.J.C. Weaver, P. Houk, P. Colombo, M. Yang, N. Oxman, Additive Manufacturing of Optically Transparent Glass, 3D Print. Addit. Manuf. 2 (2015) 92–105. doi:10.1089/3dp.2015.0021.
- [2] Bullseye Glass Co., The Vitrigraph Kiln - creating a new vocabulary in fused glass, (2014) 1–4.
- [3] E. Roeder, Extrusion of glass, J. Non. Cryst. Solids. 5 (1971) 377–388. doi:10.1016/0022-3093(71)90039-1.
- [4] G. Marchelli, R. Prabhakar, D. Storti, M. Ganter, The guide to glass 3D printing: developments, methods, diagnostics and results, Rapid Prototyp. J. 17 (2011) 187–194. doi:10.1108/13552541111124761.
- [5] S. Klein, S. Simske, C. Parraman, P. Walters, D. Huson, S. Hoskins, 3D Printing of Transparent Glass, HP Tech Rep. (2012).
- [6] L. The Ex One Company, The New Standard for Manufacturing from ExOne e Manufacturing in Sand, (n.d.).
- [7] R. Clasen, Method for the manufacture of glass bodies by extrusion, US 4682995 A, 1987.
- [8] R. Clasen, B. Schmidl, Method of manufacturing glass bodies by means of extrusion, US 4816051 A, 1989.
- [9] S. Eqtesadi, A. Motealleh, P. Miranda, A. Pajares, A. Lemos, J.M.F. Ferreira, Robocasting of 45S5 bioactive glass scaffolds for bone tissue engineering, J. Eur. Ceram. Soc. 34 (2014) 107–118. doi:10.1016/j.jeurceramsoc.2013.08.003.
- [10] J. Luo, L. Gilbert, C. Qu, J. Wilson, D. Bristow, R. Landers, Wire-Fed Additive Manufacturing of Transparent Glass Parts, in: Proc. ASME 2015 Int. Manuf. Sci. Eng. Conf. MSEC2015, Charlotte, North Carolina, USA, 2015: pp. 1–5.
- [11] J. Luo, H. Pan, E.C. Kinzel, Additive Manufacturing of Glass, J. Manuf. Sci. Eng. 136 (2014) 61024. doi:10.1115/1.4028531.
- [12] J.-P.H.R. Lereboullet, M. Prassas, Additive Manufacturing processes for making transparent 3D parts from inorganic materials, WO 2016/137956 A1, 2016.
- [13] H. Vogel, Das Temperaturabhängigkeitsgesetz der Viskosität von Flüssigkeiten, Phys. Z. 22 (1921) 645–646.
- [14] G.S. Fulcher, Analysis of recent measurements of the viscosity of glasses, J. Am. Ceram. Soc. 8 (1925) 339–355.
- [15] G. Tammann, W. Hesse, Die Abhängigkeit der Viskosität von der Temperatur bei

unterkühlten Flüssigkeiten, *Z. Anorg. Allg. Chem.* 156 (1926) 245–257.

- [16] J. Schindelin, I. Arganda-Carreras, E. Frise, V. Kaynig, M. Longair, T. Pietzsch, S. Preibisch, C. Rueden, S. Saalfeld, B. Schmid, J.-Y. Tinevez, D.J. White, V. Hartenstein, K. Eliceiri, P. Tomancak, A. Cardona, Fiji: an open-source platform for biological-image analysis, *Nat. Methods.* 9 (2012) 676–682. doi:10.1038/nmeth.2019.
- [17] R.B. Bird, W.E. Stewart, E.N. Lightfoot, *Transport Phenomena*, Wiley, 1958.
- [18] P.-T. Brun, C. Inamura, D. Lizardo, G. Franchin, M. Stern, P. Houk, N. Oxman, The molten glass sewing machine, *Proc. R. Soc. A.* (submitted).
- [19] P.-T. Brun, B. Audoly, N.M. Ribe, T.S. Eaves, J.R. Lister, Liquid Ropes : A Geometrical Model for Thin Viscous Jet Instabilities, *Phys. Rev. Lett.* 174501 (2015) 1–5. doi:10.1103/PhysRevLett.114.174501.
- [20] C. Inamura, *Towards a New Transparency: High Fidelity Additive Manufacturing of Transparent Glass Structures across Scales*, Massachusetts Institute of Technology, 2017.

Summary and conclusions

The previous chapters demonstrated the feasibility of AM routes for ceramic materials embracing polymer related technologies to provide an alternative to the ceramic powder-binder approaches.

Chapter 1 focused on the use of a preceramic polymer as a non sacrificial, reactive binder to develop inks for stereolithography (SL) and direct ink writing (DIW).

First, SL of a pure preceramic polymer was demonstrated; a commercially available ceramic precursor was chemically modified in order to introduce photo-polymerizable ends. Cellular geometries with strut size down to ~ 200 μm were fabricated and converted to dense, crack-free SiOC micro-components with optimal surface quality through pyrolysis at 1000 °C. No shape limitations (i.e. overhangs, undercuts, cavities) were experienced, but porous structures or small dense parts are the best options in order to avoid residual pores and cracks caused by the polymer decomposition during pyrolysis. The micro-components possessed a compressive strength in accordance with that of conventionally produced components.

The same preceramic polymer was used as a basis for DIW inks. In the first of these investigations, the polymer was additivated with active and inert fillers to produce complex biosilicate scaffolds for tissue engineering. The preceramic polymer, together with the addition of fumed silica, had the double role of source of silica and rheology modifier. The preceramic polymer acted as a polymeric binder and increased the viscosity of the ink, while the fumed silica additive induced a “gel-like” behavior by forming a network of silica colloidal agglomerates. Scaffolds with a rod diameter of 350 μm and a spanning distance of 1 mm were effectively produced and converted to the desired hardystonite phase upon pyrolysis in air, while a heat treatment in nitrogen produced (also bioactive) wollastonite polymorphs. The produced scaffolds had mechanical properties adequate for non load-bearing bioengineering applications.

A second preceramic polymer-based ink for DIW was developed for the production of ceramic matrix composites (CMCs); the preceramic polymer developed the ceramic matrix (SiOC) upon pyrolysis in inert atmosphere, whereas reinforcement was given by chopped carbon fibers. Formulations with a volume fraction of fibers above 30 vol% were suitable for the extrusion of fine filaments (< 1 mm diameter). The shear stresses generated at the nozzle tip seemed to orient the fibers in the extrusion direction; the process could possibly fabricate single material objects with gradually changing mechanical and functional properties.

The addition of SiC powder as passive filler allowed to produce components with a limited amount of cracks. A proper rheological characterization and optimization is still needed, but complex structures with porosity of $\sim 75\%$ and compressive strength of ~ 4 MPa were printed.

Chapter 2 presented the developments of the AM of geopolymers, aluminosilicate slurries which set at room (or relatively low) temperature through a polymer-like polycondensation reaction.

Geopolymer components with controlled porosity were designed and produced by negative replica of PLA sacrificial templates fabricated by FDM. A geopolymer slurry was used to produce accurate inverse replicas by impregnation in vacuum conditions and subsequent geopolymerization; the template was successfully removed by a combined chemical and thermal treatment. Samples possessed highly interconnected macroscopic channels and micro- and meso-porosity in the struts.

Several geopolymer inks were then developed for DIW; different water content and different kind and amount of additives were compared in order to optimize the rheological properties of the inks. The ink possessed a Bingham shear thinning behavior which enabled the extrusion as well as the retention of the produced shape even in the case of unsupported struts. Highly porous ceramic components (porosity up to ~71 vol%) with features of ~0.8 mm and unsupported parts with very limited sagging (less than 7% of the struts diameter) were produced and characterized; their mechanical properties were investigated and correlated with their porosity.

Chapter 3 reported the development of a novel extrusion-based AM approach for the production of objects starting from molten glass. The system processed glass from the molten state to annealed components of complex, digitally designed forms. Process optimization involved glass viscosity measurements and modeling as well as control over parameters such as pressure head, temperatures in the different equipment zones, and printing rate. Objects possessing draft angles and tight radii were fabricated. Within the design space it was possible to print with high precision and accuracy; parts showed a strong adhesion between layers, and high transparency through the layers.

Proofs of concepts were presented for the integration of colors, the control on viscous flow instability and the creation of suspended struts. Mastering these phenomena could lead to geometric complexity and tailored functional properties.

Table II.I reports an overview of the materials and processes employed in this work with focus on their features, advantages and limitations. The chart can be read in two directions: horizontally, from a technology perspective, and vertically, for a focus on materials.

Table II.I – Overview chart of the material and processes employed in this work.

	PRECERAMIC POLYMERS <ul style="list-style-type: none"> - High ceramic yield (binder is also ceramic former) - Sintering required 	GEOPOLYMERS <ul style="list-style-type: none"> - Inorganic, reactive slurry: no binder removal nor sintering required - Limited working time 	GLASS
NEGATIVE REPLICA <ul style="list-style-type: none"> - Printing process parameters depending on what employed for the template fabrication (here: FDM) and not on the replica process - Limitations in strut size (here: ~1 mm) and porosity in order to provide adequate infiltration 		<ul style="list-style-type: none"> - Shrinkage: negligible - Porosity: 65-70% - Porous struts (+ material intrinsic porosity) - Chemo-thermal treatment required for template removal 	
SL <ul style="list-style-type: none"> - Layer resolution: $z = 25 \mu\text{m}$ - Printing volume: $76 \times 43 \times 150 \text{ mm}^3$ - Technology cost and availability: $>200\,000 \text{ €}$, commercially available - Process rate: up to 100 slices/hour (for commercial resins) 	<ul style="list-style-type: none"> - Chemical approach: photo-curable end groups attached to the silicone resin with low mass loss - Smallest feature dimension: $\sim 200 \mu\text{m}$ - Shrinkage: $\sim 25\%$ - Porosity: $>90\%$ - Dense struts - Complex feedstock adaptation and limited material library - Limited versatility 		
DIW <ul style="list-style-type: none"> - Layer resolution: $z = 50 \mu\text{m}$ - Printing volume: 200 mm (diameter) x 400 mm (height) - Technology cost and availability: $<5\,000 \text{ €}$, commercially available but under refinement - Process rate: 5-50 mm/s - Rheology optimization is mandatory 	<ul style="list-style-type: none"> - Smallest feature dimension: $\sim 400 \mu\text{m}$ - Shrinkage: $\sim 10\%$ - Porosity: $>75\%$ - Porous struts - low shrinkage and mass loss - Material versatility (filler addition leading to complex phase development) - Fiber alignment in CMCs 	<ul style="list-style-type: none"> - Smallest feature dimension: $\sim 800 \mu\text{m}$ - Shrinkage: $\sim 10\%$ - Porosity: $\sim 70\%$ - Porous struts (+ material intrinsic porosity) - Process could be scaled up 	
G3DP (FDM) <ul style="list-style-type: none"> - Layer resolution: $z \sim 5 \text{ mm}$ - Printing volume: $250 \times 250 \times 300 \text{ mm}^3$ - Technology cost and availability: not for sale, research project - Process rate: $\sim 10 \text{ mm/s}$ 			<ul style="list-style-type: none"> - Dense struts - Commercially available feedstock - Fusion-based process: no binder or sintering required - Annealing process performed by the printer - Transparency - Process could be scaled up

The choice of the technology depends on the material properties and on the geometrical features. Negative replica is likely the most versatile approach, as it does not need to adapt and optimize the desired ceramic material for an additive manufacturing process; a variety of stable, homogeneously dispersed ceramic slurries already exists for conventional casting processing and such know-how can effectively be transferred to the infiltration of printed sacrificial templates. Layer-by-layer inhomogeneous build up is also not an issue. On the other end, the negative replica approach is limited in the maximum porosity and in the minimum thickness of the struts: a high polymer content could in fact damage the structure upon removal, and small pores could not guarantee an effective impregnation.

SL was efficiently applied to preceramic polymers and is generally suitable for reproducing complex truss structures with a fine level of details; by not employing a sacrificial binder, the structural integrity of the printed parts is easier to preserve during pyrolysis. The overall shrinkage is generally lower compared to that of ceramic powder suspensions, thanks to the high ceramic yield of the resin; finally, it is possible to produce dense struts.

On the other hand, a chemical modification of the precursor involved is time consuming and not always possible, and the selection of an appropriate solvent is also not trivial. To date, material candidates should possess organic groups to which photocurable ends can be chemically attached. Further work could investigate the use of photocurable and not photocurable preceramic polymer blends to enlarge the material window. Another limitation in the material choice is given by the strict optical requirements (i.e. sufficient light transmittance): high absorbing fillers such as SiC powder cannot be embedded in the matrix.

From this perspective, DIW and extrusion-based approaches in general are more versatile and can be applied to a wide range of materials; the experiments conducted took pace from the existing literature and developed a comprehensive library of rheological tests and procedures to design a slurry with optimized properties. Such approaches were applied to various material families showing high potential to generate fine lattices with both porous and dense struts. Limiting aspects of DIW are: the lack of support for overhangs and suspended struts, and an inadequate pressure control that does not allow to pause and restart the material flow from a different location. On the other hand, there are less constraints on the addition of fillers and reinforcement, making such technology the most promising for the fabrication of ceramic matrix composites. The capability of orient directional fillers in the printing direction is of great interest for the production of anisotropic structures with higher toughness and resistance in specific directions/sections; such approach could be also use to orient grain growth upon sintering. If a concentration gradient of fillers could be achieved in the slurry, components with graded properties could also be produced.

FDM was employed in this work in a rather unconventional way, both for the material feedstock (glass nuggets molten into a crucible) and for the high temperatures employed; for these reasons, it is more precise to refer to it as a different technology, here named G3DP. The limitations of this approach in the ceramic world are the same of conventional processes: it is practically impossible and energy consuming to get to temperatures high enough to process ceramic materials in the molten state. Therefore, the technology is limited to glass materials, which require lower temperatures and whose continuous transition from a liquid to a metastable glass state can be exploited for process design and optimization. To date, this is the only technology which possibly allows to additively manufacture glass objects which resemble the visual and mechanical performance of glass constructs that are conventionally obtained.

For what concerns the material space, different material families were explored with the common aim of moving away from the use of a sacrificial binder.

Preceramic polymers form a big family of materials able to convert into multiple silicate phases; due to their polymeric nature, they can be shaped using various AM technologies. In this work, SL and DIW were explored, but no limitations with respect to negative replica and FDM are foreseen. Other examples of PDCs from AM were also reported (see Chapter 1). Their high thermomechanical properties, microstructural stability and unique functionalities (i.e. electronic conduction for SiCN- or C clusters) make them great alternative for traditional and technical ceramics. However, issues remain in the fabrication of dense, bulk components: above certain thickness, the pyrolysis process often generates cracks due to shrinkage and to the polymer decomposition. In this work, such phenomenon was always eliminated by the addition of fillers, which is not always desired or possible. The printed ceramic lattices could be suitable for many applications: biological investigation could validate hardystonite scaffolds for bone growth promotion; lattices with high specific surface area (SSA) could also be effectively employed as catalyst carriers. The use of functional fillers could produce complex geometries with added functionalities, such as electric conduction.

Geopolymers highest potential lies in their room temperature consolidation: they do not need any heating treatment, neither on the feedstocks nor on the printed components. The low energy consumption and CO₂ emissions associated with their production make a green, sustainable alternative to traditional materials such as cement. Such features have opened the way to large scale AM for the building industry. They can be easily reinforced with various particles and fibers in order to improve their mechanical properties.

Exploration of their filtration properties is suggested by their intrinsic porosity, which can be enhanced by fabricating highly porous structures as well as by foaming; it could be validated by permeability and adsorption tests. Their potential applications therefore spread from the micro- to the macroscale.

Glass is the most commonly available material on this list, and yet the one which faces the biggest challenges when it comes to AM. To date, sintering from glass powder, either by heat treatment or by SLS, was not able to produce strong, transparent components. The need of relatively high temperatures raises its production cost and limits its applicability. The fabrication of bespoke glass objects would provide the opportunity for developing custom made products for specific applications such as lab ware; on a bigger scale, printed components could be employed for the construction of structural architectural facades. By achieving higher resolution, complex systems for (micro)fluidics could be produced. Highly porous bioglass scaffolds with higher mechanical properties could find application as biomedical devices for tissue regeneration.

Despite of being still at a research stage, the explored approaches and materials showed potential for the production of complex glass and ceramic components and cellular architectures with applications ranging across scales.

Publications

Papers

- Franchin, G.; Colombo, P.: Porous Geopolymer Components through Inverse Replica of 3D Printed Sacrificial Templates, *Journal of Ceramic Science and Technology* 2/2015 Vol. 6 No.2, 105-112 [DOI: 10.4416/JCST2014-00057];
- Elsayed, H.; Zocca, A.; Franchin, G.; Bernardo, E.; Colombo, P.: Hardystonite Bioceramics from Pre-ceramic Polymers, *Journal of the European Ceramic Society* 36/2016, 829-835 [DOI: 10.1016/j.jeurceramsoc.2015.10.034];
- Zanchetta, E.; Cattaldo, M.; Franchin, G.; Schwentenwein, M.; Homa, J.; Brusatin, G.; Colombo, P.: Stereo-photo-lithographic 3D printing of SiOC ceramic micro-components, *Advanced Materials* 28/2016, 370-376 [DOI: 10.1002/adma.201503470];
- Franchin, G.; Klein, J.; Stern, M.; Kayser, M.; Inamura, C.; Dave, S.; Weaver, J. C.; Houk, P.; Colombo, P.; Yang, M.; Oxman, N.: Additive Manufacturing of Optically Transparent Glass, *3D Printing and Additive Manufacturing* 2/2015, 92-105 [DOI: 10.1089/3dp.2015.0021];
- Zocca, A.; Franchin, G.; Elsayed, H.; Gioffredi, E.; Bernardo, E.; Colombo, P.: Direct ink writing of a pre-ceramic polymer and fillers to produce hardystonite ($\text{Ca}_2\text{ZnSi}_2\text{O}_7$) bioceramic scaffolds, *Journal of the American Ceramic Society* 2016, 1-8 [DOI: 10.1111/jace.14213].
- Franchin, G.; Scanferla, P.; Zeffiro, L.; Elsayed, H.; Baliello, A.; Giacomello, G.; Pasetto, M.; Colombo, P.: Direct Ink Writing with Geopolymeric Inks, *Journal of the European Ceramic Society* (accepted)

Patents

- Klein, J.; Franchin, G.; Stern, M.; Kayser, M.; Inamura, C.; Dave, S.; Oxman, N.; Houk, P.: Methods and Apparatus for Additive Manufacturing of Glass, U.S. Patent Application 14697564, filed 2015/04/27;
- Colombo, P.; Franchin, G.; Elsayed, H.; Sin, A.: Geopolymeric Formulations and Associated Methods for the Manufacturing of Three-Dimensional Structures, in particular in Manufacturing Brake Pads, IT Patent Application 102015000085390, filed 2015/12/18.

Oral Presentations

- Franchin, G.; Zocca, A.; Elsayed, H.; Chiappone, A.; Gioffredi, E.; Bernardo, E.; Colombo, P.: Extrusion-based three-dimensional printing of hardystonite from a preceramic polymer and fillers. Materials Science & Technology 2015, 2015/10/5-8 Columbus, OH, USA – Graduate Excellence in Materials Science: Diamond Award;
- Franchin, G.; Zocca, A.; Elsayed, H.; Chiappone, A.; Gioffredi, E.; Bernardo, E.; Colombo, P.: Direct ink-writing of a preceramic polymer and fillers to produce hardystonite ($\text{Ca}_2\text{ZnSi}_2\text{O}_7$) bioceramic scaffolds. 40th International Conference and Expo on Advanced Ceramics and Composites, 2016/01/24-29 Daytona Beach, FL, USA;
- Franchin, G.; Klein, J.; Stern, M.; Kayser, M.; Inamura, C.; Dave, S.; Weaver, J. C.; Houk, P.; Colombo, P.; Yang, M.; Oxman, N.: Additive Manufacturing of Optically Transparent Glass. 40th International Conference and Expo on Advanced Ceramics and Composites, 2016/01/24-29 Daytona Beach, FL, USA.
- Colombo P.; Franchin G.; Elsayed H.; Schmidt J.; Scanferla P.: Stampa additiva di ceramici usando polimeri inorganici. Technology Hub, Milan, IT, June 7-9, 2016.
- Houk P.; Franchin G.; Additive Manufacturing of Optically Transparent Glass. Additive Manufacturing Talks, Milan, IT, June 10, 2016.
- Franchin G.; Elsayed H.; Scanferla P.; De Marzi A.; Gobbin F.; Conte A.; Italiano A.; Colombo P.: Direct and indirect 3D printing with geopolymers. Geopolymer Camp 2016, Saint-Quentin, FR, July 4-6, 2016.
- Franchin G.; Klein J.; Stern M.; Kayser M.; Inamura C.; Dave S.; Weaver J.; Houk P.; Colombo P.; Yang M.; Oxman N.: Additive Manufacturing of Optically Transparent Glass. 6st International Congress on Ceramics, Dresden, DE, August 21-25, 2016.
- Franchin G.; Colombo P.: Additive Manufacturing of Ceramics using Inorganic Polymers. 6st International Congress on Ceramics, Dresden, DE, August 21-25 2016.
- Franchin, G.; Scanferla, P.; Zeffiro, L.; Elsayed, H.; Baliello, A.; Pasetto, M.; Colombo, P.: Direct Ink Writing of Geopolymers. 41th International Conference and Expo on Advanced Ceramics and Composites, 2017/01/22-27 Daytona Beach, FL, USA.
- Franchin, G.; Wahl, L.; Colombo, P.: Direct Ink Writing of Ceramic Matrix Composites from a Preceramic Polymer and Fillers. 41th International Conference and Expo on Advanced Ceramics and Composites, 2017/01/22-27 Daytona Beach, FL, USA.

Posters

- Colombo, P.; Franchin, G.; Strozi Cilla, M.: Novel Routes for Open Cell Geopolymer Components, Workshop How To Exploit Porosity in Geopolymers. 2014/10/02 Faenza, IT – Best Poster Award;
- Franchin, G.; Zocca, A.; Colombo, P.: 3D Printed Biosilicate Scaffolds from Preceramic Polymers, Massachusetts Institute of Technology Polymer Day. 2015/03/11 Cambridge, MA, USA;
- Colombo, P.; Franchin, G.; Elsayed, H.; Scanferla, P.; De Marzi, A.; Italiano, A.: Direct and indirect 3D printing of components with geopolymers. 40th International Conference and Expo on Advanced Ceramics and Composites, 2016/01/24-29 Daytona Beach, FL, USA.

Videos

- GLASS – Glass 3D Printing [<https://vimeo.com/136764796>]
- The Molten Glass Sewing Machine [<https://www.youtube.com/watch?v=d1SB3F3EFrY>]

Curriculum vitae

Personal data

Name: Giorgia Franchin

Date of birth: 27 June 1989

Place of birth: Padova (PD), Italy

Gender: Female

Nationality: Italian

Education and research

- 10/2008 - 09/2011 BSc in Materials and Chemical Engineering, University of Padova (Italy).
- 10/2011 - 10/2013 MSc in Materials Engineering, University of Padova (Italy).
 - 03-08/2012: European Program LPP-Erasmus, Friedrich-Alexander Universität Erlangen-Nürnberg, DE.
- 01/2014 - present: PhD in Industrial Engineering, University of Padova (Italy).
 - 01-08/2015: Glass printing project, Mediated Matter Group, Media Lab, Massachusetts Institute of Technology, Cambridge, MA USA. Supervisor: Prof. Neri Oxman.

Students thesis co-advised

- Marco Cattaldo, BSc: Pre-ceramic polymer functionalization for stereolithography of SiOC microcomponents. 2014/2015
- Luca Zeffiro, BSc: 3D printing and characterization of geopolymer components. 2015/2016
- Filippo Gobbin, MSc: Inorganic binders for indirect 3D printing of ceramic powders. 2015/2016